Variation spatiale des conditions de circulation des fluides à l'origine de la minéralisation en or orogénique dans le segment Augmitto-Bouzan (Sous-Province de l'Abitibi, Québec, Canada)

Mémoire

Guillaume Raymond

Maîtrise interuniversitaire en sciences de la Terre - avec mémoire
Maître ès sciences (M. Sc.)

Québec, Canada

Variation spatiale des conditions de circulation des fluides à l'origine de la minéralisation en or orogénique dans le segment Augmitto-Bouzan (Sous-Province de l'Abitibi, Québec, Canada)

Mémoire

Guillaume Raymond

Sous la direction de :

Georges Beaudoin, directeur de recherche

Crystal LaFlamme, codirectrice de recherche

Résumé

Augmitto-Bouzan est un segment de 12 km de long à Rouyn-Noranda (Québec, Canada) de la zone de déformation Cadillac Larder-Lake (ZDCLL) caractérisé par une minéralisation aurifère inégalement distribuée, dans des veines de quartz-carbonate±tourmaline. L'étude compare les conditions de circulation passées des fluides entre les secteurs enrichis et pauvres en or afin d'identifier les processus responsables de l'enrichissement en or du segment.

Les veines de quartz ($\delta^{18}O$: 11.3-16.8‰) tourmaline ($\delta^{18}O$: 8.5-11.9‰; δD: –59- –18‰) et carbonate ($\delta^{18}O$: 11.3-15‰; $\delta^{13}C$: –6.2- –2.8‰) sont principalement encaissées dans les roches ultramafiques-mafiques altérées du Groupe de Piché, reconnus comme étant l'expression physique de la ZDCLL. Le quartz et la tourmaline présentent des températures d'équilibre (228-420°C) qui définissent un gradient thermique vertical élevé (~30°C/100m) au sein du Groupe de Piché. La covariation entre la température et les valeurs $\delta^{18}O_{H2O}$ et δD_{H2O} est interprétée comme représentant un mélange entre un fluide métamorphique profond de haute température (>420°C), haut $\delta^{18}O_{H2O}$ (>10.8‰) et bas δD (<–29‰) et un fluide interstitiel de la croûte supérieure de plus basse température (<230°C), bas $\delta^{18}O$ (<4‰) et haut δD (~0‰). Les valeurs plus élevées de δD_{H2O} sont probablement liées aux cycles d'évaporation-condensation associés au mécanisme faille-valve dans les veines. Des remontées locales de fluide métamorphique, mises en évidence par l'interpolation du $\delta^{18}O_{H2O}$, sont observées dans les blocs Augmitto-Cinderella et Astoria et ont probablement été canalisées dans des structures de perméabilité plus élevée. Les secteurs moins minéralisés présentent des $\delta^{18}O_{H2O}$ et des rapports fluide/roche plus faibles, reflétant probablement une plus grande proportion de fluide poral et des changements d'écoulement des fluides. La modélisation de l'écoulement des fluides montre que la plus grande proportion de fluide de la croûte supérieure dans les secteurs moins minéralisés est due à 1) un écoulement moins volumineux de fluide métamorphique dans le Groupe de Piché plus mince et 2) la présence de roches plus poreuses au nord de la ZDCLL, à partir desquelles une quantité plus importante de fluide poral s'infiltre dans la faille. Nous suggérons donc que la majorité des variations des teneurs aurifères est liée à la variation du flux de fluide métamorphique le long du segment. Un écoulement de fluide métamorphique moins abondant ou dilué diminue le potentiel aurifère le long de la ZDCLL.

Abstract

Augmitto-Bouzan is a 12 km long segment of the Cadillac Larder-Lake deformation zone (CLLDZ) in Rouyn-Noranda (Québec, Canada) characterized by an uneven gold mineralization distribution, hosted in quartz-carbonate±tourmaline veins. This study compares the past fluid flow conditions between the variable gold-endowed sectors to identify processes responsible for gold endowment in the area.

Quartz ($\delta^{18}O$: 11.8-16.8‰), tourmaline ($\delta^{18}O$: 8.5-11.9‰; δD: –59- –18‰) and carbonate ($\delta^{18}O$: 11.3-15‰; $\delta^{13}C$: –6.2- –2.8‰) veins are mainly hosted in the ultramafic-mafic Piché Group recognized as the physical expression of the CLLDZ. Quartz and tourmaline display equilibrium temperatures (228-420°C) that define a high vertical thermal gradient (~30°C/100m) within the host lithologies Covariation between temperature and computed $\delta^{18}O_{H2O}$ and δD_{H2O} is interpreted to result from mixing between a high temperature (>420°C), high $\delta^{18}O$ (>10.8‰), and low δD (<–29‰) deep-seated metamorphic fluid, and a low temperature (<230°C), low $\delta^{18}O$ (<4‰) and high δD (~0‰) upper crustal pore fluid. The higher δD_{H2O} (up to 43‰) values are likely associated with flash vaporization and condensation cycles related to fault-valve mechanisms in the veins. Local upwellings of deep-seated fluid, evidenced by interpolation of $\delta^{18}O_{H2O,}$ are observed in the Augmitto-Cinderella and Astoria blocks and were likely focused along deformation-related pathways of higher permeability. Sectors of low gold endowment have lower $\delta^{18}O_{H2O}$ and fluid/rock ratios, likely reflecting a larger proportion of upper crustal fluid and fluid-flow changes. Modelling of fluid flow shows that the larger proportion of upper crustal fluid in the less endowed sectors is due to 1) the less abundant metamorphic fluid that flowed in the thinner band of Piché Group rocks and 2) the presence of more porous rocks north of the CLLDZ, from which a larger quantity of pore fluid was drawn into the fault. We suggest that most of the variation of gold endowment is related to the variation of the gold-bearing metamorphic fluid flow along the segment. Less abundant or diluted metamorphic fluid flow decreases the gold potential along the CLLDZ.

Table des matières

Liste des figures

Liste des tableaux

Remerciements

Tout d'abord, un énorme merci à mon directeur, Georges Beaudoin, pour m'avoir fait confiance pour ce projet de maîtrise et pour ses nombreux conseils et explications à travers ces années. Je remercie également ma co-directrice, Crystal LaFlamme, pour ses commentaires et recommandations essentiels au projet, mais également pour ses mots d'encouragement qui ont su me garder motivé à travers les périodes plus difficiles. Leurs nombreuses connaissances ont définitivement contribué à enrichir le potentiel de ce projet. J'aimerais également remercier les professionnels de recherche Benoît Quesnel et Christophe Scheffer pour leur contribution indispensable tout au long du projet, mais surtout pour leur patience face à mes incessantes questions quotidiennes.

Merci au projet Metal Earth pour le soutien financier et à toute l'équipe de l'Université Laval pour la mémorable excursion en Abitibi et les enrichissantes réunions et discussions. Je remercie également Taus R. C. Jørgensen pour son introduction à la géologie de l'Abitibi et sa contribution à la mise sur pied du projet de maîtrise. Merci à toutes les personnes de la compagnie Ressources Yorbeau Inc., qui ont accepté gracieusement de partager le matériel et équipement nécessaires au projet, et qui ont rendu mon court séjour à Rouyn-Noranda des plus agréables. Un merci particulier à Baptiste Chapon et Sylvain Lépine pour leurs support et intérêt continus tout au long du projet. Merci à Jean-Philippe (JP) Séguin et Isaac Siles Malta pour leur aide sur le terrain. Je remercie également les professeurs John Molson et René Therrien de m'avoir dirigé dans le bon sens par rapport à l'aspect modélisation du travail. Merci au professeur Bertrand Rottier pour sa contribution au projet à travers la correction de mon devis de recherche, l'évaluation de mon séminaire et de ce mémoire. Pareillement, merci au professeur Ross Sherlock, de l'Université Laurentienne, pour l'évaluation du dépôt initial de ce mémoire. Je tiens à remercier Edmond Rousseau pour le soutien technique tout au long du projet, toujours dans la bonhomie.

J'aimerais remercier tous mes collègues et amis que j'ai côtoyés à l'université et qui ont su agrémenter mon parcours, je pense entre autres à Micheal (Michi), Isaac, François, Thierry-Karl et Sarah. Un merci spécial à ma copine Laura pour son soutien exceptionnel à travers ce projet, qui m'a aidé à décrocher et permis de garder ma tête pendant ces longs mois de télétravail.

Avant-propos

Le présent mémoire a été écrit sous forme d'article, en anglais, pour être soumis au journal Mineralium Deposita pour publication. L'article a été entièrement écrit par Guillaume Raymond, premier auteur, qui a également effectué l'échantillonnage, la préparation des échantillons, le traitement des données et leur interprétation. Les professeurs Georges Beaudoin (Université Laval), directeur de maîtrise, et Crystal LaFlamme (Université Laval), co-directrice, sont co-auteurs de l'article et ont contribué au niveau de la conception du projet, de l'interprétation des données et de la rédaction. Les professionnels de recherche Benoît Quesnel et Christophe Scheffer sont également co-auteurs et ont contribué sur le plan de la préparation des échantillons, l'interprétation des données et de la rédaction. Finalement, les professeurs René Therrien (Université Laval) et John Molson (Université Laval) sont aussi co-auteurs de l'article, où ils ont contribué au niveau de la conception du modèle, de l'interprétation et de la rédaction.

Introduction

Ce projet de maîtrise a été développé et financé par le projet Metal Earth, sous la supervision du professeur Georges Beaudoin et de la co-supervision de la professeure Crystal LaFlamme, du Centre E4M et du département de géologie et de génie géologique de l'Université Laval. Metal Earth est un programme de recherche en géologie des ressources minérales regroupant plusieurs chercheurs actifs au sein des secteurs académiques, publics et industriels. Les professionnels de recherche Benoît Quesnel et Christophe Scheffer et les professeurs René Therrien et John Molson du département de géologie et de génie géologique de l'Université Laval sont également d'importants collaborateurs au projet.

Problématique

Les gîtes d'or orogénique

Les gîtes d'or orogéniques, initialement définis par Bohlke (1982), se forment typiquement à la transition ductile-fragile dans des environnements tardiorogéniques, sous déformation en régime compressif à transpressionnel (Groves et al., 1998; Goldfarb et al., 2005; Goldfarb & Groves, 2015). Ils sont généralement encaissés dans des roches volcanosédimentaires, au faciès des schistes verts jusqu'au faciès des amphibolites, où la minéralisation est tardi-métamorphique (e.g., Goldfarb & Groves, 2015). La minéralisation aurifère est habituellement associée à des fluides H_2O-CO_2±CH_4 de faible salinité, cristallisant des veines de quartz-carbonate et autres minéraux, comme la tourmaline, chlorite, albite, biotite et muscovite à des températures entre 220 et 450 °C (Goldfarb et al., 2005; Neumayr et al., 2007; Jébrak & Marcoux, 2008; Goldfarb & Groves, 2015). L'or est transporté dans le fluide sous forme de complexes hydrosulfurés ou chlorurés (Shenberger & Barnes, 1989; Loucks & Mavrogenes, 1999; Tomkins, 2013; Pokrovski et al., 2015). Bien que ce type de gîte ait fait l'objet de nombreuses études au cours des dernières décennies, la source de ces fluides minéralisateurs demeure un sujet de débat (e.g., Goldfarb & Groves, 2015). En effet, plusieurs auteurs optent pour une origine métamorphique générée par dévolatilisation de roches en profondeur lors du métamorphisme prograde (e.g., Kerrich & Fryer, 1979; Kerrich & Fyfe, 1981; Ridley & Diamond, 2000; Beaudoin & Pitre, 2005; Pitcairn et al., 2006; Phillips & Powell, 2010; Goldfarb & Groves, 2015; Beaudoin & Chiaradia, 2016; Pitcairn et al., 2017; Quesnel et al., in press), d'autres pour une source magmato-hydrothermale (e.g., Ridley & Diamond, 2000; Bath et al., 2013; Tomkins, 2013; Xue et al., 2013) ou même une source mantellique associée à une zone de subduction (e.g., Xue et al., 2013; Groves et al., 2020a; Groves et al., 2020b). La majorité des gîtes d'or orogéniques est associée à des structures subsidiaires de zones de déformation trans-crustales majeures, qui ont servi de drains pour la remontée des fluides hydrothermaux dans la croûte terrestre après activité sismique (Sibson et al., 1988; Groves et al., 1998; Neumayr & Hagemann, 2002; Goldfarb et al., 2005; Beaudoin et al., 2006).

L'association fréquente de l'or aux failles de second et troisième ordres plutôt qu'aux zones de failles transcrustales implique la présence de processus locaux contrôlant l'enrichissement en or. Ces mécanismes ne sont par contre pas clairement établies et peuvent varier d'un gîte à l'autre. Généralement, la concentration préférentielle de l'or est associée à un déséquilibre du fluide, causé par un changement de ses conditions de circulation, venant déstabiliser les complexes sulfurés et ainsi précipiter l'or et les minéraux de veines. De tels déséquilibres sont généralement associés à des changements physico-chimiques du fluide, tels que 1) des variations de l'état d'oxydoréduction (e.g., Goldfarb et al., 2005; Neumayr et al., 2008; Hodkiewicz et al., 2009; Ward et al., 2017; LaFlamme et al., 2018) 2) l'évolution de la fugacité de l'oxygène et/ou du soufre (e.g., Goldfarb et al., 2005; Neumayr et al., 2008; Hodkiewicz et al., 2009; Ward et al., 2017; Gaboury, 2019) 3) des variations de température (e.g., Eisenlohr et al., 1989; Loucks & Mavrogenes, 1999; Dubé & Gosselin, 2007; Pokrovski et al., 2015) et 4) des changements du pH (e.g., Mccuaig & Kerrich, 1998; Goldfarb et al., 2005; Gaboury, 2019). Ces modifications des conditions physico-chimiques sont elles-mêmes induites par des processus tels que la vaporisation instantanée lors d'un relâchement de pression des fluides induit par des séismes (e.g., Sibson et al., 1988; Robert et al., 1995; Weatherley & Henley, 2013; Sugiono et al., 2022), un mélange de fluides (e.g., Uemoto et al., 2002; Boiron et al., 2003; Bateman & Hagemann, 2004; Beaudoin & Pitre, 2005; Neumayr et al., 2008; Beaudoin & Chiaradia, 2016) et/ou des interactions fluide-roche (e.g., Uemoto et al., 2002; Goldfarb et al., 2005; Evans et al., 2006; Hodkiewicz et al., 2009; Petrella et al., 2021). Les processus mentionnés ci-haut sont souvent associés à des changements de circulation des fluides. De variations importantes de température n'ont par contre pas encore été observées, et les faibles fluctuations de température au sein d'un même gîte, voire district, suggèrent que ce mécanisme n'est pas crucial pour la précipitation de l'or (Kishida & Kerrich, 1987; Mikucki & Heinrich, 1993; Ridley et al., 1996; Ridley & Diamond, 2000; Beaudoin & Pitre, 2005; Olivo et al., 2006; Beaudoin & Chiaradia, 2016).

Les isotopes stables de l'oxygène, hydrogène et du carbone sont des outils efficaces pour suivre l'évolution des conditions du fluide, à partir de l'analyse des minéraux contenus dans les veines. En effet, ils permettent d'observer des changements de température par géothermométrie à partir de couples minéraux en équilibre isotopique. Ces isotopes peuvent également être utilisés pour calculer la composition isotopique du fluide (H_2O et CO_2) cristallisant les minéraux, ce qui permet d'identifier les sources de fluides impliqués, en plus d'éclairer certains processus physiques comme le mélange de fluides et les cycles d'évaporation-condensation (e.g., Sheppard, 1986; Beaudoin & Pitre, 2005; Beaudoin & Chiaradia, 2016; Quesnel et al., in press). Les isotopes stables permettent également l'estimation quantitative des interactions fluide-roche (e.g., Taylor, 1978; Neumayr et al., 2007; Raskevicius et al., 2019). Finalement, plusieurs auteurs les ont utilisés pour simuler l'écoulement des fluides des systèmes hydrothermaux étudiés (Beaudoin & Therrien, 1999; Badertscher et al., 2002; Beaudoin et al., 2006; Savard et al., 2007).

Le segment Augmitto-Bouzan est un terrain idéal pour étudier les mécanismes liés à la concentration préférentielle de l'or, puisque la minéralisation aurifère est spatialement distribuée de manière irrégulière, concentrée à l'ouest plutôt qu'à l'est du segment. De plus, il s'agit d'un cas rare où le gîte se retrouve directement dans le plan d'une faille transcrustale de premier ordre : la zone de déformation Cadillac Larder-Lake. Celle-ci est génétiquement associée à plusieurs districts d'or orogénique, comme Matachewan, Kirkland Lake, Larder Lake, Rouyn-Noranda, Malartic et Val-d'Or (Robert, 1989; Poulsen, 2000; Poulsen et al., 2017). Le segment Augmitto-Bouzan couvre un tronçon de 12 km de long, où les premiers 6.5 km à l'ouest sont caractérisés par d'importantes teneurs aurifères à travers plusieurs colonnes minéralisées avec des ressources mesurées et indiquées de 247 000 tonnes à 6.08 g/t Au et ressources inférées de 633 000 à 7.79 g/t Au (Salmon & McDonough, 2011). Ces zones ont également bien été contraintes par des études lithologiques, structurales, pétrographiques, minéralogiques et géochimiques (e.g., Wilson, 1962; Kelly, 1988; Gauthier et al., 1990; Neumayr et al., 2007; Salmon & McDonough, 2011; Rafini, 2014; Laporte, 2016; Meng et al., 2020). La partie est du segment est presque complètement dépourvue de minéralisation aurifère, malgré les signes d'activité hydrothermale et peu ou pas d'étude y ont été faites.

Objectifs

Ce projet de maîtrise vise à comparer les processus locaux responsables de l'enrichissement en or en comparant les zones minéralisées et les zones peu minéralisées du segment Augmitto-Bouzan. Pour ce faire, les objectifs principaux du projet furent de :

1) Analyser la composition chimique des roches encaissantes et des carbonates et tourmalines des veines pour observer les variations chimiques entre les protolithes et les fluides hydrothermaux à travers la propriété.

2) Établir la température d'équilibre isotopique des minéraux de veines ainsi que la variation spatiale de ces valeurs.

3) Déterminer les sources des fluides (H_2O et CO_2) impliqués dans le système, la variation spatiale de celles-ci et les mécanismes affectant leur composition isotopique.

4) Définir les variations spatiales des rapports fluide/roche à partir du bilan de masse des isotopes stables de l'oxygène pour quantifier les interactions fluide-roche.

5) Modéliser en 3D le transport réactif des isotopes d'oxygène dans le fluide afin d'identifier un scénario d'écoulement pouvant répliquer les valeurs de $\delta^{18}O$ mesurées et ainsi comparer les conditions d'écoulement entre les secteurs dotés ou non en or.

Les résultats de ce travail apportent une meilleure compréhension des mécanismes d'enrichissement préférentiel de l'or le long du segment Augmitto-Bouzan, pouvant être extrapolés à d'autres gisements similaires. Ces éléments de réponse sont donc directement bénéfiques à la compagnie Ressources Yorbeau Inc., à l'industrie minérale et à la communauté scientifique en apportant une nouvelle compréhension des éléments responsables de la formation du gisement, en plus d'amener de nouvelles stratégies pour cibler la minéralisation dans des environnements analogues au segment Augmitto-Bouzan.

Méthodologie

Échantillonnage

Un total de 383 échantillons, veines et roches encaissantes confondues, à partir de forages et d'affleurements, a été collecté le long du segment afin de former la grille la plus régulière possible, latéralement et verticalement, dans les secteurs minéralisés et moins minéralisés. La mise sur pied d'une séquence paragénétique à partir des échantillons et des données de terrain a permis d'identifier les veines associées aux épisodes aurifères et ainsi réduire la sélection à 108 échantillons. Ceux-ci sont représentatifs et régulièrement espacés, afin de contraindre les variations de composition des minéraux et des fluides. De ceux-ci, 28 lames minces de veines de quartz-carbonate-tourmaline et quartz-carbonate ont été produites, afin de mesurer la composition chimique en éléments majeurs des carbonates et tourmalines à travers le segment. Un total de 33 roches encaissantes associées aux veines a été sélectionné en forage pour des analyses de roche totale des éléments majeurs et isotopes (O, C). Des lames minces de celles-ci ont été produites pour établir les proportions modales des phases minérales. Les échantillons comprennent: 23 roches volcaniques altérées du Groupe de Piché, 9 grauwackes du Groupe de Timiskaming et un dyke d'albitite. Parmi les roches du Groupe de Piché, 19 échantillons sont représentatifs de l'altération carbonate±fuchsite, deux de l'altération talc-chlorite-carbonate et deux de l'assemblage trémolite-chlorite. Les encaissants ont été sélectionnés afin d'être exempts de veines, homogènes et représentatifs de la zone. Un seul encaissant de grauwacke du Groupe de Timiskaming a été recueilli à approximativement 600 m au sud de la zone de déformation Cadillac Larder-Lake, en tant qu'échantillon représentatif de grauwacke non altéré pour analyse isotopique. L'oxydation de surface et les veinules ont été retirées des encaissants avant les analyses. Les teneurs en or proviennent de la compagnie Ressources Yorbeau Inc.

Méthodes analytiques

Analyses isotopiques

Des concentrés de quartz, tourmaline et carbonates ont été triés manuellement sous un microscope binoculaire afin de s'assurer de la pureté des concentrés. Les échantillons ont ensuite été réduits en poudre à l'aide d'un mortier et d'un pilon. Entre 7 et 10 mg de poudre d'échantillon ont été utilisés pour chaque analyse.

Un peu plus de 10 mg ont été utilisés pour les échantillons de roche encaissante, préalablement réduits en poudre au concasseur à mâchoire et au broyeur gravitaire. L'oxygène a été analysé en suivant le protocole de Clayton et Mayeda (1963) au laboratoire de géochimie isotopique de l'Université Laval, Québec, Canada. L'oxygène libéré a été passé à travers une tige de carbone chauffée, afin d'être converti en dioxyde de carbone. La composition isotopique du CO_2 a ensuite été mesurée par spectromètre de masse à ratios isotopiques de marque Micromass modèle Isoprime au Laboratoire de géochimie des isotopes stables légers du Geotop, UQAM, Montréal, Canada. Les rapports isotopiques de l'oxygène sont rapportés dans la notation δ en ‰ par rapport à V-SMOW, avec une précision de 0.2 ‰. La précision et l'exactitude ont été vérifiées par des analyses répétées du standard de quartz international NBS28 (9.6 ± 0.2 ‰) et du standard de quartz interne K-1 (19.2 ± 0.2 ‰).

Les compositions isotopiques en hydrogène de la tourmaline et du carbone et oxygène des phases carbonatées des roches encaissantes et veines ont été mesurées au *Queen's Facility for Isotopic Research*, Queens Univeristy, Kingston, Canada. Pour les phases carbonatées, 20 mg de matériel était nécessaire pour les analyses de roche totale et 1 mg pour les carbonates purs. Ceux-ci ont ensuite été mis en réaction avec de l'acide phosphorique anhydre pendant 4 heures à 72 °C et le CO_2 relâché a été analysé par un système de Gas Bench Thermo-Finnigan, couplé à un spectromètre de masse à flux continu Thermo-Finnigan Delta^{Plus} XP. Les isotopes d'oxygène et de carbone sont rapportés dans la notation δ en ‰ par rapport à V-SMOW et V-PDB, respectivement, les deux avec une précision de 0.2 ‰. Comme les analyses ont été calibrées en fonction d'un standard de calcite, un facteur de correction de –1.2 ‰ a été ajouté aux valeurs de $\delta^{18}O$ des échantillons de veines dolomitiques, basé sur les fractionnements carbonate-HPO_3 de Rosenbaum and Sheppard (1986) et Sharma et al. (2002) à 72 °C. Pour la tourmaline, les échantillons ont été dégazés pendant une heure à 100 °C dans des capsules d'argent. Les compositions isotopiques de l'hydrogène ont été mesurées à partir d'un analyseur thermochimique couplé à un spectromètre de masse à flux continu Thermo-Finnigan Delta^{Plus} XP. Les rapports isotopiques de l'hydrogène sont rapportés dans la notation δ en ‰ par rapport à V-SMOW, avec une précision de 3 ‰.

Chimie minérale

Les éléments majeurs de la tourmaline et des carbonates ont été mesurés au Laboratoire de microanalyse de l'Université Laval, Québec, Canada, avec une microsonde électronique CAMECA SX-100. La tourmaline a été analysée pour les éléments suivants (Fe, Cr, Ca, Na, Mg, Si, Al, Mn, Ti et K) sous un voltage de 15 keV, un courant de 20 nA et un faisceau de 5 µm. Les éléments majeurs des carbonates (Fe, Ca, Mg, Mn et Sr) ont été analysés sous un voltage de 15 keV, un courant de 20 nA et un faisceau de 10 µm. Les données de la tourmaline ont été converties en atomes par unité de formule (apfu) pour 29 oxygènes, selon Henry et al. (2011).

Lithogéochimie

La lithogéochimie des roches totales des encaissants a été effectué laboratoires ALS, Vancouver, Canada. Les échantillons sous forme de poudre ont été soumis à une digestion à l'eau régale et ensuite analysés pour les éléments majeurs suivants (Si, Al, Ca, Mg, Na, K, Ti, Fe, Mn, P, Cr, Sr, et Ba) par utilisation d'un spectromètre d'émission atomique à plasma à couplage inductif. L'eau de cristallisation a été analysée en plaçant les échantillons dans un four à combustion, pour être ensuite mesurée par spectrométrie infrarouge. Les concentrations de CO_2 ont été mesurées par un coulomètre à CO_2 après digestion des échantillons par $HClO_4$. Les teneurs en C et S totaux ont été mesurées par combustion des échantillons dans un four Leco. Les résultats sous les limites de détection correspondent à 6 % des données et ont été remplacés par la valeur de la limite de détection divisée par la racine carrée de deux, selon Croghan et Egeghy (2003).

Modélisation 3D de l'écoulement des fluides hydrothermaux

Le modèle utilisé lors de ce travail est une version modifiée du modèle tridimensionnel d'écoulement à saturation variable et transport de soluté de Therrien and Sudicky (1996), adapté par Beaudoin et al. (2006) pour simuler l'écoulement des fluides et le transport et les réactions des isotopes d'oxygène dans des matériaux géologiques fracturés. Le modèle numérique 3D a été produit à l'aide du logiciel Hydrogeosphere par Aquanty.

Bibliographie

Badertscher, N. P., Beaudoin, G., Therrien, R., & Burkhard, M. (2002). Glarus overthrust: A major pathway for the escape of fluids out of the Alpine orogen. *Geology, 30*(10), 875-878.

Bateman, R., & Hagemann, S. (2004). Gold mineralisation throughout about 45 Ma of Archaean orogenesis: protracted flux of gold in the Golden Mile, Yilgarn craton, Western Australia. *Mineralium Deposita, 39*(5), 536-559.

Bath, A. B., Walshe, J. L., Cloutier, J., Verrall, M., Cleverley, J. S., Pownceby, M. I., . . . Nortje, G. S. (2013). Biotite and apatite as tools for tracking pathways of oxidized fluids in the Archean East Repulse gold deposit, Australia. *Economic Geology, 108*(4), 667-690.

Beaudoin, G., & Chiaradia, M. (2016). Fluidmixing in orogenic gold deposits: Evidence from the H-O-Sr isotope composition of the Val-d'Or vein field (Abitibi, Canada). *Chemical Geology, 437*, 7-18. doi:10.1016/j.chemgeo.2016.05.009

Beaudoin, G., & Pitre, D. (2005). Stable isotope geochemistry of the Archean Val-d'Or (Canada) orogenic gold vein field. *Mineralium Deposita, 40*(1), 59-75. doi:10.1007/s00126-005-0474-z

Beaudoin, G., & Therrien, R. (1999). Sources and drains: Major controls of hydrothermal fluid flow in the Kokanee Range, British Columbia, Canada. *Geology, 27*(10), 883-886.

Beaudoin, G., Therrien, R., & Savard, C. (2006). 3D numerical modelling of fluid flow in the Val-d'Or orogenic gold district: major crustal shear zones drain fluids from overpressured vein fields. *Mineralium Deposita, 41*(1), 82-98. doi:10.1007/s00126-005-0043-5

Bohlke, J. K. (1982). Orogenic (metamorphic-hosted) gold-quartz veins. *US Geological Survey Open-File Report, 795*, 70-76.

Boiron, M.-C., Cathelineau, M., Banks, D. A., Fourcade, S., & Vallance, J. (2003). Mixing of metamorphic and surficial fluids during the uplift of the Hercynian upper crust: consequences for gold deposition. *Chemical Geology, 194*(1-3), 119-141.

Clayton, R. N., & Mayeda, T. K. (1963). The use of bromine pentafluoride in the extraction of oxygen from oxides and silicates for isotopic analysis. *Geochimica Et Cosmochimica Acta, 27*(1), 43-52.

Croghan, C., & Egeghy, P. P. (2003). Methods of dealing with values below the limit of detection using SAS. *Southern SAS User Group, 22*, 24.

Dubé, B., & Gosselin, P. (2007). Greenstone-hosted quartz-carbonate vein deposits. In W. D. Goodfellow (Ed.), *Mineral Deposits of Canada: A Synthesis of Major Deposit-Types, District Metallogeny, the Evolution of Geological Provinces and Exploration Methods* (Vol. 5, pp. 49-73): Geological Association of Canada, Mineral Deposit Division.

Eisenlohr, B., Groves, D., & Partington, G. (1989). Crustal-scale shear zones and their significance to Archaean gold mineralization in Western Australia. *Mineralium Deposita, 24*(1), 1-8.

Evans, K., Phillips, G., & Powell, R. (2006). Rock-buffering of auriferous fluids in altered rocks associated with the Golden Mile-style mineralization, Kalgoorlie gold field, Western Australia. *Economic Geology, 101*(4), 805-817.

Gaboury, D. (2019). Parameters for the formation of orogenic gold deposits. *Applied Earth Science, 128*(3), 124-133.

Gauthier, N., Rocheleau, M., Kelly, D., & Gagnon, Y. (1990). Controls on the distribution of gold mineralization within the Cadillac tectonic zone, Rouyn-Beauchastel segment, Abitibi Belt, Quebec. In M. Rive, Y. Verpaelst, Y. Gagnon, J. M. Lulin, R. G, & A. Simard (Eds.), *La ceinture polymétallique du Nord-Ouest Québécois* (Vol. 43, pp. 185-198): L'institut canadien des mines et de la métallurgie.

Goldfarb, R. J., Baker, T., Dubé, B., Groves, D. I., Hart, C. J. R., Gosselin, P., . . . Richards, J. P. (2005). Distribution, Character, and Genesis of Gold Deposits in Metamorphic Terran. In *One Hundredth Anniversary Volume* (pp. 0): Society of Economic Geologists.

Goldfarb, R. J., & Groves, D. I. (2015). Orogenic gold: Common or evolving fluid and metal sources through time. *Lithos, 233*, 2-26. doi:10.1016/j.lithos.2015.07.011

Groves, D. I., Goldfarb, R. J., Gebre-Mariam, M., Hagemann, S. G., & Robert, F. (1998). Orogenic gold deposits: a proposed classification in the context of their crustal distribution and relationship to other gold deposit types. *Ore Geology Reviews, 13*(1-5), 7-27.

Groves, D. I., Santosh, M., Deng, J., Wang, Q., Yang, L., & Zhang, L. (2020a). A holistic model for the origin of orogenic gold deposits and its implications for exploration. *Mineralium Deposita, 55*(2), 275-292.

Groves, D. I., Santosh, M., & Zhang, L. (2020b). A scale-integrated exploration model for orogenic gold deposits based on a mineral system approach. *Geoscience Frontiers, 11*(3), 719-738.

Henry, D. J., Novák, M., Hawthorne, F. C., Ertl, A., Dutrow, B. L., Uher, P., & Pezzotta, F. (2011). Nomenclature of the tourmaline-supergroup minerals. *American Mineralogist, 96*(5-6), 895-913.

Hodkiewicz, P. F., Groves, D. I., Davidson, G. J., Weinberg, R. F., & Hagemann, S. G. (2009). Influence of structural setting on sulphur isotopes in Archean orogenic gold deposits, Eastern Goldfields Province, Yilgarn, Western Australia. *Mineralium Deposita, 44*(2), 129-150. doi:10.1007/s00126-008-0211-5

Kelly, D. (1988). Recent developments in Yorbeau‘s Astoria Property Rouyn-Noranda area, Quebec. *Gold Mining, 88*, 468-481.

Kerrich, R., & Fryer, B. (1979). Archaean precious-metal hydrothermal systems, Dome Mine, Abitibi Greenstone Belt. II. REE and oxygen isotope relations. *Canadian Journal of Earth Sciences, 16*(3), 440-458.

Kerrich, R., & Fyfe, W. (1981). The gold—carbonate association: source of CO2, and CO2 fixation reactions in Archaean lode deposits. *Chemical Geology, 33*(1-4), 265-294.

Kishida, A., & Kerrich, R. (1987). Hydrothermal alteration zoning and gold concentration at the Kerr-Addison Archean lode gold deposit, Kirkland Lake, Ontario. *Economic Geology, 82*(3), 649-690. doi:10.2113/gsecongeo.82.3.649

LaFlamme, C., Sugiono, D., Thebaud, N., Caruso, S., Fiorentini, M., Selvaraja, V., . . . Martin, L. (2018). Multiple sulfur isotopes monitor fluid evolution of an Archean orogenic gold deposit. *Geochimica Et Cosmochimica Acta, 222*, 436-446. doi:10.1016/j.gca.2017.11.003

Laporte, J. (2016). *Mineralogical study of the auriferous shear zone along the Augmitto-Astoria segment in the Cadillac break south to Rouyn-Noranda, Abitibi, Quebec.* (Master's thesis). Université du Québec à Montréal, Montreal (Québec, Canada). Retrieved from http://archipel.uqam.ca/id/eprint/8699

Loucks, R. R., & Mavrogenes, J. A. (1999). Gold solubility in supercritical hydrothermal brines measured in synthetic fluid inclusions. *Science, 284*(5423), 2159-2163.

Mccuaig, C., & Kerrich, R. (1998). P-T-t-deformation-fluid characteristics of lode gold deposits: evidence from alteration systematics. *Ore Geology Reviews, 12*, 381-453.

Meng, Y.-M., Jébrak, M., Sasseville, C., & Huang, X.-W. (2020). Geochemical and mineralogical diagnosis on gold ores: A case study from the Cadillac–Larder Lake Fault Zone, Abitibi, Canada. *Ore Geology Reviews, 127*, 103840.

Mikucki, E., & Heinrich, C. (1993). *Vein-and mine-scale wall-rock alteration and gold mineralisation in the Archaean Mount Charlotte deposit, Kalgoorlie, Western Australia.* Paper presented at the Vein-and mine-scale wall-rock alteration and gold mineralisation in the Archaean Mount Charlotte deposit, Kalgoorlie, Western Australia.

Neumayr, P., & Hagemann, S. G. (2002). Hydrothermal fluid evolution within the Cadillac tectonic zone, Abitibi greenstone belt, Canada: Relationship to auriferous fluids in adjacent second- and third-order shear zones. *Economic Geology and the Bulletin of the Society of Economic Geologists, 97*(6), 1203-1225. doi:10.2113/97.6.1203

Neumayr, P., Hagemann, S. G., Banks, D. A., Yardley, B. W. D., Couture, J. F., Landis, G. P., & Rye, R. (2007). Fluid chemistry and evolution of hydrothermal fluids in an Archaean transcrustal fault zone network: the case of the Cadillac Tectonic Zone, Abitibi greenstone belt, Canada. *Canadian Journal of Earth Sciences, 44*(6), 745-773. doi:10.1139/e06-130

Neumayr, P., Walshe, J., Hagemann, S., Petersen, K., Roache, A., Frikken, P., . . . Halley, S. (2008). Oxidized and reduced mineral assemblages in greenstone belt rocks of the St. Ives gold camp, Western Australia: vectors to high-grade ore bodies in Archaean gold deposits? *Mineralium Deposita, 43*(3), 363-371.

Olivo, G. R., Chang, F., & Kyser, T. K. (2006). Formation of the auriferous and barren North Dipper Veins in the Sigma Mine, Val d'Or, Canada: constraints from structural, mineralogical, fluid Inclusion, and isotopic data. *Economic Geology, 101*(3), 607-631.

Petrella, L., Thébaud, N., Evans, K., LaFlamme, C., & Occhipinti, S. (2021). The role of competitive fluid-rock interaction processes in the formation of high-grade gold deposits. *Geochimica Et Cosmochimica Acta, 313*, 38-54.

Phillips, G., & Powell, R. (2010). Formation of gold deposits: a metamorphic devolatilization model. *Journal of Metamorphic Geology, 28*(6), 689-718.

Pitcairn, I., Leventis, N., Beaudoin, G., & Dubé, B. (2017). *A metasedimentary source for orogenic gold in the Abitibi belt?*

Pitcairn, I. K., Teagle, D. A., Craw, D., Olivo, G. R., Kerrich, R., & Brewer, T. S. (2006). Sources of metals and fluids in orogenic gold deposits: insights from the Otago and Alpine Schists, New Zealand. *Economic geology, 101*(8), 1525-1546.

Pokrovski, G. S., Kokh, M. A., Guillaume, D., Borisova, A. Y., Gisquet, P., Hazemann, J. L., . . . Dubessy, J. (2015). Sulfur radical species form gold deposits on Earth. *Proceedings of the National Academy of Sciences of the United States of America, 112*(44), 13484-13489. doi:10.1073/pnas.1506378112

Poulsen, K. H. (2000). Geological classification of Canadian gold deposits. *Bulletin of the Geological Survey of Canada, 540*, 1-106.

Poulsen, K. H., Monecke, T., Mercier-Langevin, P., & Dubé, B. (2017). The Larder Lake-Cadillac Break and Its Gold Districts. In *Archean Base and Precious Metal Deposits, Southern Abitibi Greenstone Belt, Canada* (Vol. 19, pp. 0): Society of Economic Geologists.

Quesnel, B., Scheffer, C., & Beaudoin, G. (in press). The light stable isotope (H, B, C, N, O, Si, S) composition of orogenic gold deposits. In *Isotopes in mineral exploration*: SpringerNature.

Rafini, S. (2014). Fiches descriptives de gîtes – Faille de Cadillac. Projet CONSOREM 2011-01 et 2012-01. 187.

Raskevicius, T., Beaudoin, G., Kyser, K., Perrouty, S., & Gaillard, N. (2019). Whole-rock δ2H and δ18O footprint of the Canadian Malartic gold deposit, Pontiac Subprovince, Québec, Canada. *Mineralium Deposita*, 1-18.

Ridley, J., Mikucki, E., & Groves, D. (1996). Archean lode-gold deposits: fluid flow and chemical evolution in vertically extensive hydrothermal systems. *Ore Geology Reviews, 10*(3-6), 279-293.

Ridley, J. R., & Diamond, L. (2000). Fluid chemistry of orogenic lode gold deposits and implications for genetic models. In S. G. Hagemann & P. Brown (Eds.), *Gold in 2000* (Vol. 13, pp. 141-162): Society of Economic Geologists, Inc.

Robert, F. (1989). Internal structure of the Cadillac tectonic zone southeast of Val d'Or, Abitibi greenstone belt, Quebec. *Canadian Journal of Earth Sciences, 26*(12), 2661-2675. doi:10.1139/e89-226

Robert, F., Boullier, A. M., & Firdaous, K. (1995). Gold-quartz veins in metamorphic terranes and their bearing on the role of fluids in faulting. *Journal of Geophysical Research: Solid Earth, 100*(B7), 12861-12879.

Rosenbaum, J., & Sheppard, S. (1986). An isotopic study of siderites, dolomites and ankerites at high temperatures. *Geochimica Et Cosmochimica Acta, 50*(6), 1147-1150.

Salmon, B., & McDonough, B. (2011). *Technical report on the Rouyn property,-Rouyn-Noranda, Québec, Canada*. Retrieved from https://www.yorbeauresources.com/document/en/2089-TechnicalReport.pdf

Savard, C., Beaudoin, G., & Therrien, R. (2007). Numerical modelling of 3D fluid flow and oxygen isotope exchange in fractured media: spatial distribution of isotope patterns. *Geofluids, 7*(4), 387-400.

Sharma, S. D., Patil, D., & Gopalan, K. (2002). Temperature dependence of oxygen isotope fractionation of CO2 from magnesite-phosphoric acid reaction. *Geochimica Et Cosmochimica Acta, 66*(4), 589-593.

Shenberger, D., & Barnes, H. (1989). Solubility of gold in aqueous sulfide solutions from 150 to 350 C. *Geochimica Et Cosmochimica Acta, 53*(2), 269-278.

Sheppard, S. M. (1986). Characterization and isotopic variations in natural waters. *Stable isotopes in high temperature geological processes*, 165-184.

Sibson, R. H., Robert, F., & Poulsen, K. H. (1988). High-angle reverse faults, fluid-pressure cycling, and mesothermal gold-quartz deposits. *Geological Society of America, 16*(6), 551-555. doi:10.1130/0091-7613(1988)016<0551:Harffp>2.3.Co;2

Sugiono, D., LaFlamme, C., Thébaud, N., Martin, L., Savard, D., & Fiorentini, M. (2022). Fault-induced gold saturation of a single auriferous fluid is a key process for orogenic gold deposit formation. *Economic Geology*.

Taylor, H. P. J. (1978). Oxygen and hydrogen isotope studies of plutonic granitic rocks. *Earth and Planetary Science Letters, 38*(1), 177-210. doi:10.1016/0012-821x(78)90131-0

Therrien, R., & Sudicky, E. (1996). Three-dimensional analysis of variably-saturated flow and solute transport in discretely-fractured porous media. *Journal of Contaminant Hydrology, 23*(1-2), 1-44.

Tomkins, A. G. (2013). On the source of orogenic gold. *Geology, 41*(12), 1255-1256. doi:10.1130/focus122013.1

Uemoto, T., Ridley, J., Mikucki, E., Groves, D. I., & Kusakabe, M. (2002). Fluid chemical evolution as a factor in controlling the distribution of gold at the Archean Golden Crown lode gold deposit, Murchison province, Western Australia. *Economic Geology, 97*(6), 1227-1248.

Ward, J., Mavrogenes, J., Murray, A., & Holden, P. (2017). Trace element and sulfur isotopic evidence for redox changes during formation of the Wallaby Gold Deposit, Western Australia. *Ore Geology Reviews, 82*, 31-48.

Weatherley, D. K., & Henley, R. W. (2013). Flash vaporization during earthquakes evidenced by gold deposits. *Nature Geoscience, 6*(4), 294-298.

Wilson, M. E. (1962). *Rouyn-Beauchastel Map-areas, Quebec*: Geological Survey of Canada.

Xue, Y. X., Campbell, I., & Ireland, T. R. (2013). No mass-independent sulfur isotope fractionation in auriferous fluids supports a magmatic origin for Archean gold deposits. *Geology, 41*(7), 791-794. doi:10.1130/g34186.1

Chapitre 1- Constraints on gold endowment along the Augmitto-Bouzan segment (Abitibi subprovince, Quebec) orogenic gold deposit, from stable isotopes (O, C, H) and 3D fluid flow modelling

1.1 Résumé

Augmitto-Bouzan est un segment de la zone de déformation Cadillac Larder-Lake de 12 km de long à Rouyn-Noranda (Québec, Canada) caractérisé par une distribution irrégulière de sa minéralisation aurifère. Ses veines de quartz-carbonate±tourmaline sont majoritairement encaissées dans les roches komatiitiques dans la zone de déformation Cadillac Larder-Lake. Les températures d'équilibre quartz-tourmaline y montrent un gradient thermique vertical (~30°C/100m). Ce gradient et les valeurs calculées de $\delta^{18}O_{H2O}$ et δD_{H2O} sont interprétés comme le résultat du mélange entre un fluide métamorphique profond de haute température, haut $\delta^{18}O$ et bas δD, et un fluide interstitiel de la croûte supérieure de basse température, bas $\delta^{18}O$ et haut δD. Les zones minéralisées du segment sont associées à une plus grande contribution de fluide métamorphique liée à un flux important facilité par la zone de déformation plus épaisse et à des épontes localement plus perméables. L'or serait donc associé au fluide métamorphique, où la contribution de fluide interstitiel viendrait diminuer le potentiel économique du fluide.

1.2 Abstract

Augmitto-Bouzan is a 12 km long segment of the Cadillac Larder-Lake deformation zone (CLLDZ) in Rouyn-Noranda (Québec, Canada) characterized by an uneven distribution of gold mineralization, hosted in veins and stockworks dominated by quartz-carbonate±tourmaline. These veins are mostly hosted in the Piché Group, recognized as the physical expression of the CLLDZ. The western 6.5 km section (Augmitto-Astoria) contains most of the gold mineralization, and the eastern 5.5 km (East-Bay and Bouzan) are almost completely gold barren. This study compares the past fluid flow conditions between these two variable gold-endowed sectors to identify processes responsible for contrasting gold endowment in the area.

Quartz ($\delta^{18}O$: 11.8-16.8‰), tourmaline ($\delta^{18}O$: 8.5-11.9‰; δD: –59- –18‰) and carbonate ($\delta^{18}O$: 11.3-15‰; $\delta^{13}C$: –6.2- –2.8‰) veins are mainly hosted in the Piché Group ($\delta^{18}O$: 7.3-11.7‰) which consist of komatiitic rocks strongly affected by a carbonate±fuchsite alteration. Quartz and tourmaline display equilibrium temperatures (228-420°C) that define a high vertical thermal gradient (~30°C/100m) within the Piché Group rocks. Covariation between temperature and computed $\delta^{18}O_{H2O}$ (4.4-10.8‰) and δD_{H2O} (–29-43‰) is interpreted to result from mixing between a deep-seated metamorphic fluid of high temperature (>420°C), high $\delta^{18}O$ (>10.8‰) and low δD (<–29‰) and an upper crustal pore fluid of low temperature (<230°C), low $\delta^{18}O$ (<4‰)

and a δD around 0‰. The higher δD_{H2O} (up to 43‰) values are likely associated with flash vaporization and condensation cycles related to the fault-valve mechanism forming the veins. Assuming the $\delta^{13}C$ composition of carbonate minerals is near the composition of the CO_2 source, a metamorphic origin is plausible. Reactive transport of oxygen with temperature-dependent fluid-rock isotope fractionation assuming a linear vertical temperature gradient within the CLLDZ domain is simulated using a 3D numerical model. Local upwellings of deep-seated fluid, evidenced by interpolation of $\delta^{18}O_{H2O}$, are observed in the Augmitto-Cinderella and Astoria blocks and were likely focused along higher permeability deformation-related pathways. Sectors of low gold endowment have lower $\delta^{18}O_{H2O}$ and fluid/rock ratios, likely reflecting a larger proportion of upper crustal pore fluid and fluid-flow changes. Modelling of fluid flow shows that the larger proportion of upper crustal fluid in the less endowed sectors is due to 1) the less abundant metamorphic fluid that flowed in the thinner band of Piché Group rocks and 2) the presence of more porous rocks north of the CLLDZ, from which a larger amount of pore fluid was drawn into the fault. Incorporation of upper crustal fluid also correlates with higher Fe, Mg, and Ca contents in vein carbonate and tourmaline. In this study, we suggest that most of the variation in gold endowment is related to the variation in the amount of gold-bearing metamorphic fluids along the segment. Less abundant or diluted metamorphic fluids decrease the gold potential of the Augmitto-Bouzan segment, and likely in other poorly gold-endowed areas along the CLLDZ.

1.3 Introduction

Quartz-carbonate veins, with other minerals such as tourmaline, are typical of orogenic gold deposits worldwide, commonly formed near the brittle-ductile transition within late-orogenic tectonic environments (Goldfarb et al., 2005; Goldfarb & Groves, 2015). The structurally controlled veins crystallized from low salinity H_2O-CO_2 ± CH_4 fluids at temperatures of 220 to 450 °C and are hosted in greenschist to amphibolite facies rocks (Goldfarb et al., 2005; Goldfarb & Groves, 2015). Even though the specific source(s) of the fluids is still debated, most authors generally agree with a deep metamorphic origin generated from devolatilization of rocks at depth during prograde metamorphism (e.g., Kerrich & Fryer, 1979; Kerrich & Fyfe, 1981; Beaudoin & Pitre, 2005; Pitcairn et al., 2006; Phillips & Powell, 2010; Goldfarb & Groves, 2015; Beaudoin & Chiaradia, 2016; Pitcairn et al., 2017; Quesnel et al., in press). Most orogenic gold deposits are associated with subsidiary fault zones of major trans-crustal deformation zones, which served as conduits for the hydrothermal fluid to ascend into the upper level of the crust during seismic activity (Sibson et al., 1988; Groves et al., 1998; Neumayr & Hagemann, 2002; Goldfarb et al., 2005; Beaudoin et al., 2006).

The association of gold with second and third-order faults, rather than in the trans-crustal structures, implies the presence of local processes that control gold endowment (Goldfarb et al., 2005). These processes are related to the destabilization of the gold-carrying complexes, leading to the precipitation of gold and vein minerals. These mechanisms are usually associated with changes in the physicochemical properties of the mineralizing fluids, such as 1) redox state variations (e.g., Goldfarb et al., 2005; Neumayr et al., 2008; Hodkiewicz et al., 2009; Ward et al., 2017; LaFlamme et al., 2018) 2) evolving oxygen and/or sulfur fugacity (e.g., Goldfarb et al., 2005; Neumayr et al., 2008; Hodkiewicz et al., 2009; Fougerouse et al., 2016; Ward et al., 2017; Gaboury, 2019) 3) variations of temperature (e.g., Eisenlohr et al., 1989; Loucks & Mavrogenes, 1999; Dubé & Gosselin, 2007; Pokrovski et al., 2015), and 4) pH changes (e.g., McCuaig & Kerrich, 1998; Goldfarb et al., 2005; Gaboury, 2019). These modifications of the physicochemical properties are themselves driven by processes like flash vaporization during seismic-induced fluid pressure release events (e.g., Sibson et al., 1988; Robert et al., 1995; Weatherley & Henley, 2013; Sugiono et al., 2022), fluid mixing (e.g., Uemoto et al., 2002; Boiron et al., 2003; Bateman & Hagemann, 2004; Beaudoin & Pitre, 2005; Neumayr et al., 2008; Beaudoin & Chiaradia, 2016), and/or fluid-rock interactions (e.g., Uemoto et al., 2002; Goldfarb et al., 2005; Evans et al., 2006; Hodkiewicz et al., 2009; Petrella et al., 2021). The aforementioned processes are also often related to local changes in fluid flow. Important variations of temperature have, however, not yet been observed, and the small fluctuations of temperature within a deposit, and even district, often discard temperature variation as a key process in gold precipitation (Kishida & Kerrich, 1987; Mikucki & Heinrich, 1993; Ridley et al., 1996; Ridley & Diamond, 2000; Beaudoin & Pitre, 2005; Olivo et al., 2006; Beaudoin & Chiaradia, 2016).

Oxygen, hydrogen, and carbon stable isotopes are efficient tools to monitor changes in the fluid's conditions from analyses of vein minerals and host rocks. They can be used to monitor temperature variations via geothermometry of vein mineral pairs in isotopic equilibrium. They can be utilized to compute the composition of the fluids that crystallized the minerals, which helps decipher the sources and physical processes involved, such as mixing and phase separation (Sheppard, 1986; Beaudoin & Pitre, 2005; Beaudoin & Chiaradia, 2016; Quesnel et al., in press). They also enable quantitative fluid/rock ratio calculations (Taylor, 1978; Neumayr et al., 2007; Raskevicius et al., 2019). Additionally, several authors have used stable isotopes to simulate the fluid flow of the studied hydrothermal systems (e.g., Beaudoin & Therrien, 1999; Badertscher et al., 2002; Beaudoin et al., 2006; Savard et al., 2007).

The Augmitto-Bouzan segment is a fitting study area to investigate the mechanisms related to gold endowment since mineralization is only distributed on the western side of the segment and the eastern side is nearly barren. Additionally, it is a rare case of orogenic gold deposits directly located in the plane of a first-order trans-crustal fault zone: the Cadillac Larder-Lake Deformation Zone (CLLDZ). The CLLDZ is genetically associated with multiple orogenic gold districts such as Matachewan, Kirkland Lake, Larder Lake, Rouyn-Noranda, Malartic, and Val-d'Or (Robert, 1989; Poulsen, 2000; Poulsen et al., 2017). The Augmitto-Bouzan segment is 12 km long, where the western 6.5 km are characterized by high gold contents following multiple oreshoots with measured and indicated resources of 247 000 tonnes at 6.08 g/t Au and inferred resources at 633 000 at 7.79 g/t Au (Salmon & McDonough, 2011). The eastern part of the segment is almost completely barren despite signs of hydrothermal activity.

Using stable isotopes of oxygen, carbon, and hydrogen, we attempt to identify local processes responsible for the gold endowment by comparing the different sectors of the Augmitto-Bouzan segment. We investigate the spatial variation of fluid sources, temperature of vein formation, the physical processes that affected their isotopic compositions, and quantification of the fluid-rock interactions. We also compare the geochemical composition of host rocks using whole-rock lithogeochemistry to identify spatial variations of protoliths and alterations. A 3D model of oxygen isotope reactive transport in coupled variable permeability media along the segment is used to better understand the fluid-flow patterns responsible for the spatial variation of the fluid's isotopic composition and, ultimately, the irregularly distributed gold mineralization.

1.4 Geological setting

1.4.1 Regional geology

The Augmitto-Bouzan segment is located near the boundary of two Archean domains, the Abitibi and the Pontiac subprovinces, parts of the Superior Province, Canada (Fig. 1). In Val-d'Or, Quebec, the two subprovinces are separated by the Cadillac Larder-Lake Deformation Zone, a subvertical and east-trending

Archean shear zone over 250 km long with a curvilinear trace that extends to Matachewan, Ontario (Fig. 1; Card, 1990; Powell, 1991; Robert et al., 1995; Daigneault et al., 2002; Bedeaux et al., 2017; Poulsen et al., 2017). To the north, the Abitibi greenstone belt is one of the world's largest Neoarchean terranes of supracrustal rocks (Card, 1990; Monecke et al., 2017). The belt is composed of multiple east-trending sequences of folded volcano-sedimentary rocks intruded by several synvolcanic, syn-tectonic, and post-tectonic plutonic rocks (Card, 1990; Thurston, 2015; Dubé & Mercier-Langevin, 2020). Volcanic activity repeatedly occurred from 2750 to 2675 Ma, resulting in komatiites and tholeiitic basalts, as well as calc-alkaline mafic to felsic lavas and related intrusions (Ayer et al., 2002). Studies of these different assemblages suggest they originated from an evolving volcanic arc environment affected by mantle plume magmatism (Bédard & Ludden, 1997; Kerrich et al., 1999; Ayer et al., 2002; Wyman et al., 2002; Wyman & Kerrich, 2009). South of the CLLDZ, the < 2682 Ma Pontiac Group (Mortensen, 1993; Davis, 2002; Percival, 2007; Frieman, 2018) of the Pontiac subprovince is dominated by metasedimentary schists and paragneisses derived mostly from turbiditic greywackes (Percival, 2007). They have been interpreted as synorogenic flysch sedimentary rocks from a foreland basin accretionary wedge complex (Card, 1990; Daigneault et al., 2002; Davis, 2002) or as an extensional basin (Rehm et al., 2021).

The juxtaposition of the two subprovinces occurred by thrusting of the Abitibi subprovince over the south verging fold-thrust belt Pontiac subprovince (Benn et al., 1994; Calvert & Ludden, 1999; Percival, 2007) along the CLLDZ. The 2680-2673 Ma Timiskaming Group unconformably overlies the previously deposited volcanic strata of the Abitibi subprovince and is mainly composed of fluvial alluvial conglomerates and sandstones (Hyde, 1980; Mueller et al., 1991; Mueller & Donaldson, 1992; Born, 1996; Davis, 2002; Poulsen et al., 2017; Frieman, 2018). At least four deformation phases affected the rocks of the Abitibi. The first (D_1) and second (D_2) phases of deformation are characterized by folds and structures that predate Timiskaming deposition and are generally overprinted by the third phase of deformation (D_3; Dubé & Mercier-Langevin, 2020). The latter, locally referred to as D_2 in the literature, is recorded as a north-south shortening that led to the formation of an east-striking penetrative foliation and folding (Dubé & Mercier-Langevin, 2020). The D_3 phase is the main stage of regional deformation of the Abitibi greenstone belt, post-dating Timiskaming deposition, and is responsible for its first-order and east-trending fault zones (Dubé & Mercier-Langevin, 2020). Finally, the last recorded deformation event (D_4) is described as a late northwest-southeast shortening event that resulted in a dextral strike-slip movement, Z-shaped folding, and northeast striking vertical foliation (Bedeaux et al., 2017). Regional metamorphism of sub-greenschist to amphibolite facies affected the supracrustal rocks of the Rouyn-Noranda area from 2677 to 2643 Ma (Powell et al., 1995).

The Abitibi subprovince is known for its exceptional economic importance due to its large gold camps hosted by the Cadillac-Larder Lake and the Destor Porcupine deformation zones and their splays (Fig. 1; Card, 1990; Dubé & Gosselin, 2007; Monecke et al., 2017). The CLLDZ is a first-order crustal-scale fault zone that

served as the main hydrothermal pathway toward the surface for deep-seated gold-bearing fluids (Robert et al., 1995; Daigneault et al., 2002; Beaudoin et al., 2006; Dubé & Gosselin, 2007; Bedeaux et al., 2017). Precipitation of gold from these fluids in veins or wall-rock replacement along the CLLDZ and higher-order faults resulted in the formation of orogenic gold deposits (Robert et al., 1995; Neumayr et al., 2000; Dubé & Gosselin, 2007), such as along the Augmitto-Bouzan segment. Most of the orogenic gold mineralization is considered to have been formed around ca. 2643 Ma (Herzog et al., 2022) and is synchronous to the main north-south shortening event (D_3) and post-peak metamorphism (Dubé & Mercier-Langevin, 2020). Reactivation of the CLLDZ has probably occurred during D_4, leading to another gold-related event (Dubé & Mercier-Langevin, 2020).

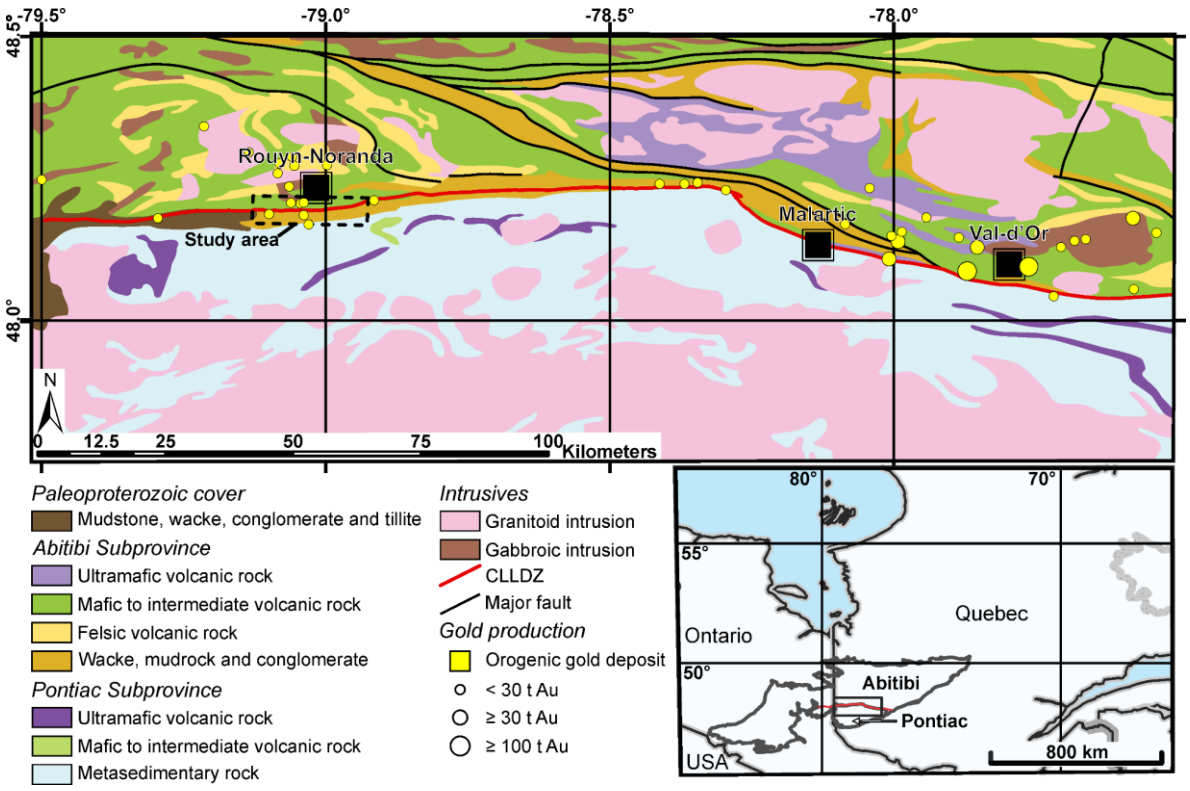

Figure 1 Simplified geological map of the southern Abitibi subprovince in Québec (Canada), showing the extent of the CLLDZ and highlighting the study area. The bottom right image shows the mapped area within the defined Abitibi and Pontiac subprovinces. Modified from Montsion et al. (2018). The gold production of orogenic gold deposits is taken from Dubé and Mercier-Langevin (2020).

1.4.2 Geology of the Augmitto-Bouzan segment

The study area covers a 12 km stretch of the CLLDZ south of Rouyn-Noranda and is subdivided into six blocks, from west to east: Augmitto, Cinderella, Lac Gamble, Astoria, East Bay, and Bouzan (Fig. 2). From north to south, the study area is underlain by volcanic rocks of the Blake River Group, followed by sedimentary rocks of the Timiskaming Group, volcanic rocks of the Piché Group, more Timiskaming rocks and metasedimentary rocks of the Pontiac Group (Fig 2). The 2704-2695 Ma Blake River Group (Corfu et al., 1989; Corfu, 1993; Mortensen, 1993; Ayer et al., 2002; Lafrance, 2005; David et al., 2006; Thurston et al., 2008;

McNicoll et al., 2014) is characterized by submarine andesitic and basaltic lavas with minor felsic occurrences that are intruded by synvolcanic gabbro-diorite sills (Ross et al., 2011; Salmon & McDonough, 2011). The contact between the northward-facing Blake River Group and the southward-facing Timiskaming Group is marked by an angular unconformity (Poulsen et al., 2017). The Timiskaming Group unconformably overlies the Blake River and Pontiac groups and is divided into two formations located on both sides of the CLLDZ (Dimroth et al., 1982; Salmon & McDonough, 2011). The Granada Formation is south of the fault and is composed of polymictic conglomerates, greywackes, and volcanosedimentary rocks (Dimroth et al., 1982; Salmon & McDonough, 2011). North of the CLLDZ, the sedimentary rocks of the La Bruère Formation have similar compositions as the Granada Formation but represent a more fluviatile environment (Dimroth et al., 1982; Salmon & McDonough, 2011). Fault-bounded on both sides by those two Formations is a < 100 m thick discontinuous band of mostly komatiitic-basaltic rocks of the Piché Group (>2708.8 Ma; Fig. 1, Fig. 2; Lafrance, 2015; Laporte, 2016; Poulsen et al., 2017; Bedeaux et al., 2018; David et al., 2018). These rocks have been highly altered and deformed to form serpentinite, talc, talc-carbonate, and chlorite schists, spatially associated with the CLLDZ and considered as its physical expression (Dimroth et al., 1982; Poulsen et al., 2017; Bedeaux et al., 2018). The Piché Group is interpreted as multiple slivers of volcanic rocks that have been inserted into the CLLDZ during the early stages of the Pontiac subprovince accretion, prior to the sedimentation of the Timiskaming Group (Bedeaux et al., 2018). Its exposure is masked to the west by the unconformably overlying Proterozoic Cobalt Group (Powell & Hodgson, 1992). Excluding the synvolcanic gabbro-diorite sills intruding the Blake River Group, the study area is cross-cut by two main types of intrusive rocks: Archean albitite dykes and the NE-SW Mesoproterozoic gabbro dykes of the Abitibi dyke warm (Fig. 2, Laporte, 2016). Greenschist-facies metamorphism affects the rocks of the area, with local exceptions around the Mesoproterozoic gabbro dykes where a 50 m wide contact metamorphic halo reaches the greenschist-amphibolite facies transition (Powell et al., 1995; Laporte, 2016).

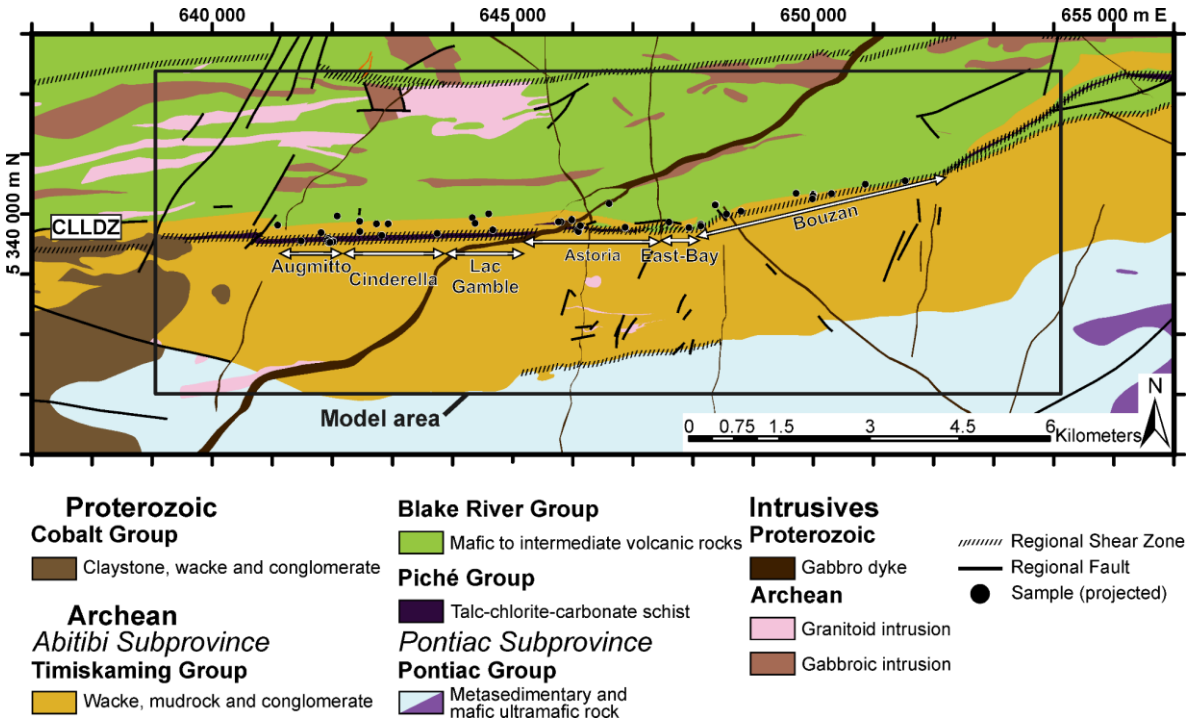

Figure 2 Geological map of the Augmitto-Bouzan segment area, Québec (Canada). The numerical model area is marked by the rectangle. Modified from (Ministère des Ressources Naturelles Géologie Québec, 2021). UTM coordinates in NAD83 zone 17N.

1.4.3 Gold mineralization

Most of the gold-bearing mineralization is located within the carbonatized and deformed ultramafic rocks of the Piché Group, but also at the southern Piché-Timiskaming contact and in albitite dykes (Gauthier et al., 1990; Salmon & McDonough, 2011; Laporte, 2016). Two main alteration assemblages are associated with the Piché Group rocks within the segment. The first assemblage is composed of talc-chlorite±calcite-ankerite resulting in rocks with a dark green to black color (Salmon & McDonough, 2011). They represent the least altered Piché Group rocks, where primary volcanic textures can be preserved (Salmon & McDonough, 2011). The second alteration assemblage consists of carbonate±fuchsite, giving the rocks a light tan to green color (Salmon & McDonough, 2011). The alteration assemblage is composed of more than 50 % carbonate minerals, such as magnesite and ankerite, with significant amounts of magnesian chlorite, fuchsite, and sericite and is associated with most of the gold mineralization of the area (Salmon & McDonough, 2011; Rafini, 2014; Laporte, 2016). A local tremolite-chlorite assemblage can be observed surrounding the Mesoproterozoic dykes of the Astoria block, representing late contact metamorphism of the Piché Group, accompanied by gold remobilization (Laporte, 2016). Gold mineralization is found either in selvages or within veins, veinlets, or stockworks of quartz-carbonate±tourmaline (Gauthier et al., 1990; Salmon & McDonough, 2011; Laporte, 2016). Gold mineralization is considered a continuous process that began at the end of the main deformation event (D_3) and lasted until the late Archean dextral strike-slip motion (D_4; Gauthier et al., 1990). Gold is in the quartz vein matrix or associated

with sulfides, as well as in solution in sulfides (Laporte, 2016). Ore minerals are native gold with associated pyrite, arsenopyrite, pyrrhotite, and chalcopyrite (Laporte, 2016). The most common sulfide is pyrite, whereas arsenopyrite dominates near contact with the Timiskaming rocks (Laporte, 2016).

Figure 3 displays the gold content from the carbonate±fuchsite zone of the Piché Group in a longitudinal vertical section. Laterally, there are important gold content variations between the western endowed sectors (Augmitto to Astoria) and the eastern less endowed sectors (East-Bay and Bouzan; Fig. 3). Mineralization forms shoots that are subvertical to steeply dipping to the east, with gold grades reaching over 25 g/t per meter (Fig. 3). The less endowed sectors are barren of gold, except for a single patch of mineralization with less than 5 g/t Au near the surface, at the limit between the East-Bay and Bouzan blocks (Fig. 3). Geological differences between both sectors include a change in the orientation of the Piché Group from E-W in the endowed sectors to NE-SW in the less endowed sectors, accompanied by a decrease in its thickness from around 100 to less than a few tens of meters (Fig. 2). The northern portion of the Timiskaming Group, the La Bruère Formation, also disappears towards the eastern blocks, where the Piché Group is in contact with the volcanic rocks of the Blake River Group (Fig. 2).

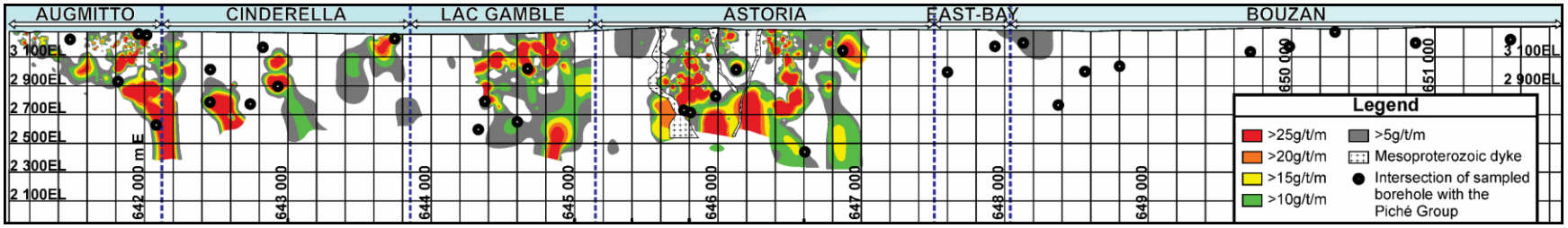

Figure 3 Longitudinal section in the Piché Group showing the distribution of gold along the Augmitto-Bouzan segment. Modified from Ressources Yorbeau Inc. unpub. data (2021). UTM coordinates are in NAD83, zone 17N.

1.5 Methodology

1.5.1 Sampling strategy

Representative vein and wall rock samples (n=108) from drill cores and outcrops were collected along a grid along the Augmitto-Bouzan segment, from surface to a maximum depth of 685 m, and in gold-rich to gold-poor areas to spatially constrain the variation in mineral and fluid compositions. From these, 28 thin sections of quartz-carbonate-tourmaline and quartz-carbonate veins were made to measure the major element composition of carbonate and tourmaline. A total of 33 host rock samples associated with the veins were collected from drill cores for major elements and isotope (O, C) whole-rock analysis. Thin sections of these samples were used to establish the modal proportions of the mineral phases. Samples include Piché Group altered volcanic rocks (n=23), Timiskaming Group greywackes (n=9), and an albitite dyke (n=1). From the Piché Group volcanic rocks, 19 samples are representative of the carbonate±fuchsite alteration, two of the talc-chlorite-carbonate alteration, and two of the tremolite-chlorite assemblage. The Timiskaming Group greywackes did not appear visibly altered. The host rock samples were selected to be free of veins, homogeneous, and representative of the area. A single outcrop sample of greywacke was taken approximately 600 m south of the CLLDZ as a representative of unaltered Timiskaming greywacke for oxygen isotope analysis. Near-surface oxidation and veinlets were removed from the samples before analysis. Gold grades are from company assays.

1.5.2 Analytical Methods

1.5.2.1 Stable Isotope Geochemistry

Vein quartz, tourmaline, and carbonate concentrates were handpicked under a binocular microscope. Between 7 and 10 mg of powdered sample, including host rocks, were used for each analysis. Oxygen was extracted following Clayton and Mayeda (1963) at the Stable Isotope Laboratory, Université Laval, Québec, Canada. The liberated O_2 was passed over a hot graphite rod to be converted to CO_2. The isotopic composition of the evolved CO_2 was measured by a Micromass Isoprime Isotope Ratio Mass Spectrometer at the Geotop-UQAM, Montreal, Canada. Oxygen isotope ratios are reported in the δ notation in ‰ relative to V-SMOW with a precision of 0.2 ‰. The precision and accuracy of the $\delta^{18}O$ values were verified by repeated analyses of NBS28 (9.6 ± 0.2 ‰) and K-1 (19.2 ± 0.2 ‰) internal quartz standard.

The tourmaline hydrogen isotope composition and the carbon and oxygen compositions of carbonate phases from host rocks and veins were measured at the Queen's University Facility for Isotopic Research, Kingston, Canada. For carbonate phases, 20 mg of material was needed for whole-rocks and 1 mg for pure concentrates, which were then reacted with anhydrous phosphoric acid for 4 hours at 72 °C. The released CO_2 was then analysed using a Thermo-Finnigan Gas Bench coupled to a Thermo-Finnigan Delta^{plus} XP Continuous-Flow Isotope Ratio Mass spectrometer. Oxygen and carbon isotopes are reported in the δ notation relative to V-

SMOW and V-PDB, respectively, both with precisions of 0.2 ‰. Since the analyses were calibrated according to a calcite standard, a correction of –1.2 ‰ was added to the $\delta^{18}O$ values of dolomitic vein samples based on the carbonate-HPO_3 fractionation from Rosenbaum and Sheppard (1986) and Sharma et al. (2002) at 72 °C. Tourmaline samples were degassed for one hour at 100 °C into silver capsules. The δD values were measured using a Thermo-Finnigan thermo-combustion elemental analyzer coupled to a Thermo-Finnigan Continuous-Flow Isotope Ratio Mass Spectrometer. Hydrogen isotope ratios are reported in the δ notation relative to V-SMOW with a precision of 3 ‰.

1.5.2.2 Mineral chemistry

Major elements in tourmaline and carbonates were measured at the *Laboratoire de microanalyse* of Université Laval, Québec, Canada, with a CAMECA SX-100 electron probe microanalyzer. Tourmaline was analysed for the following elements (Fe, Cr, Ca, Na, Mg, Si, Al, Mn, Ti, and K) using a 15 keV voltage, 20 nA current, and a beam size of 5 µm. Major elements in carbonate (Fe, Ca, Mg, Mn and Sr) were analysed using a 15 keV voltage, 20 nA current, and a beam size of 10 µm. Tourmaline data was normalized to 29 oxygens, according to Henry et al. (2011).

1.5.2.3. Lithogeochemistry

Whole-rock lithogeochemistry was carried out at ALS laboratories, Vancouver, Canada. Samples were subjected to the fused beads technique, followed by acid digestion to be then analysed for the following elements (Si, Al, Ca, Mg, Na, K, Ti, Fe, Mn, P, Cr, Sr, and Ba) using an Inductively Coupled Plasma-Atomic Emission Spectrometer. Water of crystallization has been analysed by placing the samples in a combustion furnace, to then be measured by infrared spectrometry. Concentrations of CO_2 have been measured by a CO_2 coulometer after digestion of the samples by $HClO_4$. Total C and S contents were measured by combustion of the samples in a Leco furnace. Results under the detection limits correspond to 6 % of the data and have been replaced by the value of the detection limit divided by the square root of two, according to Croghan and Egeghy (2003).

1.5.3 Modelling of fluid flow

The model used in this work is a modified version of HydroGeoSphere (HGS), a three-dimensional variably saturated flow and solute transport model developed by Therrien and Sudicky (1996) and adapted by Beaudoin et al. (2006) to simulate fluid flow as well as oxygen isotope transport and reaction in fractured geological materials. The model uses a control volume finite element technique discretized in 3D, which guarantees local and global mass conservation (Therrien & Sudicky, 1996; Beaudoin et al., 2006). HGS simulates flow following Darcy's law, as well as advective-dispersive isotope mass transport, coupled with isotopic exchange between the rock matrices and fluid along with temperature-dependent fluid-rock

fractionation. The governing equations and verifications of the model are detailed in Therrien and Sudicky (1996) and Beaudoin et al. (2006).

1.6 Results

1.6.1 Vein paragenetic sequence

The paragenetic sequence of the veins has been established based on cross-cutting relationships and is presented in Figure 4, where only the most common types of veins are displayed. The first generation of veins (V_1) consists of folded and crenulated veins and veinlets filled by carbonates (Fig. 5A-B). They are ubiquitous throughout the whole segment but only found within the Piché Group rocks, regardless of the alteration assemblage. The second generation of veins (V_2) is composed of folded, crenulated, and occasionally boudinaged veinlets of grey quartz (Fig. 5B), usually associated with V_1. They crosscut the V_1 generation but are not as abundant (Fig. 5B). They are hosted mainly by carbonate±fuchsite alteration in the Piché Group. Both of these types of veins can be found parallel to the main deformation fabric (Fig. 5A) and are often deformed, showing that they were most likely pre to syn D_3. The third generation of veins (V_3; Fig. 5C) is only found in the Augmitto, Cinderella, and Lac Gamble blocks and is preferentially hosted by strong fuchsitic alteration in the Piché Group. V_3 veins are folded, centimeter-size, and composed of beige microcrystalline quartz, commonly with sulfide mineralization. The fourth generation (V_4; Fig. 5D) crosscuts V_3 and consists of white-grey quartz with varying content of carbonate and tourmaline, with minor sulfide mineralization. They form centimeter to meter-size tabular stockworks and hydrothermal breccias containing clasts of the surrounding wall rocks (Fig. 5D). They are almost exclusively hosted by Piché Group altered volcanic rocks and Archean albitite dykes, with rare occurrences in Timiskaming greywacke and Blake River andesite near the CLLDZ. When hosted in the Piché Group volcanic rocks, V_4 veins are generally found in association with strong carbonate±fuchsite alteration. The fifth generation (V_5) forms decimetric to pluridecimetric veins of white to dark-grey quartz, with varying amounts of carbonate and occasionally sulfide (Fig. 5E), hosted within both Timiskaming sedimentary rocks and Piché Group volcanic rocks. The sixth generation (V_6; Fig. 5F) is characterized by centimeter-wide veins of subhedral to euhedral dolomite or ankerite, with minor quartz. The seventh and final generation (V_7) represents straight, planar, and late white calcite veinlets (Fig. 5G), cross-cutting every previous generation.

The gold is associated with V_3 to V_5. Samples analysed throughout this study were selected based on these three gold-related vein generations. Due to their similarity in mineralogy, timing, and relationship with gold endowment, these three vein generations were treated as a unit, without distinction between generations.

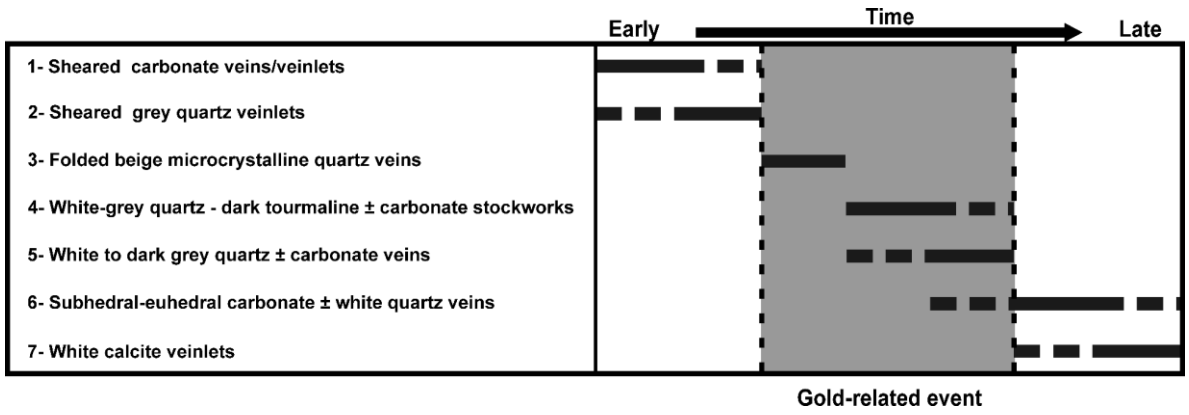

Figure 4 Simplified paragenetic sequence based on cross-cutting relationships of the different vein types. The greyed-out field corresponds to the time period related to gold mineralization.

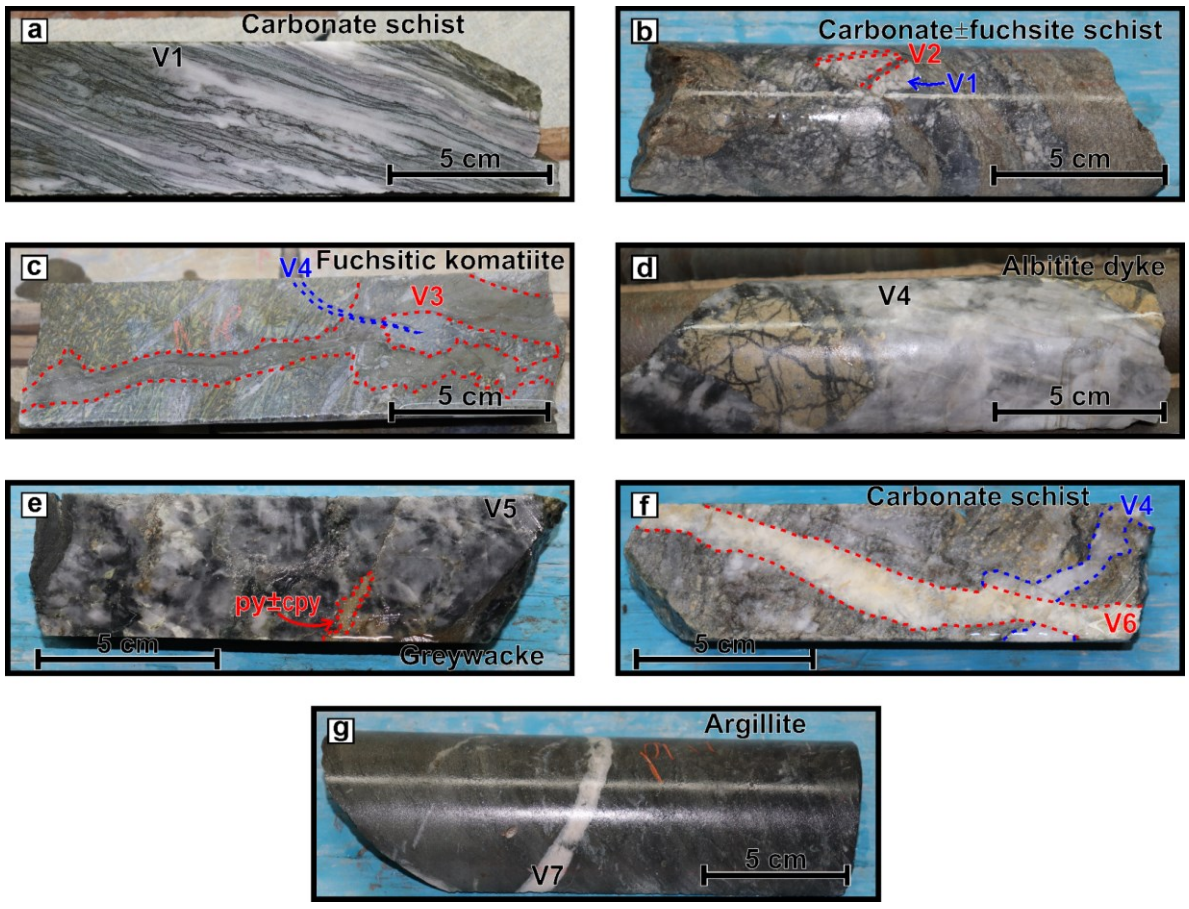

Figure 5 a V_1 parallel to the main foliation in a carbonate schist host rock of the Piché Group. **b** V_2 filled by dark grey quartz in carbonate±fuchsite rocks of the Piché Group. The quartz of V_2 seems to have simultaneously grown with the carbonate of V_1 in some areas of the core but cross-cuts it in others (*red*). **c** V_3 (*red*) in a strongly fuchsite altered rock of the Piché Group with preserved spinifex texture. It is crosscut by a small V_4 veinlet (*blue*). **d** V_4 with drusy tourmaline cutting an albitite clast. **e** V_5 in greywacke of the Timiskaming Group cut by a pyrite (py) ± chalcopyrite (cpy) stringer in dark grey quartz. **f** V_6 (*red*) in a carbonate schist of the Piché Group, cross-cutting a V_4 vein (*blue*). **g** Typical late V_7 in Timiskaming Group argillite.

1.6.2 Whole-rock chemical composition

Whole-rock major element lithogeochemical data can be found in Appendix B. The carbonate±fuchsite and talc-chlorite-carbonate schist samples (n=20) range in composition from 29.9 to 56.5 wt% SiO_2 ($\bar{x} \pm 1\sigma$ = 37.1 ± 7.3), 4.1 to 11.8 wt% Al_2O_3 (5.5 ± 1.9), 6.1 to 25.8 wt% MgO (17.1 ± 6.3), 3.7 to 11.1 wt% Fe_2O_3 (8.5 ± 1.8), 0.12 to 0.51 wt% Cr_2O_3 (0.29 ± 0.08) and 1.2 to 16.7 wt% CaO (7.7 ± 4.7). The two tremolite-chlorite schists from Astoria were sampled in the CLLDZ, next to the Proterozoic gabbro dykes, and are metamorphosed equivalents of the carbonate±fuchsite and talc-chlorite-carbonate schists. Their major element compositions are similar with 40.8 to 45.1 wt% SiO_2, 5.9 to 9.5 wt% Al_2O_3, 24.9 wt% MgO, 11.2 to 12.8 wt% Fe_2O_3, 0.18 to 0.39 wt% Cr_2O_3, and 4.83 to 5.97 wt% CaO. Most of these rocks fall into the komatiite to komatiitic basalt fields, with the exceptions of a Lac Gamble and an East-Bay block sample that plot into the high-Mg and high-Fe basalts, respectively (Fig. 6A). This shows a relatively homogeneous chemical composition of the Piché Group throughout the segment. The choice of the Jensen cation plot (Fig. 6A; Jensen, 1976) is based on the low susceptibility of its elements to chemical mobility during deuteric and metamorphic processes and the fact that they vary in inverse proportions to one another. This ternary diagram has also been used for similar rock types, alteration patterns, and geological environments (e.g., Robert et al., 1990; Lafrance, 2015). The geochemical classification also correlates with geochemical and field observations of the same rocks from other studies (e.g., Gauthier et al., 1990; Laporte, 2016; Bedeaux et al., 2017; Bedeaux et al., 2018).

To measure the intensity of the alteration, we used molar fractions of elements following Kishida and Kerrich (1987) due to similarities with the Kerr Addison deposit in terms of host rocks and alteration types. The molar ratio CO_2/(Fe+Mg+Ca) indicates the degree of carbonatization, which is often linked to gold mineralization. A ratio close to 0 would indicate an unaltered host rock, and a ratio near 1 indicates the saturation value of carbonate minerals of the host rock (Kishida & Kerrich, 1987). The muscovite molar ratio has been adapted for fuchsite since it is often found in close association with gold across the property and the fact that Cr replaces a portion of Al in fuchsite (Whitmore et al., 1946). The resulting index is 3K/(Al+Cr), where a ratio of 1 corresponds to the saturation relative to muscovite/fuchsite of the host rock. The saturation indices were not calculated for the two tremolite-chlorite samples since they do not represent the hydrothermal alteration assemblage.

Spatially, the carbonatization ratios are relatively constant within the Piché Group throughout the segment, with values averaging 0.7 (Fig. 7A-B). A first peak of values is found between longitudinal positions of 1000 and 1760 m in the Augmitto and Cinderella blocks, where the CO_2/(Fe+Mg+Ca) average is 0.8 with a maximum of 0.99 at a depth of 250 m. Another high carbonatization zone with a molar ratio of 0.96 is located at a depth of 700 m, around a longitudinal position of 3275 m. The westernmost sample, near the surface, has a low CO_2/(Fe+Mg+Ca) value of 0.3 (Fig. 7A-B). The lowest ratio is at a position of 7500 m and a depth of 370 m in the Bouzan block, where the values drop to 0.05. These two low-value samples are from the talc-chlorite-

carbonate alteration zone. The 3K/(Al+Cr) ratio shows that the muscovite-fuchsite alteration is not pervasive throughout the segment, with peaks of higher intensity in certain areas (Fig. 7C-D). The peak in the Lac Gamble block is at a longitudinal distance of 3270 m and a depth of 700 m with a value of 0.89 (Fig. 7C-D). The fuchsite index drops to near zero at similar depths and 275 m away towards the east. However, for the same distance and a depth of 285 m, the 3K/(Al+Cr) value is 0.47 (Fig. 7C-D). From the Astoria to the Bouzan blocks, the index is near zero, except for a single East-Bay sample at 0.26 (Fig. 7C-D).

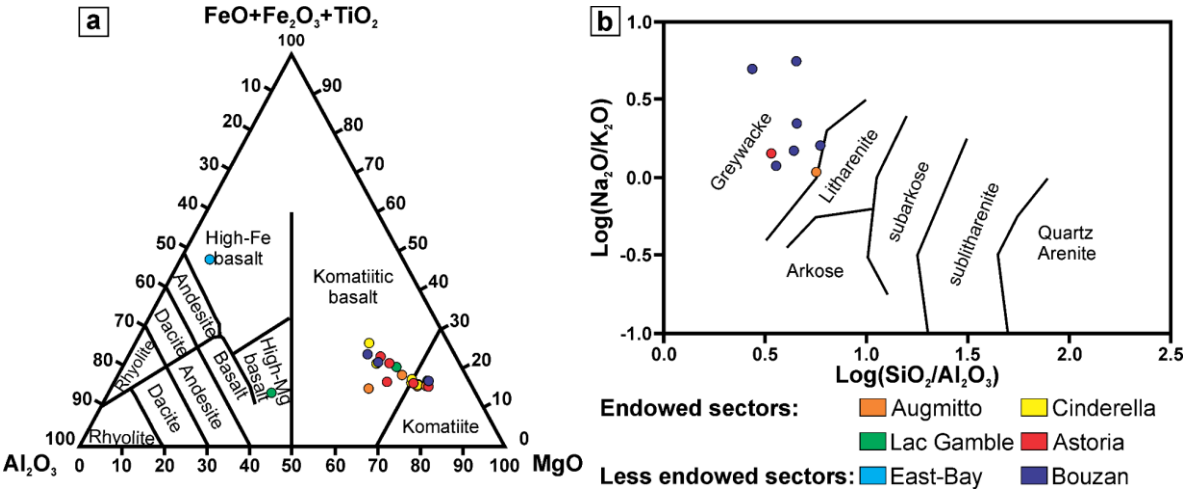

Figure 6 a Geochemical classification of the Piché Group volcanic rocks from the Augmitto-Bouzan segment, based on the cation plot ternary diagram of Jensen (1976). **b** Geochemical classification of the Timiskaming Group sedimentary rocks from the Augmitto-Bouzan segment, based on the Log(SiO_2/Al_2O_3) vs. Log(Na_2O/K_2O) diagram of Pettijohn et al. (1973).

Major element composition of greywacke samples (n=8) ranges from 51.0 to 71.8 wt% SiO_2 (60.7 ± 8.2), 11.7 to 19.3 wt% Al_2O_3 (14.5 ± 2.6), 2.8 to 14.2 wt% Fe_2O_3 (6.4 ± 3.8), 1.0 to 8.2 wt% CaO (3.6 ± 2.6), 0.5 to 2.5 wt% K_2O (1.7 ± 0.7) and 2.2 to 5.0 wt% Na_2O (3.3 ± 0.9). Every sample plots into the greywacke field of Pettijohn et al. (1973; Fig. 6B).

The albitite dyke sample from East-Bay contains 48.9 wt% SiO_2 and high values of Al_2O_3, Na_2O, TiO_2, and P_2O_5 of 17.2, 5.2, 1.1, and 0.33 wt%, respectively. According to geochemical classification diagrams (Cox et al., 1979; Middlemost, 1994; Enrique & Esteve, 2019), the dyke had a gabbroic composition prior to its albitization.

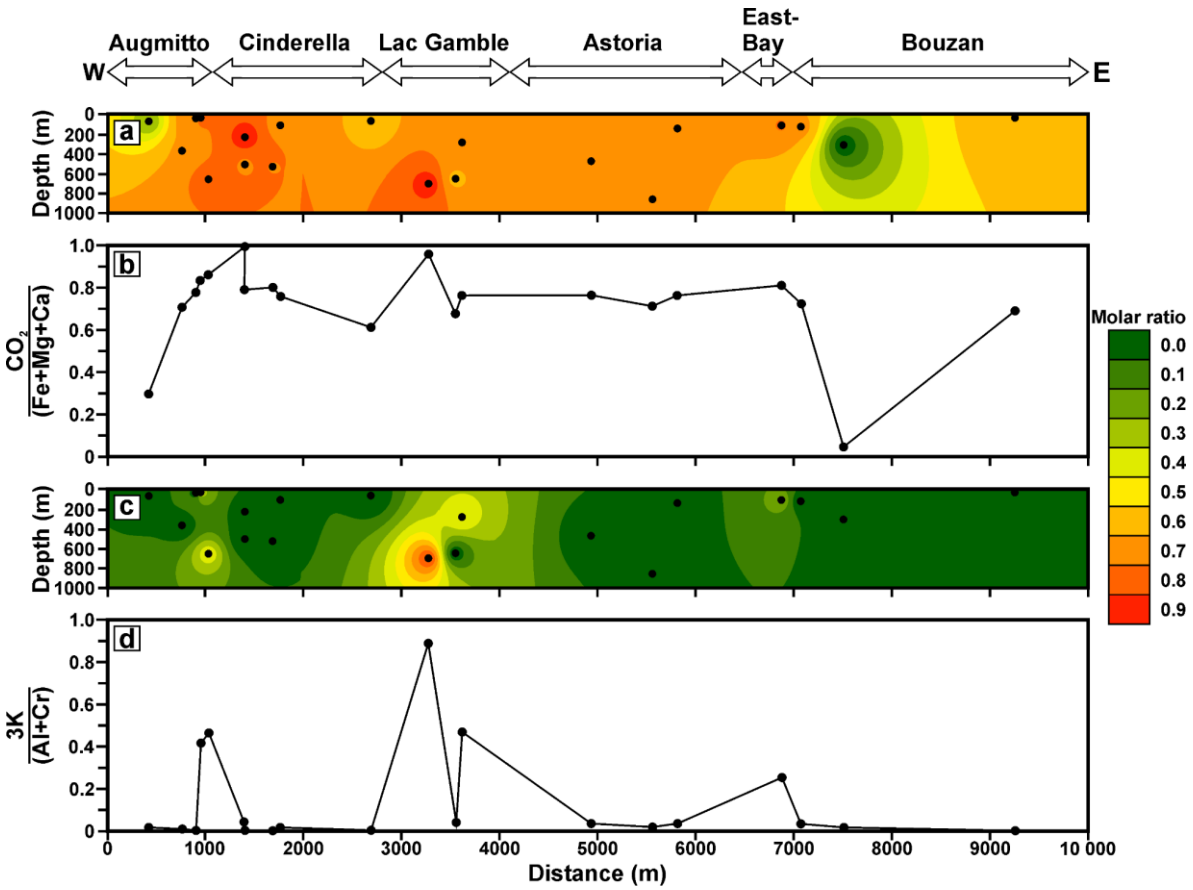

Figure 7 Molar ratios of elements adapted from Kishida and Kerrich (1987), related to the main alteration minerals associated with gold mineralization in the Piché Group rocks. **a** Spatial variation of the CO_2/(Fe+Mg+Ca) carbonatization index across the segment **b** CO_2/(Fe+Mg+Ca) saturation values versus the longitudinal distance (m). **c** Interpolation of the 3K/(Al+Cr) alteration index for saturation relative to fuchsite across the property. **d** 3K/(Al+Cr) values versus longitudinal distance. Interpolations from **a** and **c** were carried out with the IDW method described in Appendix A.

1.6.3 Vein carbonate and tourmaline chemical composition

The main carbonate mineral in the V_4 and V_5 veins from the Augmitto, Cinderella, Lac Gamble, Astoria, and East-Bay blocks is ferroan dolomite (Appendix C; Fig. 8). Some rare occurrences of ferroan magnesite are found in V_4 veins of the Augmitto and Cinderella blocks (Fig. 8). Calcite is found in one sample from Astoria, which becomes the dominant carbonate phase towards the Bouzan block, although some rare ankerite is found in the latter (Fig. 8). A decrease of the Mg/(Mg/Fe) ratio, from dolomitic to ankeritic carbonate, is documented from the gold-endowed western area (n=23, 0.84 ± 0.03) to the less endowed eastern area (n=14, 0.71 ± 0.14; Fig. 10A). The Mn content follows the same trend as the Fe content (Fig. 10B), from an average of 0.23 % $MnCO_3$ in endowed sectors to an average of 0.68 wt% in the less endowed areas. Only one sample from Bouzan has a similar chemical composition typical of ferroan dolomite as the endowed sectors, which is from the only sampled borehole cutting gold-bearing mineralization in the Bouzan block.

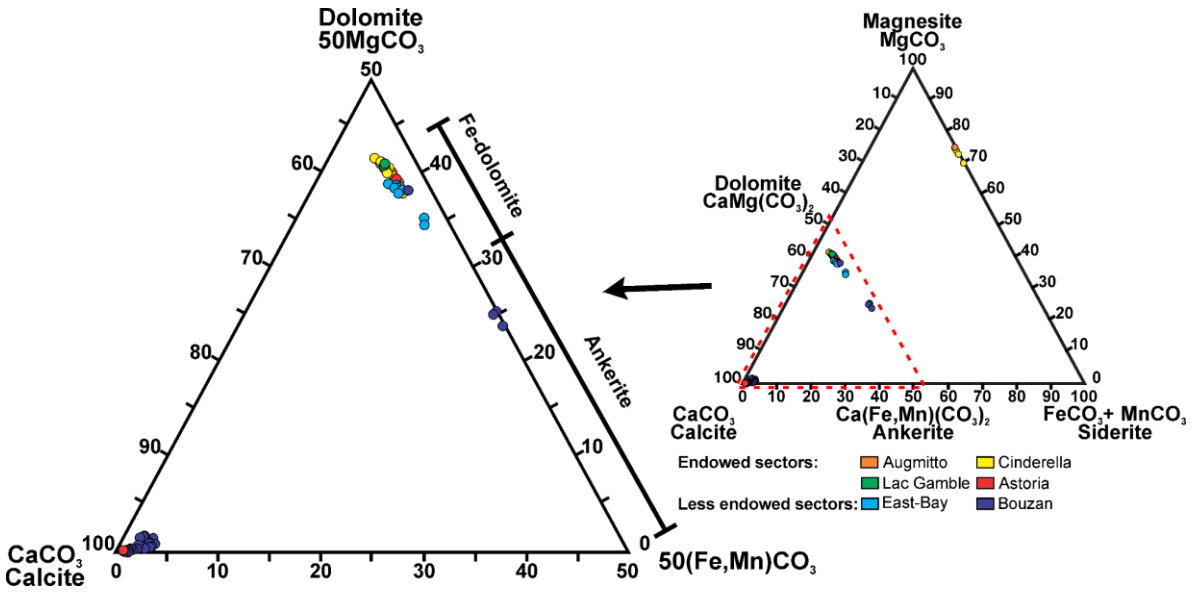

Figure 8 Composition of vein carbonates from the Augmitto-Bouzan segment, according to their respective blocks. $CaCO_3$-$MgCO_3$-$FeCO_3$ ternary diagram in mole%. The left diagram is zoomed-in at $50MgCO_3$ and $50(Fe,Mn)CO_3$. Analytical results are presented in Appendix C.

Vein tourmaline plots into the alkali group, except for two samples within the X-vacant group, with a dravitic composition (Fig. 9; Appendix D). Tourmaline from endowed sectors is characterized by Mg/(Mg+Fe) values between 0.8 and 0.89 (0.85 ± 0.02), Na/(Na+Ca) ratios between 0.92 and 0.99 (0.97 ± 0.02), as well as $^{x}\square/(^{x}\square+Na^{1+}+K^{1+})$ values from 0.09 to 0.33 (0.18 ± 0.07), and plot into the dravitic field (Fig. 9B-C). Tourmaline from less endowed sectors shows a wider range of Mg/(Mg+Fe), Na/(Na+Ca), and $^{x}\square/(^{x}\square+Na^{1+}+K^{1+})$ ratios ranging from 0.48 to 0.83 (0.64 ± 0.08), 0.56 to 0.98 (0.87 ± 0.11), and 0.09 to 0.52 (0.27 ± 0.15), respectively. In the less gold-endowed sectors, dravitic tourmaline has a higher Fe content, plotting towards the field for schorlitic tourmaline. Two tourmalines fall into the magnesio-foitic field, close to a dravitic composition (Fig. 9B). Endowed sectors tourmaline is Cr_2O_3-rich with lesser CaO and MnO contents than less endowed East-Bay and Bouzan blocks tourmaline. Overall, the tourmaline chemical composition follows the same trend as the dolomite-ankerite vein carbonate, with an increase in Fe, Ca, and Mn content, as well as a decrease in Mg from gold-endowed to less endowed sectors (Fig. 10A). Similar to carbonate, only one sample from Bouzan has a chemical signature similar to that of the endowed sectors' dravite. It is also associated with the only sampled borehole cutting gold mineralization of that sector.

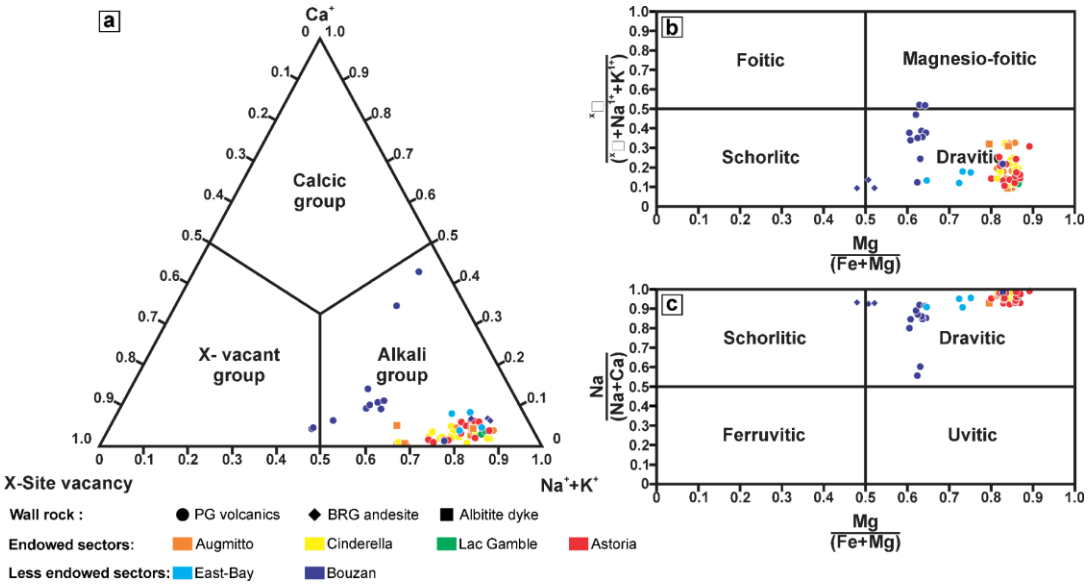

Figure 9 Composition of vein tourmaline from the Augmitto-Bouzan segment, according to their respective blocks and type of wall rocks.. **a** $^{X}\square$-Ca-(Na+K) ternary diagram for the primary tourmaline groups, adapted from Henry et al. (2011). **b** Mg/(Fe+Mg) versus $^{X}\square$/($^{X}\square$+Na^{1+}+K^{1+}) diagram to discriminate tourmaline species, modified from Henry et al. (2011). **c** Mg/(Fe+Mg) versus Na/(Na+Ca) diagram to discriminate tourmaline species, adapted from Jiang et al. (2002). PG = Piché Group. BRG = Blake River Group

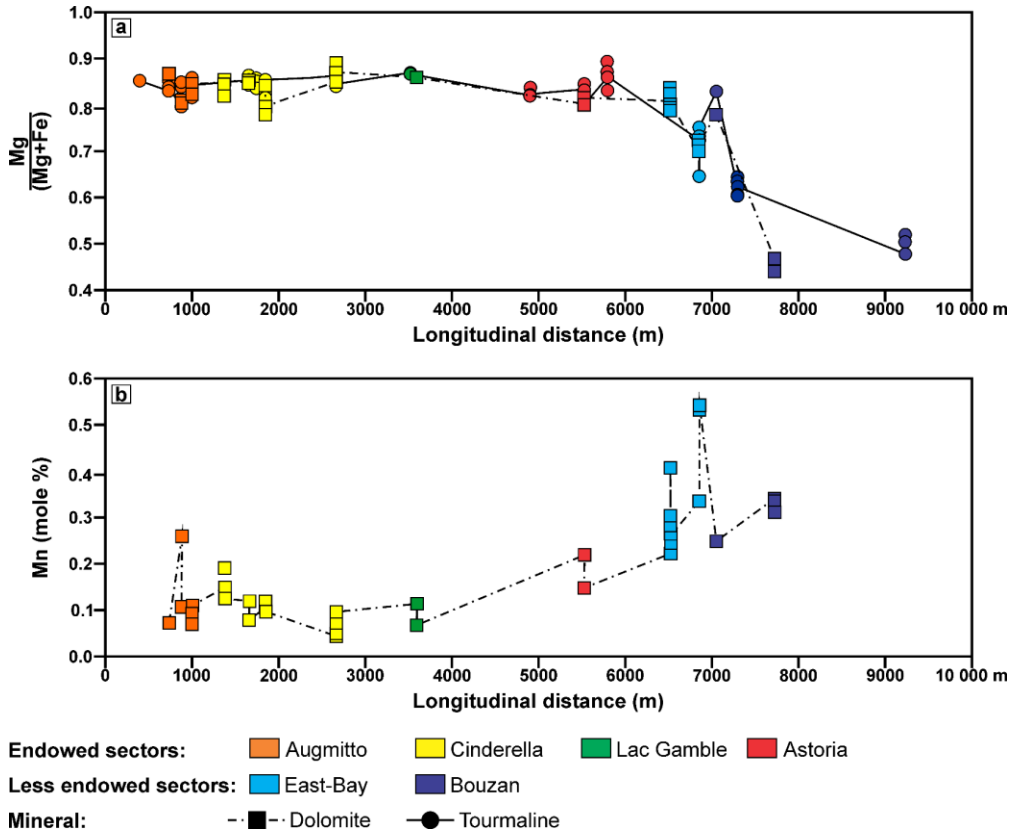

Figure 10 Changes in the chemical composition of vein minerals across the segment (Appendix C-D). **a** Mg/(Fe+Mg) values of vein tourmaline and dolomite-ankerite versus the longitudinal distance along the segment. **b** Mn content of dolomitic to ankeritic carbonates versus the longitudinal distance along the segment.

1.6.4 Host rock carbon and oxygen isotope composition

The host rock isotope compositions are presented in Appendix B. The 19 carbonate±fuchsite, two talc-chlorite-carbonate, and two tremolite-chlorite schists of the Piché Group have $\delta^{18}O$ values from 7.3 to 11.7 ‰ (9.5 ± 1.2; Fig. 11A). The dataset is relatively homogeneous and constant spatially, except for lower values in the Astoria block. The $\delta^{13}C$ and $\delta^{18}O$ values of the host rock undifferentiated carbonate fraction range from –6.0 to –2.1 ‰ (–4.1 ± 0.9; Fig. 11B) and 10.2 to 15.4 ‰ (13.1 ± 1.2; Fig. 11C), respectively. From both of these isotopic systems, the composition of the undifferentiated carbonate phases within the host rocks has a low compositional variance.

The nine greywacke samples of the Timiskaming Group have $\delta^{18}O$ values that range from 9.7 to 13.5 ‰ (11.4 ± 1.3; Fig. 11D). Their oxygen isotope composition is relatively constant throughout the segment. The $\delta^{13}C$ and $\delta^{18}O$ values from the undifferentiated carbonates of the greywacke range from –6.8 to –2.2 ‰ (–4.7 ± 1.6; Fig. 11F) and 12.1 to 15.5 ‰ (13.5 ± 1.1; Fig. 11E), respectively. The $\delta^{18}O$ composition of the carbonate fraction within the greywackes displays no systematic trends throughout the segment and is similar to the composition of the carbonate fraction in carbonate±fuchsite and talc-chlorite-carbonate schists.

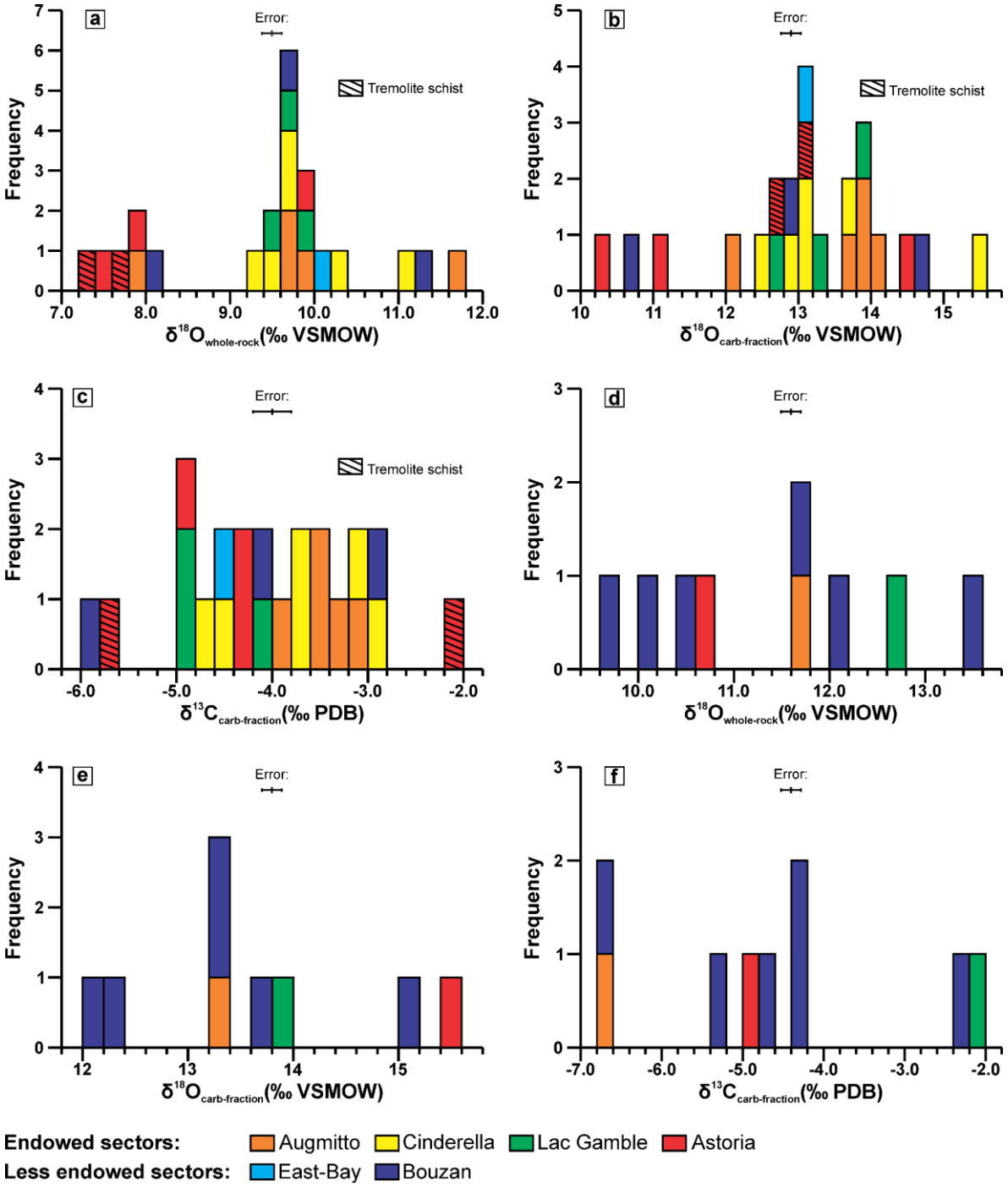

Figure 11 Isotopic composition of host rocks throughout the segment. **a** Histogram of the $\delta^{18}O$ values of the Piché Group rocks for each block of the segment. **b** Histogram of the $\delta^{18}O$ values of carbonate fraction from the Piché Group rocks for each block of the segment. **c** Histogram of the $\delta^{13}C$ values of carbonate fraction from the Piché Group rocks for each block of the segment. **d** Histogram of the $\delta^{18}O$ values of the Timiskaming greywackes for each block of the segment. **e** Histogram of the $\delta^{18}O$ values of carbonate fraction from the Timiskaming greywackes for each block of the segment. **f** Histogram of the $\delta^{13}C$ values of carbonate fraction from the Timiskaming greywackes for each block of the segment.

The albitite dyke sample from the East-Bay block has a $\delta^{18}O$ value of 6.5 ‰, which is the lowest of all host rocks across the segment. The undifferentiated carbonate in the albitite dyke has $\delta^{18}O$ and $\delta^{13}C$ values of 11.4 and –4.3 ‰, respectively.

1.6.5 Vein carbonate carbon and oxygen isotope composition

Carbonates from V_4 and V_5 range from a $\delta^{18}O$ of 11.3 to 15.0 ‰ (12.8 ± 1.0; Fig. 12A-C) and a $\delta^{13}C$ of –6.2 to –0.5 ‰ (–3.8 ± 1.6; Fig. 12 B-D) across the segment (n=20; Table 1). The isotopic composition of ferroan dolomite (n=11) ranges from a $\delta^{18}O$ of 11.5 to 14.5 ‰ (12.6 ± 0.9) and a $\delta^{13}C$ of –6.2 to –2.8 ‰ (–4.3 ± 1.1). One ferroan dolomite outlier from Astoria has a $\delta^{18}O$ of 21.9 ‰ and a $\delta^{13}C$ of –0.5 ‰ (Fig. 12). Calcite (n=8) has a $\delta^{18}O$ of 11.3 to 15.0 ‰ (13.1 ± 1.1) and a $\delta^{13}C$ of –5.3 to –0.5 ‰ (–2.9 ± 1.9).

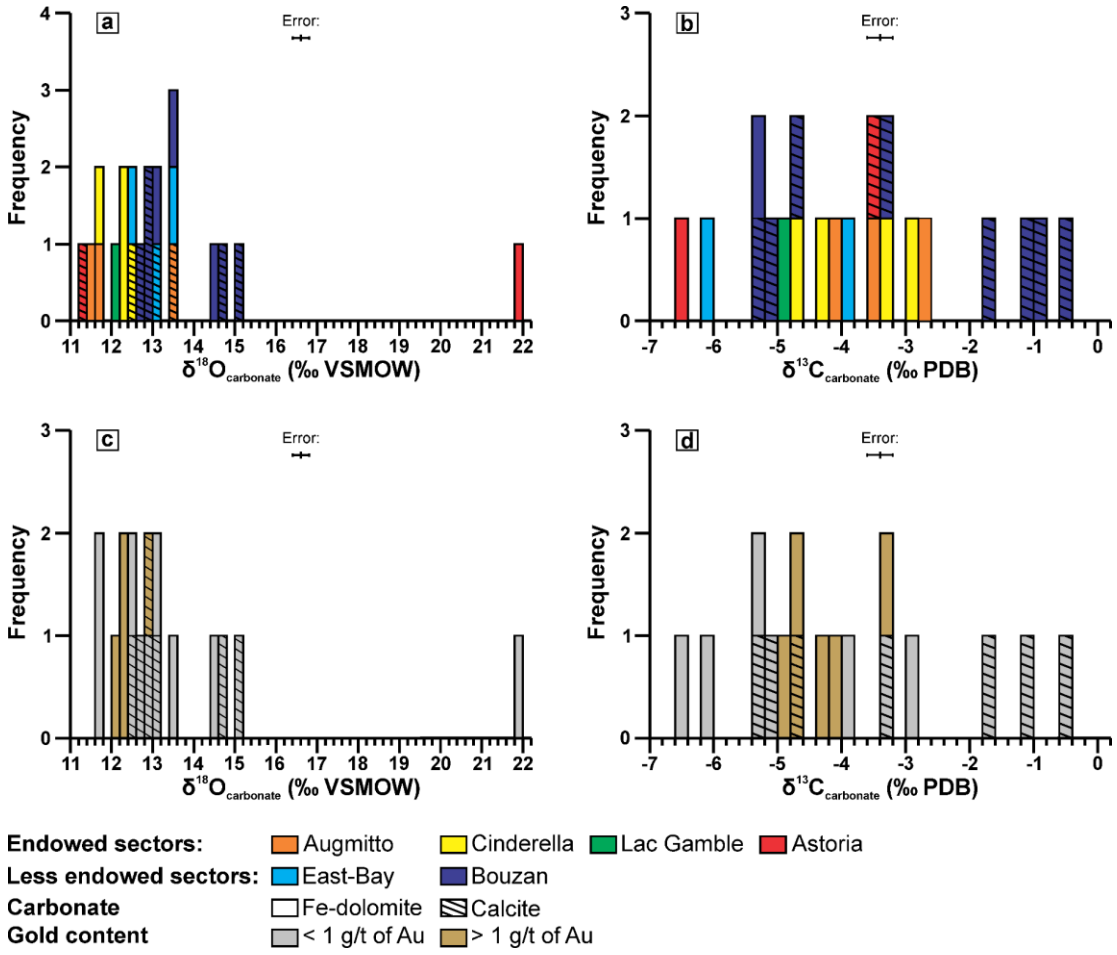

Figure 12 Isotopic composition of vein carbonates from the Augmitto-Bouzan segment, according to their respective block and gold content (Table 1). **a** $\delta^{18}O$ composition histogram for each block of the segment. **b** $\delta^{13}C$ composition histogram for each block of the segment **c** $\delta^{18}O$ composition histogram based on veins with more and less than 1 g/t of gold. **d** $\delta^{13}C$ composition histogram based on veins with more and less than 1 g/t of gold. Only veins with available analyses of their gold content are displayed in **c** and **d**.

Spatially, carbonates from the Augmitto to Astoria blocks (n=9) are characterized by $\delta^{18}O$ values between 11.3 and 13.5 ‰ (12.1 ± 0.7) and $\delta^{13}C$ values between –5.0 and –2.8 ‰ (–3.9 ± 1.4). Carbonates from the East-Bay and Bouzan blocks (n=9) have higher $\delta^{18}O$ but similar $\delta^{13}C$ values ranging from 12.4 to 15.0 (13.4 ± 0.9) and –6.2 to –0.5 ‰ (–3.5 ± 2.1), respectively. Thus, the carbonate phases from endowed sectors (Fig. 3) show relatively lower $\delta^{18}O$ and a narrower range of $\delta^{13}C$ values than those from the less endowed sectors (Fig. 3; Fig. 12A-B). Veins with more than 1 g/t of gold contain carbonate phases with lower $\delta^{18}O$ values, in contrast to veins with less than 1 g/t that have higher $\delta^{18}O$ values (Fig. 12C). Carbonates in veins with less than 1 g/t of gold also display a broader range of $\delta^{13}C$ values than veins with more than 1 g/t (Fig. 12D). Overall, the isotopic composition of the carbonate fraction from host rocks and vein minerals share a similar composition throughout the segment (Fig. 13).

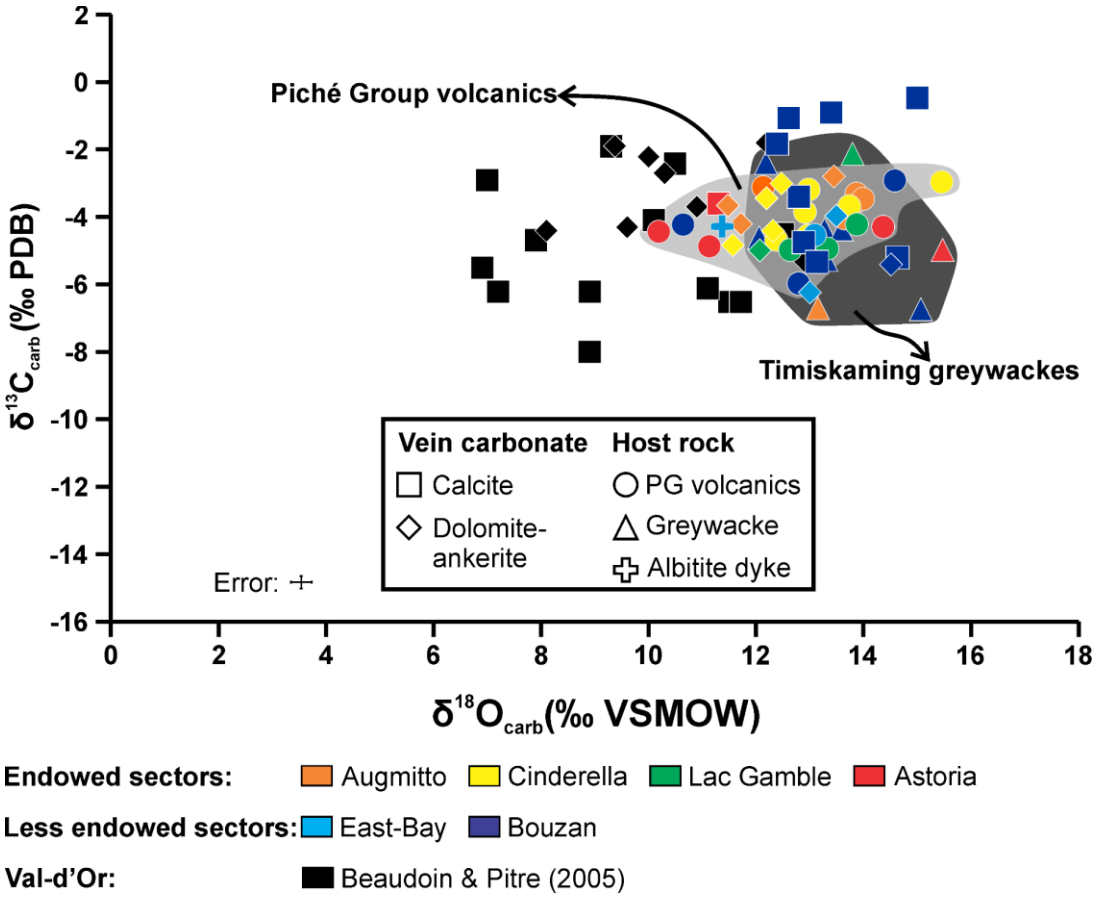

Figure 13 $\delta^{18}O$ versus $\delta^{13}C$ diagram for carbonate phases of the Augmitto-Bouzan segment, in veins (Table1) and host rocks (Appendix B). Carbonate data from the Val-d'Or vein field (Beaudoin & Pitre, 2005) are also plotted. PG = Piché Group.

1.6.6 Vein tourmaline (O, H) and quartz (O) isotope composition

The quartz $\delta^{18}O$ signature across the segment ranges from 11.8 to 16.8 ‰ (14.3 ± 0.9), following a normal distribution (Fig. 14A). The $\delta^{18}O$ values do not show a spatial variation between blocks (Fig. 14A) nor a

specific association with gold mineralization (Fig. 14D). Additionally, no noticeable $\delta^{18}O$ variations are found between V_3, V_4, and V_5 vein generations associated with gold.

Tourmaline (n=17) has $\delta^{18}O$ values between 8.5 and 11.9 ‰ (10.7 ± 0.9; Fig. 14B) and δD values between –59 and –18 ‰ (–39.7 ± 11.9; Fig. 14C). No notable spatial variation of both $\delta^{18}O$ and δD from tourmaline is found between blocks (Fig. 14B-C). Similar to the oxygen isotope composition of quartz, no specific tourmaline isotopic signature is correlated with the gold content of the veins (Fig. 14E-F).

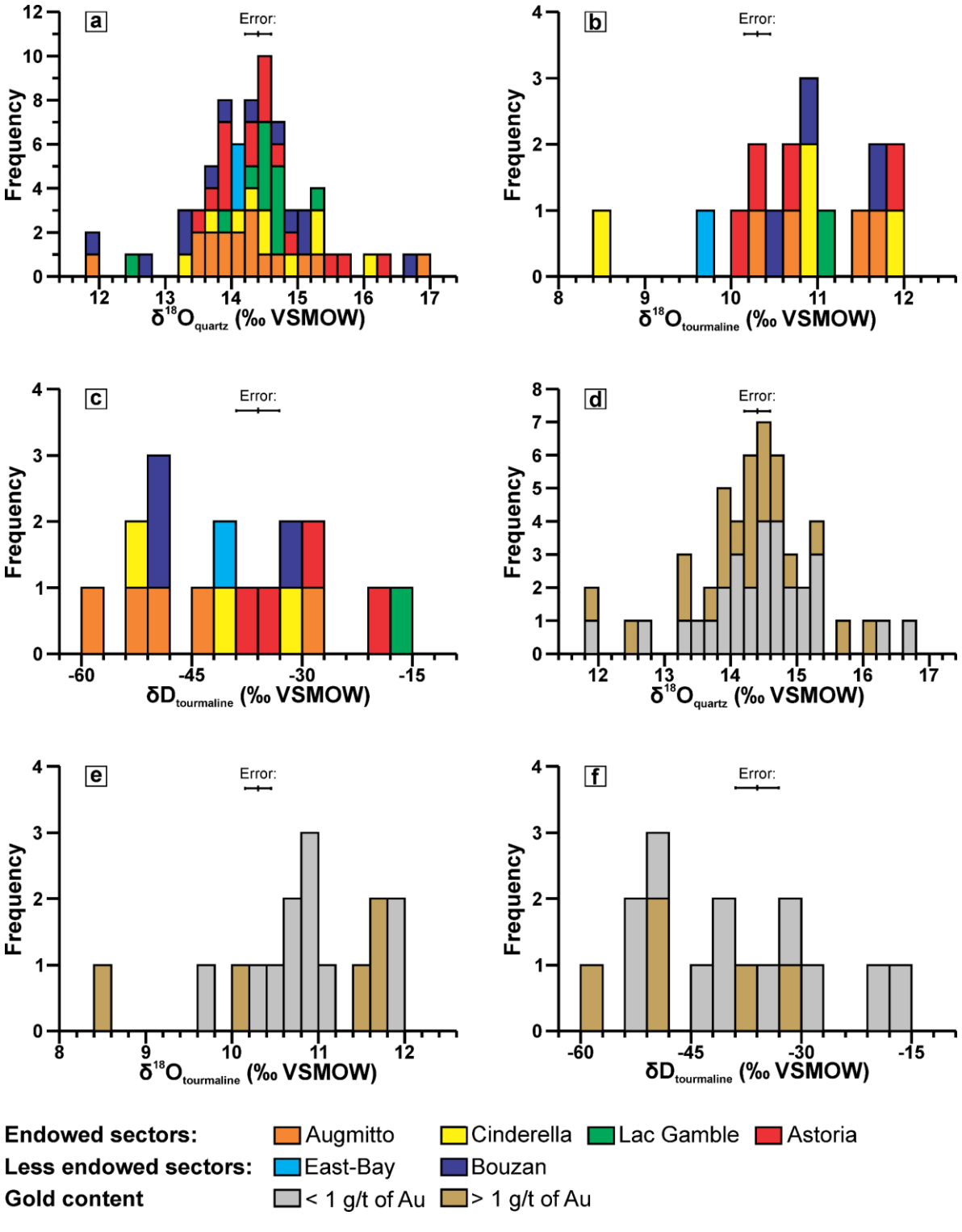

Figure 14 Isotopic composition of vein quartz and tourmaline from the Augmitto-Bouzan segment, based on their respective block and gold content. **a** Histogram of $\delta^{18}O$ values of quartz for each block. **b** Histogram of $\delta^{18}O$ values of tourmaline for each block. **c** Histogram of δD values of tourmaline for each block. **d** Histogram of $\delta^{18}O$ values of quartz according to veins with more and less than 1 g/t of gold. **e** Histogram of $\delta^{18}O$ values of tourmaline according to veins with more and less than 1 g/t of gold. **f** Histogram of δD values of tourmaline according to veins with more and less than 1 g/t of gold. Only veins with available gold grades are displayed in **d**, **e,** and **f**.

Table 1 Isotopic composition of vein minerals from the Augmitto-Bouzan segment.

Block	Sample	UTM Nad83 Zone 17N		Depth	Quartz	Tourmaline		Carbonate		T	H_2O	
		Easting	Northing		$\delta^{18}O$	$\delta^{18}O$	δD	$\delta^{18}O$	$\delta^{13}C$	Qtz-Tur	$\delta^{18}O$	δD
				m	VSMOW (‰)	VSMOW (‰)	VSMOW (‰)	VSMOW (‰)	VPDB (‰)	°C	VSMOW (‰)	VSMOW (‰)
Augmitto	19-GR-631AUG-02	641090	5339816	459.0	15.3							
	19-GR-124S-01	641482	5339553	60.2	14.1	10.3	-30			273	6.2	33
	19-GR-405S-14	641815	5339694	361.5	14.2	10.6	-53			282	6.7	7
	18BEQ0304AG01.4	641921	5339565	0.0	14.1							
	18BEQ0303AG01	641934	5339600	0.0	16.8							
	18BEQ0303AG01.2	641938	5339596	0.0	15.0							
	18BEQ0307AG01	641939	5339532	0.0				13.5	-2.8			
	18BEQ0308AG01.1	641939	5339528	0.0	13.7			11.5	-3.6			
	18BEQ0308AG01.2	641939	5339528	0.0								
	18BEQBEQ0309AG01.1	641950	5339526	0.0	13.5							
	18BEQBEQ0309AG01.2	641950	5339526	0.0								
	18BEQ0310AG01.2	641950	5339526	0.0	13.9							
	19-GR-442S-02	641962	5339532	23.4	13.9	11.4	-51			408	10.0	-20
	19-GR-442S-03	641962	5339532	23.6	11.8							
	19-GR-425S-05	642011	5339550	25.8	13.6							
	19-GR-425S-07	642011	5339543	34.2	14.7							
	19-GR-415S-04	642082	5339969	668.5	14.3	11.7	-59	11.7	-4.2	409	10.4	-29
Cinderella	19-GR-610CI-05	642458	5339710	278.3	14.4							
	19GR-535CI-01	642455	5339887	479.6	13.3							
	19-GR-535CI-05	642455	5339885	505.7	14.0			12.2	-3.4			
	19-GR-564CI-06	642737	5339839	523.1	14.4	11.9	-52	12.5	-3.0	420	10.8	-23
	19-GR-603CI-06	642825	5339649	117.4	15.2	10.8	-44			228	5.2	36
	19-GR-467CI-07	642930	5339845	395.7	14.2			11.6	-4.8			
	19-GR-467CI-08	642930	5339844	399.7	14.8							
	19-GR-467CI-09	642929	5339842	414.3	13.7	10.8	-41			359	8.6	-1
	19-GR-620CI-05	643745	5339678	50.6	16.1			12.3	-4.4			
	19-GR-620CI-06	643745	5339677	51.7	15.2	8.5	-33			*	*	
Lac Gamble	19-GR-500GA-04A	644328	5339940	681.5	12.5							

Table 1 Isotopic composition of vein minerals from the Augmitto-Bouzan segment. (Continued)

Block	Sample	UTM Nad83 Zone 17N		Depth	Quartz	Tourmaline		Carbonate		T	H_2O	
		Easting	Northing		$\delta^{18}O$	$\delta^{18}O$	δD	$\delta^{18}O$	$\delta^{13}C$	Qtz-Tur	$\delta^{18}O$	δD
				m	VSMOW (‰)	VSMOW (‰)	VSMOW (‰)	VSMOW (‰)	VPDB (‰)	°C	VSMOW (‰)	VSMOW (‰)
Lac Gamble	19-GR-500GA-04B	644328	5339940	681.5	14.7							
	19-GR-500GA-05A	644328	5339940	684.9	14.5							
	19-GR-500GA-05B	644328	5339940	684.9	14.7							
	19-GR-628GA-03	644374	5339849	490.4	14.5							
	19-GR-574GA-04A	644602	5340005	632.5	14.6							
	19-GR-574GA-04B	644602	5340005	632.5	15.2							
	19-GR-574GA-06	644602	5340005	630.8	14.4	11.0	-18			306	7.7	35
	19-GR-461GA-03	644672	5339742	264.2	14.3							
	19-GR-461GA-04A	644672	5339742	264.3	14.4							
	19-GR-461GA-04B	644672	5339742	264.3				12.1	-5.0			
	19-GR-461GA-06A	644672	5339739	268.9	13.8							
	19-GR-461GA-06B	644672	5339739	268.9	14.6							
Astoria	19-GR-10013AS-03	645760	5339871	116.4	14.4							
	19-GR-10010AS-06	645803	5339875	132.6	14.3							
	19-GR-638AS-02	645984	5339914	467.7	0.0	11.8	-34			344	9.3	9
	19-GR-638AS-05	645981	5339903	493.4	0.0			21.9	-6.5			
	18BEQ0011AG12	646077	5339729	0.0	13.9							
	18BEQ0011AG13	646091	5339711	0.0	14.6							
	18BEQ0011AG08	646093	5339717	0.0	13.7							
	18BEQ0011AG04	646094	5339771	0.0	13.8							
	18BEQ0011AG06	646104	5339765	0.0	14.2							
	18BEQ0011AG11.3	646106	5339754	0.0	14.5							
	18BEQ0011AG09	646107	5339776	0.0	14.4							
	18BEQ0011AG02.1	646118	5339780	0.0	15.4			11.3	-3.6			
	19-GR-299AS-08	646128	5339808	289.6	16.5							
	19-GR-656AS-03	646606	5340175	850.8	0.0	10.6	-29			363	8.5	10
	19-GR-645AS-02	646871	5339775	147.9	0.0	10.0	-37			228	4.4	43
	19-GR-645AS-06	646871	5339779	135.3	0.0	10.3	-20			285	6.5	39

Table 1 Isotopic composition of vein minerals from the Augmitto-Bouzan segment. (Continued)

Block	Sample	UTM Nad83 Zone 17N		Depth	Quartz	Tourmaline		Carbonate			T	H_2O	
		Easting	Northing		$\delta^{18}O$	$\delta^{18}O$	δD	$\delta^{18}O$	$\delta^{13}C$		Qtz-Tur	$\delta^{18}O$	δD
				m	VSMOW (‰)	VSMOW (‰)	VSMOW (‰)	VSMOW (‰)	VPDB (‰)		°C	VSMOW (‰)	VSMOW (‰)
East-Bay	19GR-650AS-04	647600	5339866	296.2	0.0			13.5	-4.0				
	19-GR-04EB-04	647931	5339778	119.0	11.4	9.7	-41	13.0	-6.2		235	4.4	36
	19-GR-04EB-05	647931	5339774	122.5	11.7								
Bouzan	19-GR-12A-01	648128	5339833	93.2	14.2								
	19-GR-12A-04	648128	5339807	119.0	14.8	10.4	-49				266	6.1	16
	19-GR-12A-05	648128	5339802	123.6	10.8								
	19-GR-476SC-01	648373	5340162	507.4		11.7	-51	12.9	-4.8				
	19GR-476Sc-03	648372	5340155	520.3	15.0			13.1	-5.3				
	19-GR-475SC-02	648559	5340001	298.0				15.0	-0.5				
	19GR-652BO-02	648801	5340049	254.1	16.7			14.5	-5.4				
	19-GR-483BW-03	649714	5340348	172.0	11.8			12.4	-1.8				
	18BEQ0013AG02	649999	5340336	8.8	12.7			12.8	-3.4				
	18BEQ0013BG06	649996	5340318	34.2	14.6								
	18BEQ0013CG08	649995	5340311	44.0	13.9								
	18BEQ0013DG18	649986	5340258	118.4	13.6			13.4	-0.9				
	19-GR-17A-01	650304	5340345	14.9	13.3	10.8	-31	12.61	-1.1		402	9.3	0
	19-GR-473BO-03	650867	5340498	91.7	14.8								
	19-GR-472BO-03	651529	5340554	67.2				14.6	-5.2				

Oxygen isotope equilibrium temperature is calculated using Kotzer et al. (1993). The $\delta^{18}O_{H2O}$ values were computed using temperature from Kotzer et al. (1993) and the quartz-H_2O fractionation of Matsuhisa et al. (1979). The δD_{H2O} values were computed using temperature and the tourmaline-H_2O fractionation of Kotzer et al. (1993).
*Quartz-tourmaline pairs not in equilibrium.

1.6.7 Equilibrium temperature and isotope composition (O, H) of water

Quartz-tourmaline pairs in the δ-δ diagram plot as a broad array between the 200 °C and the 550 °C isotherms (Fig. 15A). The 16 quartz-tourmaline pairs appear to be in isotopic equilibrium since they plot in the typical range of temperature for orogenic gold deposits (Goldfarb & Groves, 2015), except sample 19-GR-620CI-06 from the Cinderella block, which yields a temperature of 124 °C (Fig. 15A). Using the quartz-tourmaline fractionation from Kotzer et al. (1993), quartz-tourmaline pairs display equilibrium temperatures between 228 and 420 °C (321 ± 70; Table 1, Fig. 15A). A broad covariation between the temperature and the depth of the sample exists, as shown in Figure 15B, except for two quartz-tourmaline pairs close to the surface, which are hosted by an albitite dyke, in the Augmitto block, and by Blake River andesite, in the Bouzan area, in contrast to the other pairs which are hosted by Piché Group rocks. The calculated $\delta^{18}O$ values for water in equilibrium with quartz range from 4.4 to 10.8 ‰ (7.9 ± 2.0; Table 1) using the fractionation from Matsuhisa et al. (1979). The calculated δD values of water in equilibrium with tourmaline using Kotzer et al. (1993) range from –29 to 43 ‰ (10 ± 23). Both $\delta^{18}O_{H2O}$ and δD_{H2O} values covary with the calculated oxygen isotope equilibrium temperature values (Fig. 16). The isotopic composition of water in equilibrium with quartz and tourmaline forms a linear array between two fluid end-members. The first end-member is characterized by high $\delta^{18}O$ values up to 10.8 ‰, low δD values down to –29 ‰, and a high temperature (>400 °C; Fig. 15C, Fig. 16). The second end-member is characterized by low $\delta^{18}O$ values down to 4.4 ‰, high δD values up to 43 ‰, and a low equilibrium temperature (200-250 °C; Fig. 15C, Fig. 16).

The spatial distribution of $\delta^{18}O$ values of water in equilibrium with quartz within the Piché Group is shown in Figure 17. Results show two areas of high $\delta^{18}O_{H2O}$. The first is at depths from 400 to 600 m in the Augmitto-Cinderella blocks, with $\delta^{18}O_{H2O}$ values around 10 ‰. The $\delta^{18}O_{H2O}$ decreases towards the surface and on either side of this plume-like structure, reaching compositions around 6 ‰. The second is in the Astoria block, with $\delta^{18}O_{H2O}$ values up to 9 ‰ at depths of around 300 to 900 m. In between, the Lac Gamble block shows a constant $\delta^{18}O_{H2O}$ around 7.8 ‰. From the surface of the easternmost part of the Astoria to the Bouzan blocks, $\delta^{18}O_{H2O}$ values decrease to around 5-6 ‰. Nevertheless, caution must be exercised due to the low data density in some areas.

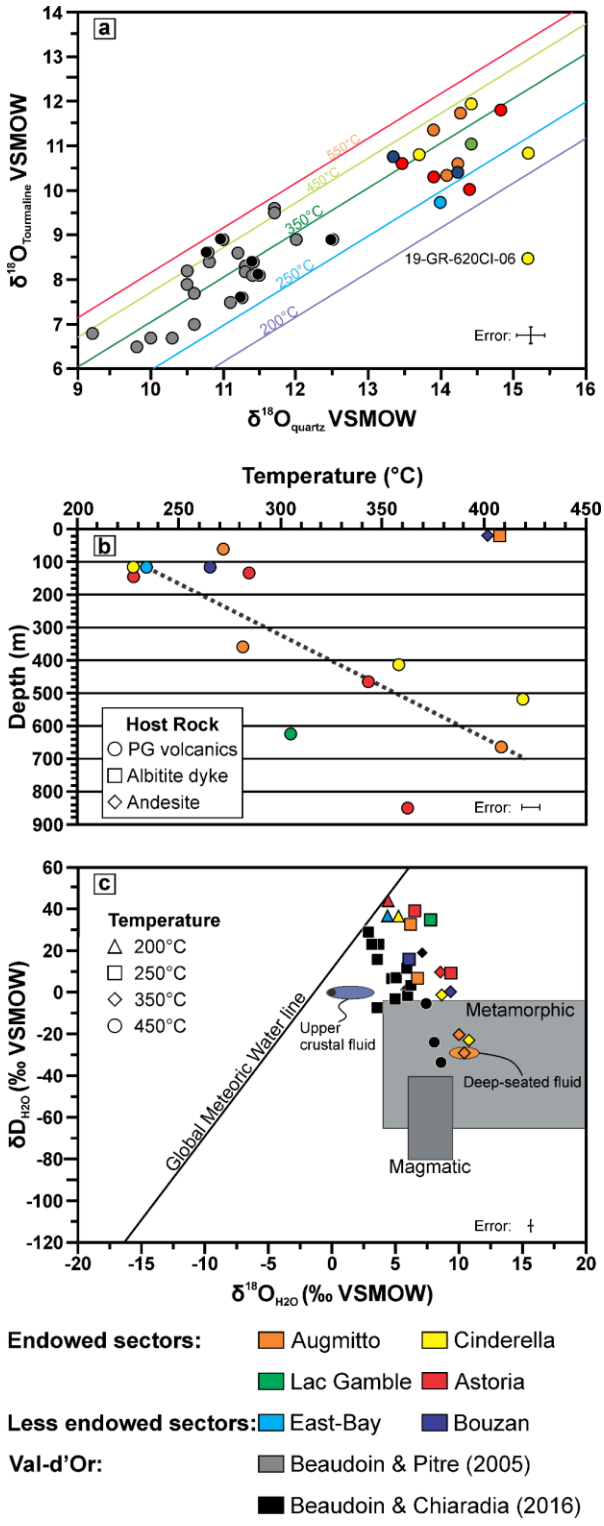

Figure 15 a Plot of $\delta^{18}O$ values of coexisting quartz and tourmaline in veins of the Augmitto-Bouzan segment (Table 1). Sample 19-GR-620CI-06 shows that the two minerals are not in equilibrium. The isotherms are calculated from Kotzer et al. (1993). **b** Variation of equilibrium temperature with depth (Table 1). **c** δD and $\delta^{18}O$ values of water of the Augmitto-Bouzan segment plotted into the compositional fields of natural water reservoirs from Sheppard (1986). δD_{H2O} values were calculated using Kotzer et al. (1993) and $\delta^{18}O_{H2O}$ using Matsuhisa et al. (1979). Data from Val-d'Or (Beaudoin & Pitre, 2005; Beaudoin & Chiaradia, 2016) are also plotted. PG = Piché Group.

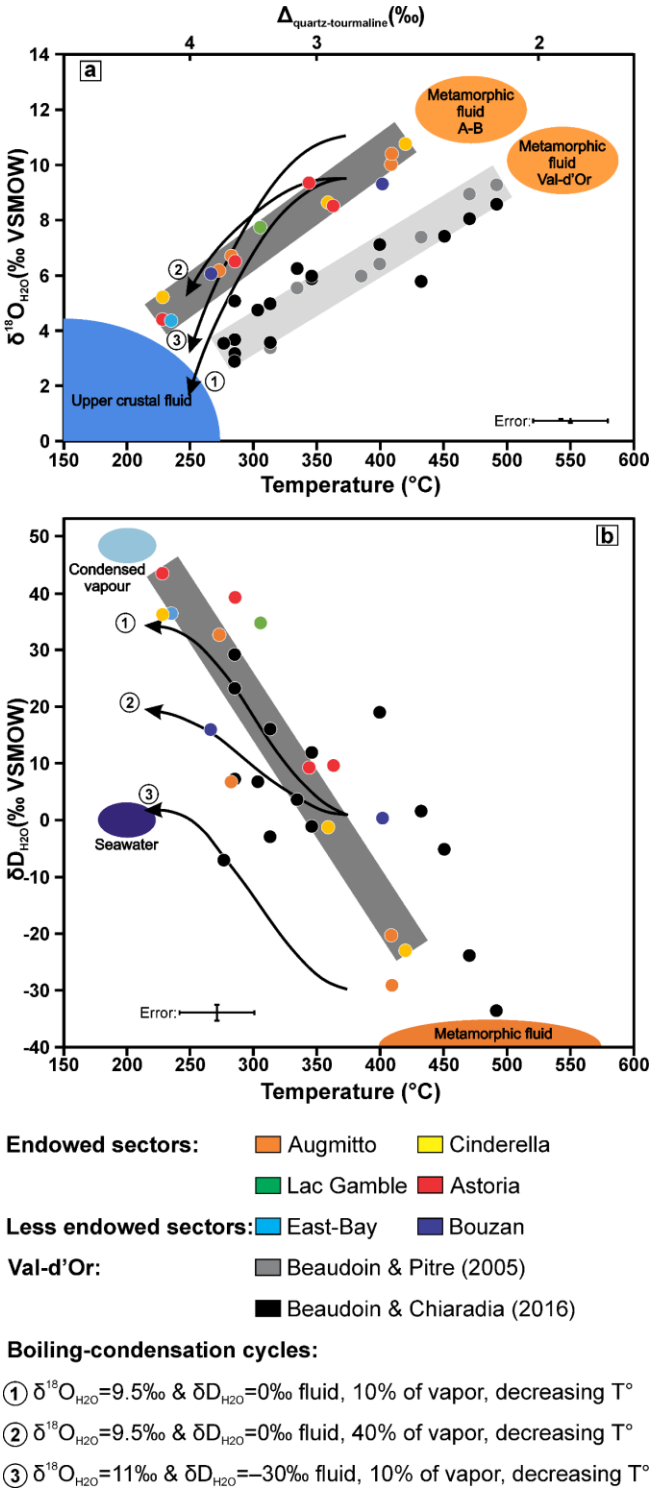

Figure 16 Diagram of **a** $\delta^{18}O_{H2O}$ versus quartz-tourmaline oxygen isotope equilibrium temperature of the Augmitto-Bouzan segment (A-B) compared to Val-d'Or (Beaudoin & Pitre, 2005; Beaudoin & Chiaradia, 2016). The bands display the fluid mixing paths. **b** δD_{H2O} versus quartz-tourmaline oxygen isotope equilibrium temperature. The arrows represent the effect of boiling-condensation cycles on the stable isotope composition of water during cooling. Evaporation of **1)** 10 % and **2)** 40 % vapor from a $\delta^{18}O_{H2O}$=9.5‰, δD_{H2O}=0‰ fluid and **3)** 10 % vapor from a metamorphic fluid ($\delta^{18}O_{H2O}$=11‰, δD_{H2O}= -30‰) and their condensation after each increment. Based on evaporation and condensation equations from Sharp (2017).

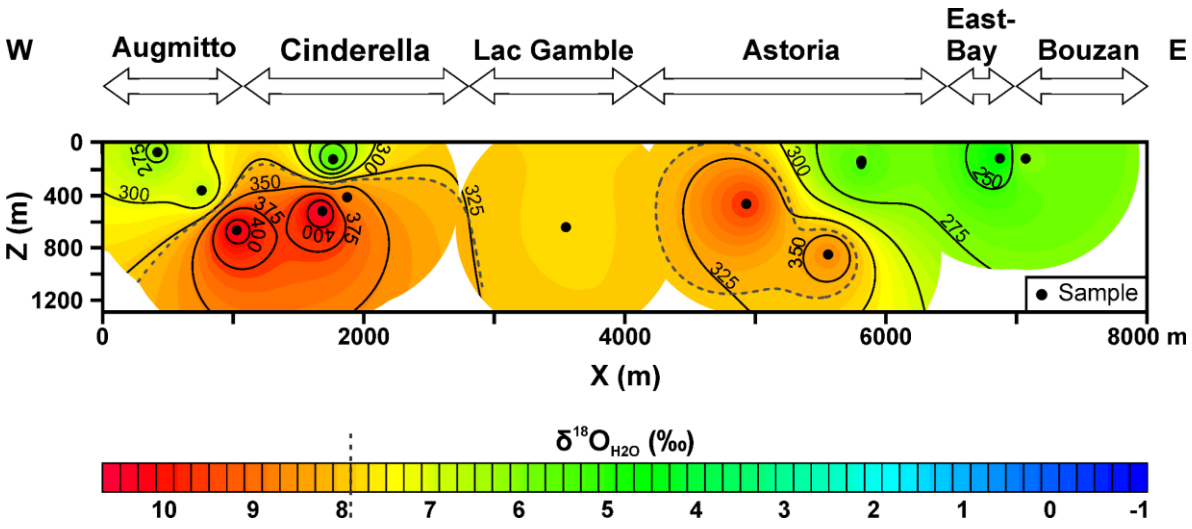

Figure 17 Interpolated $\delta^{18}O_{H2O}$ values calculated from Matsuhisa et al. (1979) in a longitudinal section within the Piché Group (CLLDZ). The dark grey dashed line represents the 8 ‰ isopleth. The interpolated temperature isotherms are displayed over the oxygen isotope zonations based on quartz-tourmaline equilibrium temperatures in Figure 15B (Table 1). Both interpolations were produced using IDW, described in Appendix A. A buffer zone of 850 m between each sample point has been established, based on half of the longest distance between two samples.

1.6.8 Numerical modelling of fluid flow

1.6.8.1 Domain and boundary conditions

The domain used for the simulation is a rectangular prism with a length of 15 km, a width of 5 km, and a depth of 2 km. The domain is discretized using 50 m elements on the X-axis, 10 m elements on the Y-axis, and 50 m elements on the Z-axis. The model contains four subvertical rock units (Fig. 18), representing a simplistic depiction of the four groups of Archean rocks in the study area (Fig. 2). Each geological unit is defined as a porous matrix with different hydraulic and isotopic properties based on their principal rock types (Table 2). The matrix is considered fully saturated, as in Beaudoin et al. (2006). Since the Piché Group is considered the physical expression of the CLLDZ, it has been assigned a high hydraulic conductivity, typical of fault zones, throughout its volume (Table 2). A hydraulic head of 200 m is assigned at the inflow boundary, i.e., the lowermost plane of the Z-axis, from where a fluid with a constant $\delta^{18}O$ of 10 ‰ infiltrates the model flowing upwards, based on the high $\delta^{18}O$ end-member water composition (Fig. 15C, Table 1). Its oxygen isotope composition is slightly higher than the deep-seated fluid measured in the studies of Beaudoin and Pitre (2005), Beaudoin et al. (2006), and Beaudoin and Chiaradia (2016) in the Val-d'Or area. The rock porosity is filled by an interstitial fluid with an initial $\delta^{18}O$ value of 1 ‰, based on the extrapolated isotopic composition of the low $\delta^{18}O$ fluid end-member (Fig. 15C, Table1). This composition is marginally lighter than that of the upper crustal reservoir of Beaudoin and Chiaradia (2016) in the Val-d'Or area. A thermal gradient is simulated in the Piché Group by assigning a decreasing fractionation factor by steps of 50 °C for every 150 m, from a depth of 800 m to the top, based on

the observed temperature gradient (Fig. 15B). Below 800 m, the system is assumed to be isothermal at 450 °C, and every other unit of the model is assumed to be isothermal at 350 °C.

Table 2 Hydraulic and isotopic properties of the numerical model

Property	Value	Unit	Source*	Property	Value	Unit	Source*
Saturated porous matrix				*Fluid*			
Longitudinal dispersivity	14.83	m	1	Free-solution diffusion coefficient	2.0×10^{-9}	m^2/sec	3
Transverse dispersivity	1.48	m	1	$\delta^{18}O$ of infiltrating fluid	10	‰	
Vertical transverse dispersivity	0.15	m	1	$\delta^{18}O$ of interstitial fluid	1	‰	
Reverse rate of reaction	3.2×10^{-13}	sec^{-1}	3, 17	*Isotope exchange*			
Blake River Group mafic volcanic rocks				Blake River Group mafic volcanic rocks			
Hydraulic conductivity	10^{-8}	m/sec	4	Oxygen-rock water mass ratio	7		
Porosity	18	%	4, 16	Fractionnation factor (350°C)	1.0018		2
Tortuosity	0.011		5	Timiskaming & Pontiac Group greywackes			
Specific storage	4.3×10^{-7}	m^{-1}	6	Oxygen rock-water mass ratio	61		
$\delta^{18}O_{Rock}$	8	‰	7	Fractionnation factor (350°C)	1.0049		2
Density	2983	kg/m^3		Piché Group komatiites (talc-carbonate schist)			
Timiskaming & Pontiac Group greywackes				Oxygen rock-water mass ratio	23		
Hydraulic conductivity	10^{-9}	m/sec	8, 4	Fractionnation factor 200°C	1.0107		2
Porosity	2.5	%	9	Fractionnation factor 250°C	1.0081		2
Tortuosity	0.0135		10	Fractionnation factor 300°C	1.0062		2
Specific storage	2.1×10^{-6}	m^{-1}	6	Fractionnation factor 350°C	1.0048		2
$\delta^{18}O_{Rock}$ Timiskaming	8.60	‰		Fractionnation factor 400°C	1.0038		2
$\delta^{18}O_{Rock}$ Pontiac	9.85	‰	11	Fractionnation factor 450°C	1.0029		2
Density	2726	kg/m^3					
Piché Group komatiites (talc-carbonate schist)							
Hydraulic conductivity	7.93×10^{-6}	m/sec	3				
Porosity	6.5	%	12, 13				
Specific storage	8.6×10^{-7}	m^{-1}	6				
$\delta^{18}O_{Rock}$	5.50	‰	14, 15				
Density	2787	kg/m^3					

*1- Xu and Eckstein (1995); 2- calculated from Vho et al. (2019); 3- Beaudoin et al. (2006); 4- Singhal and Gupta (2010); 5- Heap and Kennedy (2016); 6- Kuang et al. (2020); 7- Beaudoin et al. (2014); 8- Domenico and Schwartz (1998); 9- Mielke et al. (2016); 10- Srisutthiyakorn and Mavko (2016); 11- Raskevicius et al. (2019); 12- Börner et al. (2018); 13- Banerjee et al. (2011); 14- Lahaye and Arndt (1996); 15- Eiler (2001); 16- Heap et al. (2015); 17- Cole et al. (1992).

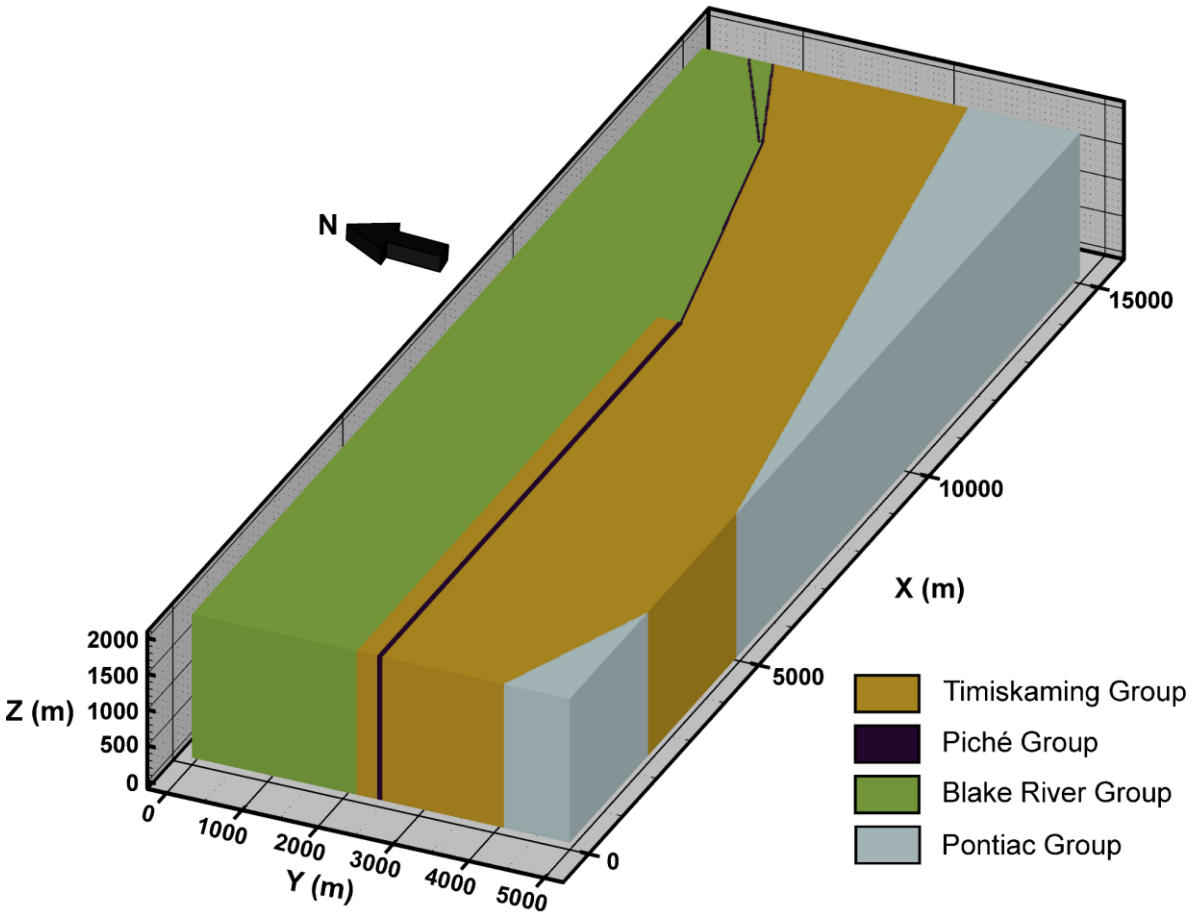

Figure 18 3D model showing the distribution of the four lithological units based on the geology of the study area (Fig 2). The assigned hydraulic and isotopic properties are in Table 2.

Four different boundary condition scenarios were adapted from Beaudoin et al. (2006) and tested to identify the most appropriate scenario (Appendix E1). The lateral boundaries of the model were considered impermeable for every scenario. For scenario A, the bottom and top boundaries are permeable with an assigned fixed head, where fluid inflow and outflow occur, respectively. For scenario B, the bottom and top boundaries are impermeable, except along the trace of the Piché Group (CLLDZ), where fluid inflow and outflow are allowed. For scenario C, the bottom boundary is impermeable, except along the trace of the Piché Group where fluid inflow occurs, while the top surface is assumed to be a permeable outflow boundary. Finally, for scenario D, the base of the model is assumed open, with the outflow boundary being at the top and limited to the trace of the Piché Group in an otherwise impermeable top boundary.

The simulations for scenario A show that the system reached solute transport steady-state at the earliest stages after 1000 years (Appendix E2). At this time, the $\delta^{18}O_{H2O}$ values of water in the Piché Group are homogeneous at around 10 ‰ throughout the model. Such uniformity of the oxygen isotope composition of the

fluid does not correlate with the variations observed in the field (Fig. 17). Scenario B displays a similar evolution with time as scenario A, where water in the Piché Group has the same isotopic composition as the infiltrating fluid (10 ‰) after 100,000 years, but with $\delta^{18}O_{H2O}$ values of around 8 ‰ in the lower 200 m of the Bouzan segment after 1000 years (Appendix E3). These boundary conditions yield a difference in the oxygen isotope composition of the fluid between the endowed and less endowed sectors. However, their $\delta^{18}O$ values are higher compared to those measured in Figure 17, and therefore the boundary conditions of scenario B fail to reproduce the measured isotopic compositions. The results of scenario C (Appendix E4) are similar to scenario A, where the $\delta^{18}O$ composition of the fluid in the Piché Group is almost the same as the infiltrating fluid (10 ‰). This homogeneous composition is produced at the earliest stages of infiltration, showing that the system reached solute transport steady-state after around 1000 years. Simulations using scenario D show a depletion of $\delta^{18}O_{H2O}$ between X = 8870 and 11100 m, which corresponds to the less endowed sectors (Fig. 19), with $\delta^{18}O_{H2O}$ values as low as 6 ‰ towards the surface after 1000 years. This zone with lower $\delta^{18}O_{H2O}$ values corresponds to the area where the Piché Group has reduced thickness, from 70 m to 30 m, where it changes in orientation from east-west to northeast-southwest, and where its northern contact is with volcanic rocks instead of sedimentary rocks (Fig. 18). The model results are consistent with the interpolated $\delta^{18}O_{H2O}$ values of 5-6 ‰ in the East-Bay and Bouzan blocks (Fig. 17). For the same time period, the other areas of the Piché Group yield a constant fluid oxygen isotope composition of 10 ‰ (Fig. 19A). The model shows a homogeneous steady-state solute transport after 250 000 years, with $\delta^{18}O_{H2O}$ composition of 10 ‰ throughout the whole Piché Group (Fig. 19D). The difference in $\delta^{18}O_{H2O}$ between endowed and less endowed sectors from the numerical model of scenario D provides the best match with the oxygen isotope isopleths measured on the field (Fig. 17).

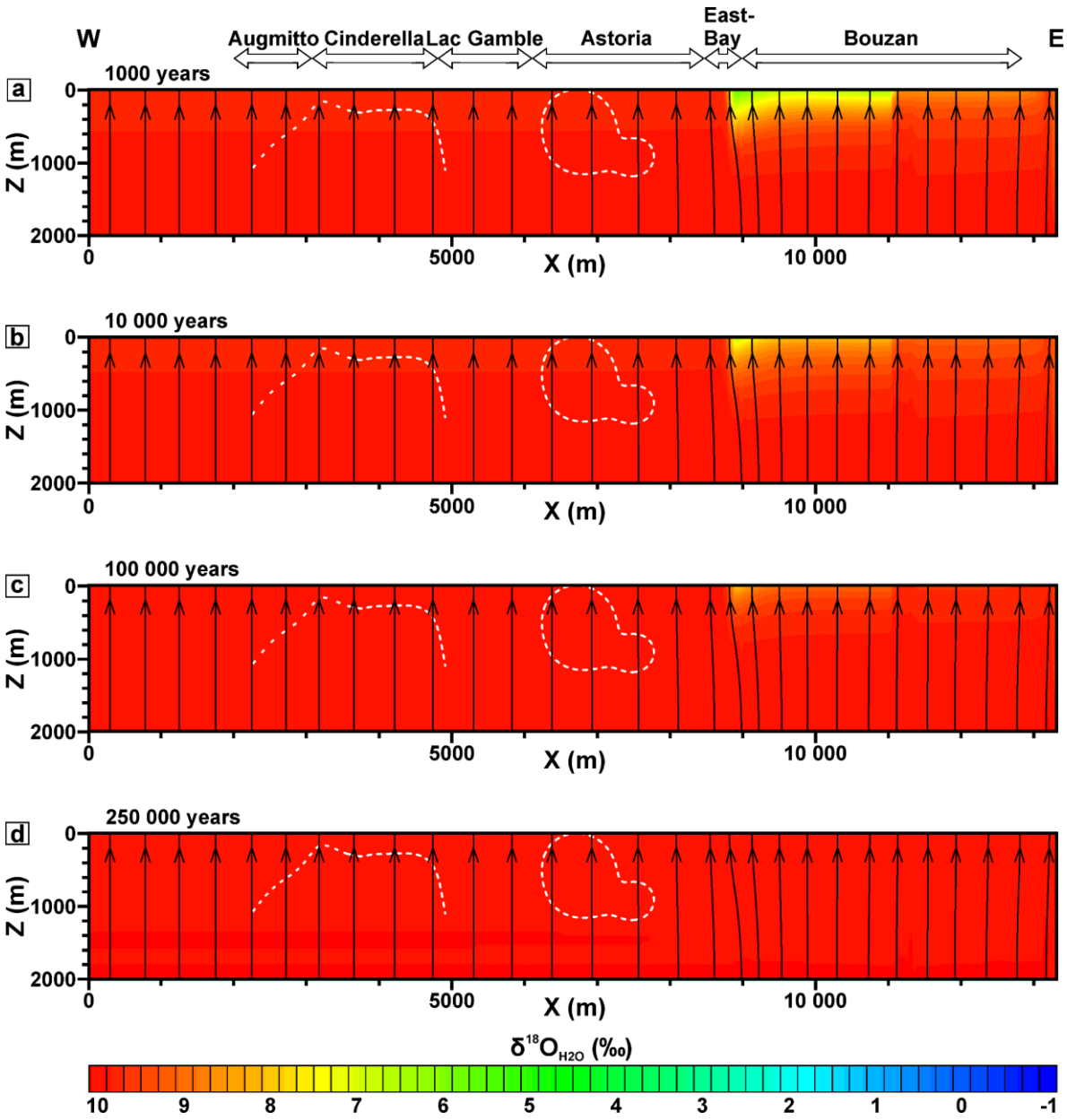

Figure 19 Simulated $\delta^{18}O_{H2O}$ values for boundary conditions of scenario D (Appendix E1) after (**a**) 1000, (**b**) 10 000, (**c**) 100 000, and (**d**) 250 000 years in a longitudinal section within the Piché Group. The streamlines are displayed to show the direction of the infiltrating fluid. The white dashed line represents the 8 ‰ isopleth of Figure 17.

1.6.8.2 Numerical model results

However, these initial conditions do not reproduce the plumes of higher $\delta^{18}O$ in the Augmitto-Cinderella and Astoria blocks. To reproduce the field data, we added higher hydraulic conductivity corridors of 7.93×10^{-6} m/s, one order of magnitude higher than the surrounding rock in areas of high $\delta^{18}O$ (Fig. 20). The higher conductivity corridors have been assigned fractionation representing temperatures of 450 °C, from depths of 2000 to 1000 m, and 400 °C from 1000 to 400 m, based on the computed equilibrium temperatures in these

zones (Table 1). The results of the model (Fig. 21) show two plumes of high $\delta^{18}O$ (~ 10 ‰) form in the Augmitto-Cinderella and Astoria blocks that expand towards the surface. For the first 10,000 years of the simulation, at the surface and on either side of those plumes, $\delta^{18}O$ values in the endowed sectors are lower, similar to what is observed in Figure 17. Further away from the plumes' influence, the $\delta^{18}O_{H2O}$ values are around 7.2 ‰ and increase gradually with depth at approximatively 0.2 ‰ per 100 m. At X = 8870 m, the oxygen isotope isopleths decrease abruptly to around 4.5 ‰ until a depth of ~ 800 m. This corresponds to the area where the Piché Group thickness decreases, changes strike towards the northeast, and is in contact with volcanic rocks to the north. Between 11100 and 11450 m along the x-axis, $\delta^{18}O$ values are slightly higher than their surroundings. These values correspond to an area in the model where the Piché Group is 10 m wider in order to reproduce its original orientation observed on the field (Fig. 2) while working with 50 m×10 m×50 m rectangular prisms that form the model's grid. After 10 000 years, the water reaches a solute transport steady-state composition with a uniform value of 10 ‰ (Fig. 21C-D), which is that of the infiltrating fluid. The model reasonably replicates the isopleths measured in the field (Fig. 17) after 1000 to 10 000 years (Fig. 21A-B).

At the beginning of every simulation, a transient flow and solute transport have been modelled, where steady-state fluid flow is reached before the first time step, as shown by the constant streamlines with each time increment (Fig. 19, Fig. 21, Appendix E). The timescale to reach steady-state for solute transport is thus quite larger than it is to reach steady-state fluid flow, as conveyed by the varying $\delta^{18}O_{H2O}$ concentrations over time (Fig. 19, Fig. 21, Appendix E).

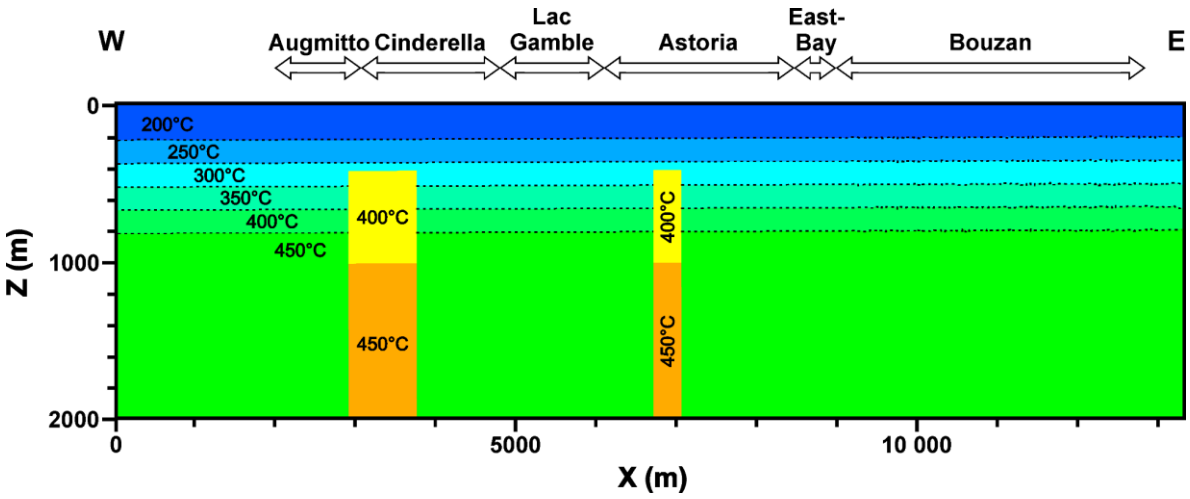

Figure 20 Variation in the equilibrium temperature in a longitudinal section within the modelled Piché Group. Corridors with higher conductivity (orange and yellow) of 7.93 × 10^{-6} m/s have been assigned between X = 2910 and 3770 m and X = 6710 and 7070 m extending from depths of 400 to 2000 m. The surrounding zones have a conductivity of 7.93 × 10^{-7} m/s. The thermal gradient observed in the field (Fig. 15B) has been modelled by assigning decreasing fractionation steps of 50 °C for every 150 m until a depth of 800 m, below which the model is considered isothermal at 450 °C. Fractionation temperatures in the high conductivity corridors are assigned according to the computed temperatures of Figure 17 (Table 1).

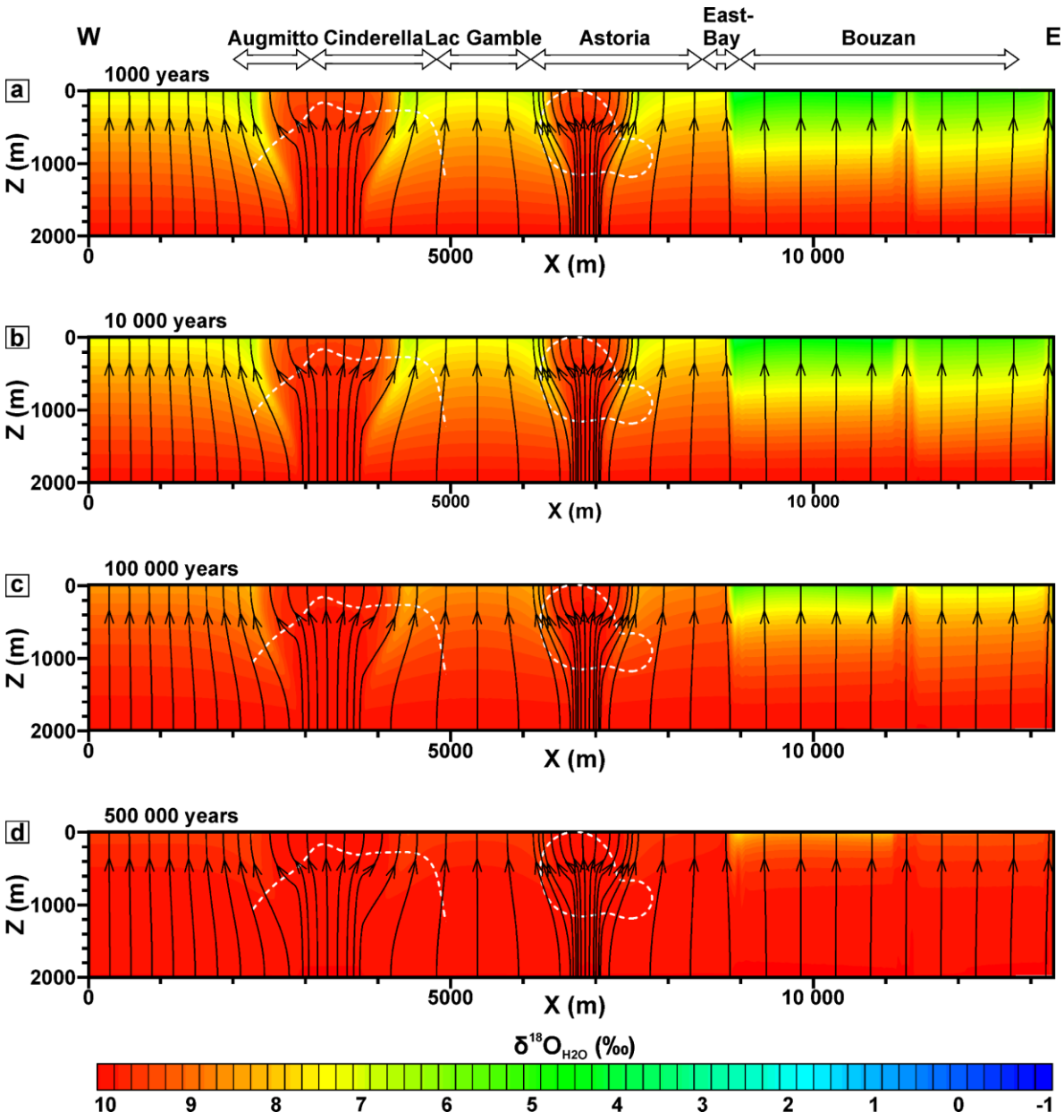

Figure 21 Simulated $\delta^{18}O_{H2O}$ values for the model with high conductivity corridors (Fig. 20) with boundary conditions of scenario D (Appendix E1) after (**a**) 1000, (**b**) 10 000, (**c**) 100 000, and (**d**) 500 000 years within the Piché Group. The streamlines are displayed to show the direction of the infiltrating fluid. The white dashed line represents the 8 ‰ isopleth of Figure 17.

1.7 Discussion

1.7.1. Sources of hydrothermal fluids

1.7.1.1 Sources of water

Knowing the aqueous fluid's oxygen and hydrogen isotope compositions allows discrimination of fluid sources by comparing the values with other natural reservoirs and can also bring forth physical processes

involved (e.g., Sheppard, 1986; Beaudoin & Chiaradia, 2016; Quesnel et al., in press). The calculated water isotope composition from the study area plots within, or above, the metamorphic box from Sheppard (1986; Fig. 15C) and outside the magmatic water composition field such that a magmatic origin is unlikely. The large spread of water isotopic compositions (Fig. 15C, Fig. 16A) and the observed linear distribution suggest that the distribution of the $\delta^{18}O_{H2O}$ and δD_{H2O} results from mixing between two fluid end-members. The first end-member is characterized by high $\delta^{18}O_{H2O}$ (> 11 ‰), low δD_{H2O} (< –30 ‰), and high temperature (> 420 °C). It is consistent with a deep-seated metamorphic water source (Fig. 15C) often proposed as mineralizing fluids for orogenic gold deposits, including for the Val-d'Or vein field (Beaudoin & Pitre, 2005; Olivo et al., 2006; Beaudoin & Chiaradia, 2016). The second end-member is distinguished by its low $\delta^{18}O_{H2O}$ (< 4 ‰), high δD_{H2O} (> 40 ‰), and low temperature (< 230 °C), interpreted as a shallower, upper crustal origin (Fig. 15C). The source of this second fluid endmember is difficult to establish. A meteoric origin is unlikely as most of the rocks of the area were likely submerged during the Archean (Beaudoin & Pitre, 2005; Beaudoin & Chiaradia, 2016). In addition, records of meteoric fluids in orogenic gold deposits are often attributed to post-mineralization events (Quesnel et al., in press), and fluid inclusion microthermometry is not consistent with infiltration of meteoric fluids in deposits associated with the CLLDZ, including Astoria (Neumayr et al., 2007). The low $\delta^{18}O_{H2O}$ value of this second fluid endmember is consistent with trapped Archean seawater, which is known to have similar oxygen isotope signatures to its contemporary counterpart (Kyser et al., 1999; Pope et al., 2012), and has also been proposed by Beaudoin and Pitre (2005) in Val-d'Or. However, the recorded δD_{H2O} values are higher than expected for seawater. The high δD_{H2O} values of this fluid can be explained by successive cycles of flash vaporization during pressure release by activation of a fault-valve system (Sibson et al., 1988; Weatherley & Henley, 2013) and condensation during pressure increase of the sealed system (Fig. 16B), as detailed in Beaudoin and Chiaradia (2016) and Quesnel et al. (in press). These phase separation events would significantly increase the δD_{H2O} values of the fluids involved with decreasing temperature, while slightly lowering the $\delta^{18}O_{H2O}$ values (Fig. 16). However, flash vaporization-condensation cycles of a cooling metamorphic fluid cannot solely explain the observed trend. Indeed, continuous fluid mixing is necessary to replicate the measured oxygen isotope compositions (Fig. 16). In addition, phase separation is not possible under 374 °C, where fluid mixing is assumed the dominant mechanism. Those two hydrothermal water sources are consistent with multiple studies of orogenic gold systems along the CLLDZ (e.g., Beaudoin & Pitre, 2005; Olivo et al., 2006; Beaudoin & Chiaradia, 2016; Daver et al., 2020).

The Augmitto-Bouzan segment presents higher $\delta^{18}O$ values of quartz, tourmaline (Fig. 15A), carbonate (Fig. 13), and aqueous fluids (Fig. 16A), systematically ~ 2 ‰ more elevated in $\delta^{18}O$ than in the Val-d'Or vein field (Beaudoin & Pitre, 2005; Olivo et al., 2006; Neumayr et al., 2007; Beaudoin & Chiaradia, 2016). Neumayr et al. (2007) attributed this shift to higher oxygen exchange with the host rocks in higher-order faults (Val-d'Or), in contrast to lower fluid/rock ratios in deposits located directly in the CLLDZ. Quesnel et al. (in press) observed

that vein minerals hosted in igneous rocks, like deposits in Val-d'Or, have lower $\delta^{18}O$ values than those hosted in volcano-sedimentary rocks, such as those along the Augmitto-Bouzan segment. Thus, the observed difference in $\delta^{18}O$ signatures could be explained by oxygen isotope exchange during fluid-rock interactions, where fluid exchange with volcano-sedimentary host rocks with higher $\delta^{18}O$ values will lead to more elevated fluid oxygen isotope composition in the Augmitto-Bouzan segment. Equally, fluid-rock exchange with sedimentary rocks would be more likely to yield a higher $\delta^{18}O$ composition, compatible with the slightly higher $\delta^{18}O$ of the upper crustal end-member of the segment compared to Val-d'Or (Fig. 16). Thus, the higher $\delta^{18}O$ of the deep-seated metamorphic fluid at Augmitto-Bouzan compared to Val-d'Or (Fig. 16) must represent a source rock with heavier oxygen isotope composition, perhaps as a result of devolatilization of a higher proportion of sedimentary rocks or low temperature altered volcanic rocks, compared to the source of fluids in Val-d'Or (Quesnel et al., in press).

The spatial variation of equilibrium temperatures also suggests fluid mixing. The temperature variations with depth indicate a large thermal gradient averaging 32 °C per 100 m (Fig. 15B). This is ten times higher than the typical ~ 30 °C/km Archean geothermal gradient (Martin, 1993; Nicoli et al., 2016). This high thermal gradient and its overlap with the Augmitto-Cinderella and Astoria ore shoots suggest progressive mixing between the upwelling hot metamorphic fluid with the lower temperature upper crustal pore fluid. Two samples plot outside the measured thermal gradient (Fig. 15B) and are hosted in an albitite dyke and Blake River andesite host rocks. These two samples are the only quartz-tourmaline veins sampled outside the Piché Group, were collected near the surface, and have quartz-tourmaline equilibrium temperatures around 400 °C (Fig. 15B), suggesting that this thermal gradient and hot metamorphic fluid upwelling occurred exclusively in the Piché Group rocks and along the higher permeability structures of the CLLDZ. This also suggests that the upper crustal fluids more easily circulated through the Piché Group, or were already present in higher volume at the inception of the hydrothermal system

Advection of deep-seated, metamorphic fluids towards higher crustal levels in orogenic gold deposits has been advocated by several authors (e.g., McCuaig & Kerrich, 1998; Beaudoin et al., 2006; Phillips & Powell, 2010). However, the infiltration pattern of these presumably hotter fluids has not yet been documented, and isothermal conditions have often been assumed, because of the lack of evidence for a thermal gradient (e.g., Kishida & Kerrich, 1987; Robert & Kelly, 1987; Robert et al., 1995; Ridley et al., 1996; McCuaig & Kerrich, 1998; Beaudoin & Pitre, 2005; Beaudoin et al., 2006; Olivo et al., 2006). This study specifically selected regularly distributed samples, both longitudinally and vertically, along the trace of the CLLDZ, which enabled detection of the thermal gradient, perhaps unlike previous studies which only considered depth, such as at the Sigma deposit (Beaudoin & Chiaradia, 2016). Alternatively, this could also be related to the less common geological setting of the segment being in the plane of the CLLDZ since most orogenic gold deposits worldwide are associated with

subsidiary structures away from the plane (Groves et al., 1998). Advection of deep-seated hot metamorphic fluid across the segment is also corroborated by the large carbonate alteration haloes, which can reach up to near 90 m wide (Chapon et al., 2013).

The interpolation of the few $\delta^{18}O_{H2O}$ values within the Piché Group rocks in the less endowed sectors suggests fluid flow was dominated by a larger proportion of the upper crustal end-member than in endowed blocks, shown by the lower $\delta^{18}O_{H2O}$ values and lower temperatures (Fig. 17). Blocks with substantial gold endowment (Fig. 3) also appear to be directly linked to large pulses of the deep-seated metamorphic fluid at high temperatures and with elevated $\delta^{18}O_{H2O}$ (Fig. 17). These variations between sectors could potentially explain the variation of gold content across the segment. Indeed, this indicates that gold precipitated in veins with higher proportions of deep-seated fluids, suggesting that the deep-seated fluid was the main gold transporter. This is consistent with the evidence from the Pontiac sediments that prograde metamorphism can source the deep-seated fluid in components like water and gold by depleting them from their original host rock (Pitcairn et al., 2017; Pitcairn et al., 2021).

1.7.1.2. Source of CO_2

Most of the quartz-carbonate pairs of the dataset appear in oxygen isotope disequilibrium, plotting outside of the geologically reasonable 220-450 °C isotherms (Appendix F; Goldfarb & Groves, 2015; Quesnel et al., in press). Thus, they are not suitable to use as geothermometers. Similar disequilibrium has been documented in other orogenic gold systems (Kontak & Kerrich, 1997; Beaudoin & Pitre, 2005) and is thought to be the result of a late retrograde oxygen isotope reequilibration at low temperature of the carbonate minerals with surface water (Appendix F; Sharp & Kirschner, 1994; Kontak & Kerrich, 1997; Beaudoin & Pitre, 2005; Quesnel et al., in press). The dolomite outlier from Astoria (Fig. 12A-C) has most likely been more affected by this phenomenon than the other samples. This could be related to the reequilibration of the dolomite with late and localized fluids associated with the intrusion of the Proterozoic dykes in Astoria. The $\delta^{13}C$ and $\delta^{18}O$ compositions of vein and host rock carbonates are similar, likely indicating that they originated from the same hydrothermal system.

The small $\delta^{13}C$ fractionations of 0.0 to –2.2 for dolomite-CO_2 and –0.9 to –2.7 for calcite-CO_2 between 230 and 420 °C (Ohmoto & Rye, 1979), respectively, indicates that the $\delta^{13}C$ composition of the carbonates resembles its CO_2 source. This range of temperature is based on the minimum and maximum quartz-tourmaline equilibrium temperatures (Fig. 15A; Table 1). The CO_2 that formed the carbonate phases of the study area falls into the range of composition of three possible sources. The first two correspond to deep-seated igneous or subcontinental sources (Quesnel et al., in press), which is unlike the previous interpretation of the sources of mineralizing fluids based on the isotopic signature of the quartz and the tourmaline. The $\delta^{13}C$ of CO_2 could also

be a product of prograde metamorphism of reduced carbon-bearing sedimentary rocks (Zhang et al., 1989; Madu et al., 1990; Oberthuer et al., 1996; Quesnel et al., in press), which is more consistent with the proposed metamorphic source for water. Mixing of two CO_2 sources remains a possibility, as discussed in Beaudoin and Pitre (2005), and would most likely be between a metamorphic ($\delta^{13}C > -6.2$ ‰) and an upper crustal ($\delta^{13}C \sim 0$ ‰) source, such as CO_2 dissolved in seawater-derived (Quesnel et al., in press).

1.7.2. Spatial variation of fluid/rock ratios

In this section, the possible links between spatial variation of gold endowment and variation fluid rock interaction, i.e., fluid/rock ratio, are investigated by following Taylor (1978) for an open-system where:

$$F/R = \ln\left[\frac{\delta^{18}O^{i}_{H_2O} + \Delta - \delta^{18}O^{i}_{rock}}{\delta^{18}O^{i}_{H_2O} - \left(\delta^{18}O^{f}_{rock} - \Delta\right)}\right] \quad (1)$$

where $\delta^{18}O^{f}$ and $\delta^{18}O^{i}$ are the final and initial isotopic compositions, F is the molar percent of oxygen in the fluid, R is the molar percent of rock oxygen, and $\Delta = \delta^{18}O^{f}_{rock} - \delta^{18}O^{f}_{H2O}$. The fluid/rock ratios calculated from these equations are indicators of fluid-rock interactions and assumed to be minimum values (Taylor, 1978; Ohmoto, 1986). The $\delta^{18}O^{f}_{rock}$ values correspond to the measured whole-rock isotopic compositions (Fig. 12A-D Appendix B). The rock-water (Δ) fractionations were calculated based on the modal mineral compositions determined in thin sections and by using mineral-H_2O equations for oxygen isotopes from Vho et al. (2019; Appendix G).

An initial oxygen isotope composition ($\delta^{18}O^{i}_{rock}$) of 5.5 ‰ is assumed for host rocks from the Piché Group, based on studies of unaltered komatiitic to basaltic rocks (e.g., Smith et al., 1984; Taylor & Sheppard, 1986; Gruau et al., 1992; Lahaye & Arndt, 1996; Eiler, 2001; Polat et al., 2018; Sarkar et al., 2018). Since Δ is a function of temperature, and temperature varies vertically and laterally in these rocks (Fig. 15B, Fig. 17), the assigned temperatures are based on the quartz-tourmaline equilibrium temperature from vein samples nearest the host rock sample (Table 1; Appendix B). Where no data was available, the temperature was based on the interpolation of Figure 17. Similarly, the composition of the fluid varies significantly due to mixing, thus the initial composition of the water ($\delta^{18}O^{i}_{H2O}$) was based on the measured (Table 1), as well as interpolated values (Fig. 17) for host rock samples with no associated quartz-tourmaline sample. Fluid/rock ratios were not computed for the two tremolite-chlorite samples since they are not representative of the hydrothermal alteration but rather of late contact metamorphism with Proterozoic dykes.

For Timiskaming greywackes, an initial oxygen isotope composition ($\delta^{18}O^{i}_{rock}$) of 8.6 ‰ is used, based on the whole-rock composition of a sample taken 600 m south of the CLLDZ and assumed to be the least altered

sample from the area, since no data is available in the literature. Because no data constrain the temperature of the greywacke host rocks, they were assigned a reasonable temperature of 300 ± 50 °C. The oxygen isotope composition of the fluid ($\delta^{18}O^{i}_{H2O}$) was assumed to be constant at 10 ‰ in greywacke, based on the composition of metamorphic water in equilibrium with this rock type (Fig. 15C, Fig. 16A).

The initial oxygen composition of the albitite dyke ($\delta^{18}O^{i}_{rock}$) was assumed at 5.8 ‰, based on the composition of unaltered gabbroic rocks found in the literature (Kalamarides, 1984; Gao et al., 2006; Furnes et al., 2007; Polat et al., 2018). Similarly to the greywackes, due to the lack of temperature constraints, a reasonable temperature of 300 ± 50 °C was assigned. An initial oxygen isotope composition of 10 ‰ was assigned to the fluid ($\delta^{18}O^{i}_{H2O}$) based on the computed values in the albitite dyke in Augmitto, which is near the deep-seated metamorphic end-member. It is also assumed that fluid mixing was limited in these host rocks since the Augmitto sample does not follow the thermal gradient (Fig. 16B). Every parameter and computed ratio are found in Appendix G.

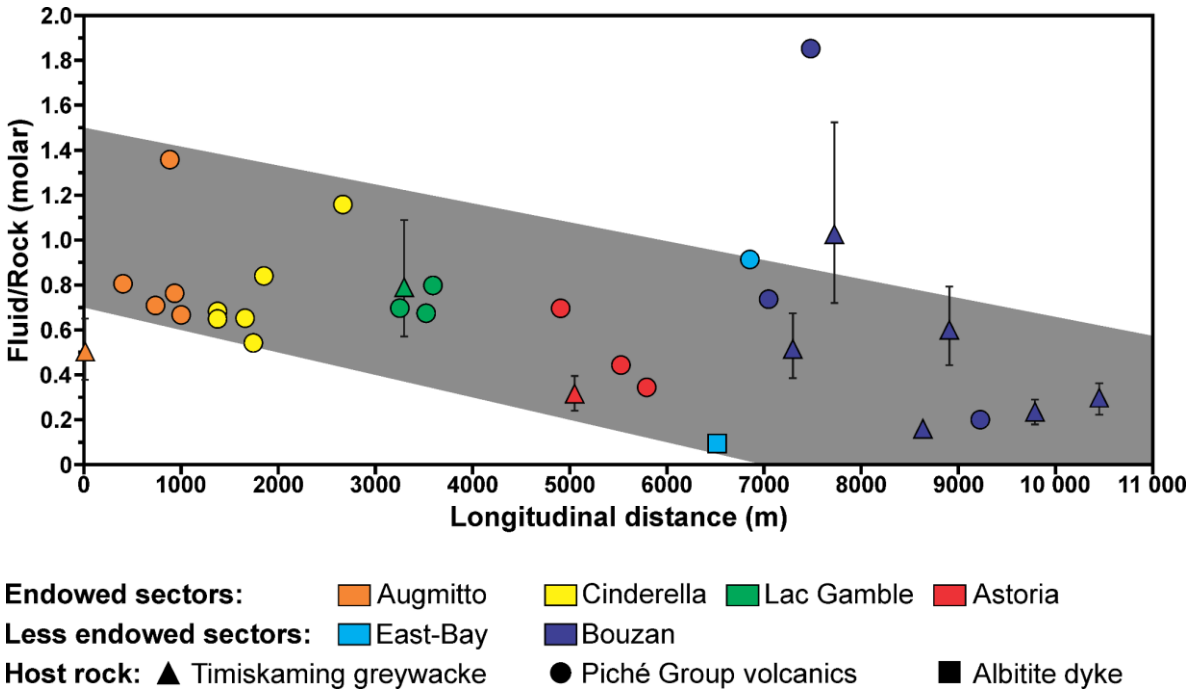

Figure 22 Open-system fluid/rock ratios versus the longitudinal distance across the segment. The lower and upper brackets of the Timiskaming Group greywacke represent fluid/rock ratios at 250 and 350 °C, respectively. The shifts in fluid/rock ratios of the albitite dyke between 250 and 350 °C are too low to be displayed. The grey band encompasses maximum and minimum fluid/rock ratios along the segment.

Overall, the average fluid/rock ratios of the host rocks across the Augmitto-Bouzan segment are relatively low and similar to those computed for the Malartic deposit (Raskevicius et al., 2019), hosted in Pontiac metasedimentary rocks south of the CLLDZ. The ratios of the segment fall into the range of calculated values for the higher-order faults in the Val-d'Or and Malartic districts by Neumayr et al. (2007). The high ratios

computed for the CLLDZ and assigned to Astoria in Neumayr et al. (2007) were based on the Orenada deposit in Val-d'Or, hosted in Pontiac metasedimentary rocks.

The fluid/rock ratios show a progressive decrease of their values towards the less endowed sectors, from an average of 0.80 in Augmitto, 0.75 in Cinderella, 0.85 in Lac Gamble, 0.45 in East-Bay, and 0.48 in Bouzan, excluding the 1.9 outlier in Bouzan. The sample in Bouzan with a ratio of 1.9 can be explained by its more uncommon talc-chlorite alteration, compared to the other samples, and because the $\delta^{18}O_{rock}$ is only 0.2 ‰ higher than the composition of the rock. Even though the values are low, the higher fluid/rock ratios in the endowed sectors reflect higher fluid-rock interactions, which might have been important for gold precipitation, which was not achieved in the East-Bay and Bouzan blocks. Additionally, the fluid/rock ratios indicate a gradual change in the overall integrated fluid flux, suggesting a larger-scale fluid flow structure in endowed sectors, with the hypothesis that the high flow structure continues west of the Augmitto-Bouzan segment study area.

Orogenic gold deposits are usually associated with high fluid fluxes, and thus fluid/rock ratios of at least an order of magnitude higher than at Augmitto-Bouzan (Mikucki & Ridley, 1993; Ridley & Diamond, 2000). The lower ratios presented here could potentially be associated with the fact that the equation used is adapted for water-dominated hydrothermal systems, and the fluids of the study area contained a high proportion of CO_2, as shown by the host rocks containing up to 50 % carbonate minerals (Salmon & McDonough, 2011) and the fluid inclusion data from Neumayr et al. (2007) showing up to 55 mole% CO_2 in veins from Astoria.

1.7.3. Spatial geochemical variations

The Augmitto, Cinderella, and Lac Gamble blocks, characterized by high gold content, display high carbonatization (Fig. 7A) and high local fuchsite molar ratios (Fig. 7C). A lower value for a sample in the Augmitto block and the significant drop of the carbonatization index in Bouzan are related to samples with the talc-chlorite alteration assemblage, compared to the carbonate±fuchsite assemblage of other samples (Fig. 7A-B). In Astoria, a sudden decline of the 3K/(Al+Cr) values occurs between 4900 and 5900 m (Fig. 7C-D). This drop is likely due to late contact metamorphism overprinting the initial hydrothermal alteration assemblage of the Astoria area during intrusion of the Mesoproterozoic dykes, which is also attested by the low whole-rock $\delta^{18}O$ values similar to the metamorphosed tremolite-chlorite schists (Fig. 11A; Appendix B) and the low fluid/rock ratios (Fig. 22).

The variation in alteration intensity does not directly correlate with the chemical composition of carbonate and tourmaline observed between the endowed and less endowed sectors (Fig. 10). Indeed, areas of high saturation indices (Fig. 7) are not directly correlated to the shifts in Fe/Mg in tourmaline and carbonates, implying that another process controlled the chemical composition of the minerals. Similar changes in the Fe/Mg ratio of carbonate and other minerals in veins have been discussed by Ridley and Diamond (2000). They

mentioned Fe/Mg variations along veins and related these Fe/Mg to changes in the fluid composition at a local scale, following the Fe/Mg ratio of the host rocks. However, the Fe/Mg ratios of carbonate and tourmaline of the Augmitto-Bouzan segment are relatively constant in the endowed sectors but increase significantly in the less endowed areas (Fig. 10), hence these are not localized changes. Since protoliths are comparable in nature (Fig. 6A), they likely attest to larger-scale variations of the fluid chemical composition.

Thus, the changes in tourmaline and carbonate chemical compositions seem to point either towards a modification of the fluid's chemistry related to its interaction with rocks during its migration and/or to fluid mixing. This is corroborated by the slightly lower fluid/rock ratios (Fig. 22) and a higher proportion of upper crustal fluids with lower $\delta^{18}O_{H2O}$ in the less endowed sectors (Fig. 17). Vein mineral chemistry between East-Bay and Bouzan has more Fe, Ca, and Mn than elsewhere (Fig. 10; Appendix C-D). This could be related to the proximity of the intermediate to mafic volcanic rocks of the Blake River Group in the less endowed sectors. The increasing Ca content in solution, leached from mafic rock plagioclase could potentially have decreased its Mg/Ca ratio, thus leading to preferential crystallization of calcite instead of ferroan dolomite (Folk & Land, 1975; Machel & Mountjoy, 1986). This would be consistent with the change of the dominant carbonate phase in the less endowed sectors (Fig. 8).

1.7.4. Fluid flow along the Augmitto-Bouzan segment

As previously mentioned, fluid flow, as well as oxygen isotope transport and reaction in fractured geological materials, can be simulated using 3D numerical models by using appropriate boundary conditions and hydraulic properties. The boundary conditions chosen for this study (Fig. 19) were also used in a similar geological context for the numerical model of the Val-d'Or vein field by Beaudoin et al. (2006). The numerical model with corridors of high hydraulic conductivity between the Augmitto and Cinderella zones and at Astoria (Fig. 21) has been designed to replicate the oxygen isotope zonation pattern observed in the field (Fig. 17). The higher conductivity of these corridors is most likely the result of deformation-induced permeability. Deformation events likely developed preferential pathways for infiltration of the deep-seated metamorphic fluid along structural elements such as foliation planes and fractures, which are already recognized to be of major significance for gold exploration across the property (Salmon & McDonough, 2011).

The Augmitto vein stockwork is subparallel with mainly east-west foliation (S_3), particularly toward the eastern end of the block (Wilson, 1962; Rafini, 2014). These structures would create a preferential zone of higher permeability for the rising metamorphic fluid, as modelled at the boundary between the Augmitto and Cinderella areas (Fig. 20, Fig. 21).

In the Astoria block, mineralized veins are subparallel to the main foliation (S_1), as well as stretching lineations and a late foliation associated with D_4 (Kelly, 1988; Gauthier et al., 1990; Neumayr et al., 2007; Rafini,

2014). The veins are thus associated with deformation-related structures that can explain the higher hydraulic conductivity of the area.

Only few structural data are available in East-Bay and Bouzan, making it challenging to compare with the structural information available for the gold-endowed sectors. However, the rocks of this area are less deformed and altered compared to the rocks from Augmitto to Astoria (Wilson, 1962). This is consistent with the lack of preferential deformation-induced pathways for the hydrothermal fluid, thus in agreement with the absence of high conductivity corridors in the 3D model for these two blocks (Fig. 20), as well as with the lower fluid/rock ratios.

The Lac Gamble block is significantly mineralized with a high gold content (Fig. 3), but the lack of quartz-tourmaline data of the block (n=1) does not allow any conclusions regarding the presence of hot metamorphic fluid upwelling (Fig. 17).

The oxygen isotope pattern documented along the Augmitto-Bouzan segment is reproduced over a short period of time, i.e., 10 000 years or less (Fig. 21A-B), after which a steady-state solute transport composition is reached where the composition of fluids in the CLLDZ is dominated by the composition of the deep-seated metamorphic fluid. This interval is consistent with the minimum duration of hydrothermal activity (10 000 years) for the Sigma deposit by Garofalo (2000), as well as the duration (10 to 8,000 years) to form a 5 Moz goldfield by Micklethwaite et al. (2015). Overall, the duration is consistent with the fact that these types of deposits are generally formed by short-lived hydrothermal systems (Beaudoin et al., 2006; Wyman et al., 2016; Herzog et al., 2022).

Compared to the rest of the segment, the proportion of upper crustal fluid is higher in the Piché Group of East-Bay and Bouzan, as shown by the lower $\delta^{18}O_{H2O}$ values measured in the field (Fig. 17) and simulated in the numerical models before 10 000 years (Fig. 19A-B, Fig. 21A-B), which is likely related to changes in fluid flow. These changes could be linked to either the absence of a sedimentary rock package north of the CLLDZ, the decrease in thickness, or the orientation change of the Piché Group (Fig. 18). Fluid flow behavior within the rocks of the Timiskaming and Blake River groups across the CLLDZ is illustrated in two north-south cross-sections in the endowed sectors (Fig. 23B) at X = 1400 m and in the less endowed sectors (Fig. 23C) at X = 10 800 m (Fig. 23). In both endowed and less endowed sectors, flow vectors show that a portion of the pore fluid from surrounding rocks drains into the CLLDZ (Fig. 23). In the gold endowed sectors, the Timiskaming sedimentary rocks north of the Piché Group have a lower porosity of 2.5 % and thus contain a smaller volume of upper crustal fluid. In addition, the wider band of the Piché Group of the area favours the circulation of a larger volume of metamorphic fluids. Mixing of the upper crustal fluid thus has a negligible effect on the composition of the fluid circulating into the CLLDZ, which remains metamorphic-dominated with high $\delta^{18}O_{H2O}$ (Fig. 21, Fig. 23).

The zones of high hydraulic conductivity in Augmitto-Cinderella and Astoria are even less affected by this mixing since they promote even more metamorphic fluid advection (Fig. 21). On the other hand, the Blake River Group north of the Piché Group in the less endowed sectors has a higher porosity (18 %; Table 2) and thus holds a larger volume of pore fluid. Additionally, the decrease in thickness of the Piché Group in these sectors leads to less significant advection of metamorphic fluid into the CLLDZ compared to the endowed sectors. Therefore, the upper crustal fluid is drawn into the CLLDZ in a larger proportion in East-Bay and Bouzan, and the smaller volume of infiltrating metamorphic fluid is more diluted, leading to the modelled (Fig. 19, Fig. 21) and measured (Fig. 17) lower $\delta^{18}O_{H2O}$ values. This model is also consistent with the fluid/rock ratios, where ratios are higher in the endowed sectors, controlled by higher hot metamorphic fluid advection, and lower in East-Bay and Bouzan.

The variation of fluid flow between endowed and less endowed sectors likely explains the differences in gold distribution by considering that gold is likely transported into the deep-seated metamorphic fluid (Fig. 17, Fig. 21; Phillips & Powell, 2010). Indeed, this could explain the relationship between zones of high gold content (Fig. 3) and zones dominated by metamorphic fluids (Fig. 17), which were preferentially focused into the Piché Group through pathways of high hydraulic conductivity. In the less endowed sectors, the lower proportion of gold-bearing metamorphic fluids diluted by upper crustal pore fluids results in lower gold endowment.

The difference in fluid flow between endowed and less endowed sectors is also consistent with the geochemical data of vein carbonate and tourmaline. The preferential enrichment for Fe, Mn, and Ca in the vein minerals of the less endowed sector correlates with the low $\delta^{18}O_{H2O}$ values. These elements could have potentially been transported into the upper crustal fluids originating from the Blake River and incorporated into the Piché Group by leaching of these elements from the andesitic to basaltic rocks of the Blake River Group into pore water (Hood et al., 2019). For minerals sampled within the Augmitto to Astoria areas, their higher Mg and Cr contents could also attest for fluids that percolated almost solely through the ultramafic rocks of the Piché Group, with little to no chemical contribution from other rock packages.

1.7.5. Gold precipitation mechanisms throughout the segment

This study thus demonstrates the most likely phenomenon for the variation of gold content between the endowed and less endowed sectors of the property, but mechanisms related to precipitation of vein minerals along gold decomplexation in the endowed areas remain uncertain. Still, the isotopic composition of the aqueous fluids and fluid/rock ratios can hint at certain phenomena related to such precipitation.

Veins of the Augmitto-Cinderella area with metamorphic-dominant compositions likely precipitated from fluid-rock interactions, which might have changed the redox state of the fluid since the low δD_{H2O} values do not seem to corroborate for phase separation, and the high $\delta^{18}O_{H2O}$ and temperature values do not point toward fluid mixing (Fig. 16; Table 1). This is consistent with the fact that the Augmitto and Cinderella blocks have the highest

fluid/rock ratios of the segment (Fig. 22). The upwelling of metamorphic fluid in Astoria is most likely controlled by phase separation, caused by flash vaporization and condensation, according to the high δD_{H2O} (> 0 ‰) and high $\delta^{18}O_{H2O}$ (> 8.5 ‰; Fig. 16; Table 1). Elsewhere in the endowed sectors, vein mineral and gold precipitation might have been caused by either fluid-rock interactions, fluid mixing, phase separation, or a combination of these mechanisms. Vein mineral precipitation in the East-Bay and Bouzan blocks was likely dominated by fluid mixing, as shown by the low temperature and $\delta^{18}O_{H2O}$ fluids, which might have caused a change in the fluids' thermochemistry.

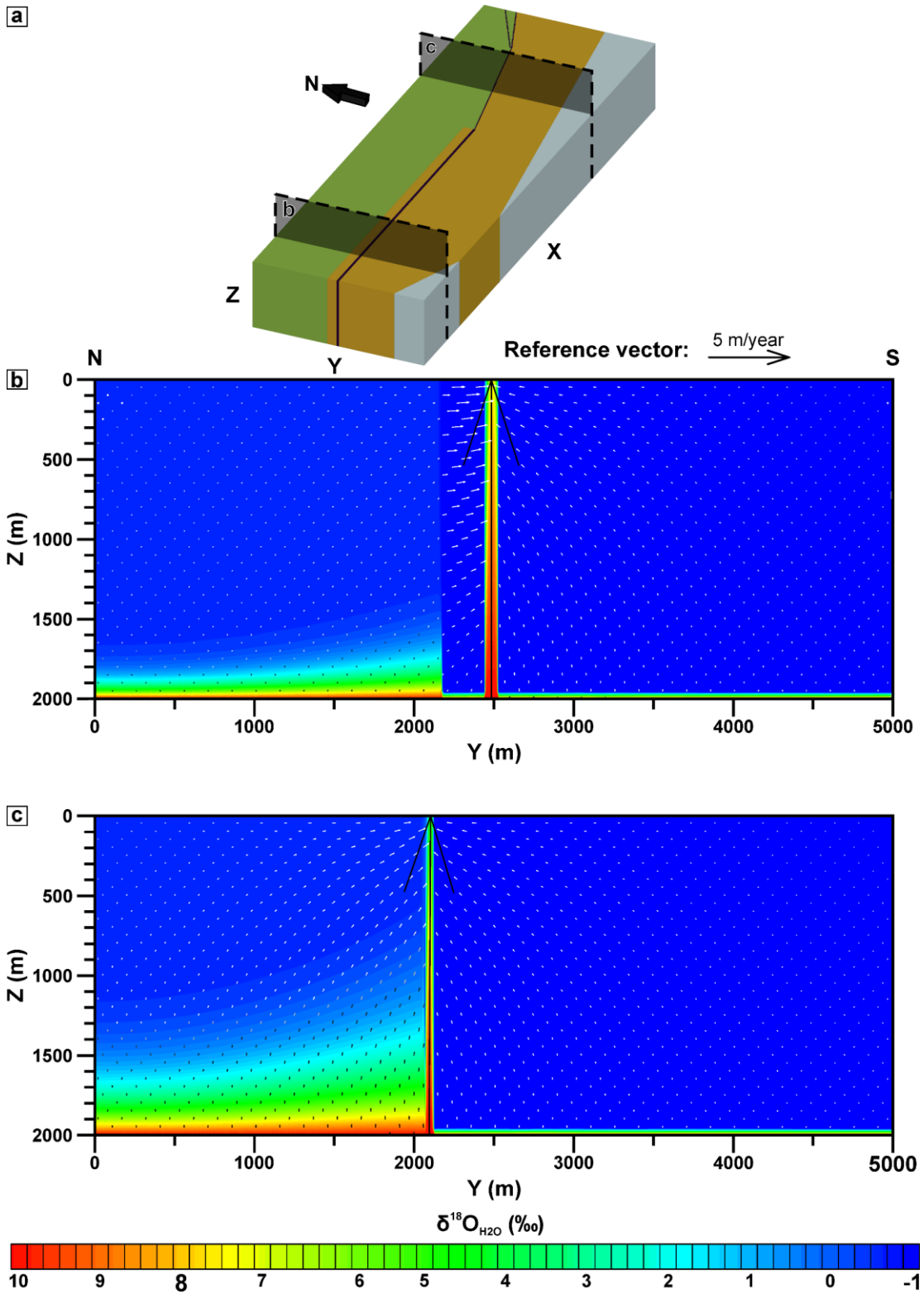

Figure 23 a Block model of Figure 18 with two cross-sections looking east from scenario of Figure 21, after 10 000 years (Fig. 19B) at **b** X = 1400 m and **c** X = 10 800 m. Velocity vectors are displayed and give the direction of fluid flow. Their sizes are proportionate to the velocity of the fluid, except for the vector in the Piché Group, which has been reduced by half for better visual representation.

1.8 Conclusions

A multi-method approach combining petrography, stable isotope analyses, spatial variations, and 3D fluid flow modelling on a segment of the CLLDZ with irregularly distributed gold mineralization allowed the characterization of fluid sources and fluid-rock interactions responsible for the heterogeneous deposition of orogenic gold mineralization. The study suggests mixing between a gold-bearing deep-seated metamorphic fluid characterized by a high $\delta^{18}O$ (> 10.8 ‰), low δD (< –29 ‰) and high temperature (> 420 °C), and an upper crustal pore fluid with low $\delta^{18}O$ (< 4 ‰), a δD around 0 ‰ and low temperature (< 230 °C). These end-members have likely been affected by multiple flash vaporization and condensation cycles due to pressure fluctuations within the hydrothermal system, which led to high δD (≤ 43 ‰). The $\delta^{13}C$ composition of carbonate minerals (–6.2- –2.8 ‰) is also consistent with a metamorphic origin of the CO_2 source.

A vertical thermal gradient of ~ 32 °C per 100 m is identified within the Piché Group rocks in the gold-endowed sectors. Areas dominated by advection of high $\delta^{18}O_{H2O}$ fluids in the Augmitto-Cinderella and Astoria blocks were presumably facilitated through local zones of higher permeability. Sectors of poor gold endowment, the East-Bay and Bouzan blocks, are characterized by lower $\delta^{18}O_{H2O}$, interpreted as a higher proportion of upper crustal fluid within the fault zone. This likely resulted from both 1) the decrease in thickness of the Piché Group rocks in the area, which promotes a lower volume of metamorphic fluids, and 2) more porous volcanic rocks north of the fault, which contribute to a greater proportion of pore water in the CLLDZ, compared to sedimentary rocks in the gold endowed sectors. This incorporation of upper crustal pore fluid from the Blake River Group could also be consistent with the progressive increase of Fe, Ca, and Mn content in vein minerals in the less endowed sectors.

The study area is characterized by relatively low fluid/rock ratios, progressively decreasing towards the less gold endowed East-Bay and Bouzan blocks. This is consistent with a larger advection of gold-bearing high-temperature, metamorphic-dominated fluid in the endowed sectors compared to the less endowed sectors.

This study suggests that variations of gold endowment between sectors could have been controlled by changes in fluid flow where gold is associated with a higher flow of gold-bearing metamorphic fluid which can be spatially controlled by preferential structures which enhance the fault's permeability. The study also suggests that the greater the involvement of the upper crust in a hydrothermal system, the more diluted and uneconomic it becomes and could potentially be associated with geochemical changes in the mineral phases.

1.9 Acknowledgments

This project is a part of the Masters of Science (MSc) thesis of Guillaume Raymond. The project is part of the Metal Earth program, funded by the Canada First Research Excellence Fund. We are grateful for the collaboration with Yorbeau Resources Inc., which facilitated access to material, data, and core samples. Special thanks to Baptiste Chapon and Sylvain Lépine for their continued support and insights, on and off the field. We acknowledge Jean-Philippe Séguin and Isaac Siles Malta for their assistance throughout the fieldwork. We thank Taus R. C. Jørgensen (Laurentian University) for his early guidance on the project and his introduction to the geology of the area.

Conclusions et recommandations

Une approche multiméthodes combinant pétrographie, analyses d'isotopes stables, variations spatiales et modélisation de l'écoulement des fluides en 3D sur un gisement avec une minéralisation aurifère irrégulière le long de la zone de déformation Cadillac Larder-Lake a permis de caractériser les sources des fluides et les interactions fluide-roche responsables de la distribution hétérogène de la minéralisation. L'étude suggère un mélange entre un fluide métamorphique aurifère profond caractérisé par un $\delta^{18}O$ élevé (> 10.8 ‰), un faible δD (< –29 ‰) et de hautes températures (> 420 °C) et un fluide poral de la croûte supérieure avec un faible $\delta^{18}O$ (< 4 ‰), un δD autour de 0 ‰ et de basses températures (< 230 °C). Ces pôles ont probablement été affectés par plusieurs cycles d'ébullition et de condensation dus à d'importantes fluctuations de pression au sein du système hydrothermal, ce qui a conduit aux valeurs de δD élevées (≤ 43 ‰). La composition en $\delta^{13}C$ des minéraux carbonatés (–6.2- –2.8 ‰) tend également vers une origine métamorphique de la source de CO_2.

Un important gradient thermique vertical d'environ 32 °C par 100 m est identifié au sein des roches du Groupe de Piché, sans doute un résultat du mélange progressif du fluide profond chaud avec le fluide supracrustal de plus basse température. Des remontées de fluide avec des valeurs élevées de $\delta^{18}O_{H2O}$ sont observées dans les blocs d'Augmitto-Cinderella et d'Astoria, où l'écoulement des fluides métamorphiques a vraisemblablement été facilité par des zones locales de perméabilité plus élevée. Les secteurs relativement pauvres en or, les blocs East-Bay et Bouzan, sont caractérisés par des $\delta^{18}O_{H2O}$ plus bas, interprétés comme étant dus à une proportion plus importante de fluide interstitiel de la croûte supérieure au sein de la zone de faille. Ceci est probablement associé à 1) la diminution de l'épaisseur du Groupe de Piché dans la région, favorisant un écoulement de fluide métamorphique moins volumineux vers la surface et 2) la présence de roches volcaniques plus poreuses au nord de la faille, venant incorporer un plus grand volume d'eau porale dans celle-ci par rapport aux roches sédimentaires dans les secteurs aurifères. Cette incorporation de fluide interstitiel provenant du Groupe de Blake River pourrait également être cohérente avec l'augmentation progressive du Fe, Ca et Mn des minéraux de veines des secteurs peu minéralisés, ainsi qu'avec le changement de la phase carbonatée dominante passant de la Fe-dolomite à la calcite.

Le terrain d'étude est caractérisé par des rapports fluide/roche relativement bas, qui diminuent progressivement vers les blocs East-Bay et Bouzan. Cette observation est cohérente avec un flux plus important de fluides métamorphiques de haute température dans les secteurs minéralisés et un flux plus faible de fluides mixtes de basse température dans les secteurs peu minéralisés.

Cette étude démontre donc que les variations de dotation en or entre les secteurs sont essentiellement contrôlées par des changements dans l'écoulement des fluides où l'or est associé à un écoulement plus

important de fluide métamorphique, pouvant être contrôlé spatialement par des structures préférentielles qui augmentent la perméabilité de la faille. L'étude suggère également que plus l'implication de fluide interstitiel de la croûte supérieure est importante dans un système hydrothermal, plus son contenu aurifère est dilué et peu rentable, ce qui pourrait être associé à des changements de composition chimique des phases minérales.

Le projet s'est penché sur l'étude du système hydrothermal passé, par l'entremise des minéraux filoniens, pour expliquer les différences de dotation d'or dans la propriété. Cependant, les phénomènes responsables de la précipitation de l'or à travers le segment demeurent relativement incertains. Comme travaux futurs, il serait intéressant de comparer des forages minéralisés et non minéralisés entre Augmitto et Astoria, comme nous n'avons pas noté de changements importants dans la composition des fluides. Il serait judicieux d'aller inspecter à l'échelle micro à nanoscopique les changements géochimiques au niveau des minéraux associés à l'or (e.g., pyrite, arsenopyrite), pouvant témoigner de l'état passé des fluides. Par exemple, une étude in situ des isotopes du soufre ($\delta^{34}S$ et $\Delta^{33}S$) sur les sulfures pourrait être intéressante pour observer des variations de l'état d'oxydation des fluides. De plus, une étude des inclusions fluides pourrait être bénéfique afin de dénoter concrètement les changements de phase des fluides liés aux fluctuations de pression, comme nous avons interprété au niveau des isotopes d'hydrogène dans ce travail, et comparer les différentes compositions des fluides entre les zones minéralisées et non minéralisées.

References

Ayer, J., Amelin, Y., Corfu, F., Kamo, S., Ketchum, J., Kwok, K., & Trowell, N. (2002). Evolution of the southern Abitibi greenstone belt based on U–Pb geochronology: autochthonous volcanic construction followed by plutonism, regional deformation and sedimentation. *Precambrian Research, 115*(1-4), 63-95.

Badertscher, N. P., Beaudoin, G., Therrien, R., & Burkhard, M. (2002). Glarus overthrust: A major pathway for the escape of fluids out of the Alpine orogen. *Geology, 30*(10), 875-878.

Banerjee, K., Basu, A., Guin, R., & Sengupta, D. (2011). Radon (222Rn) level variations on a regional scale from the Singhbhum Shear Zone, India: A comparative evaluation between influence of basement U-activity and porosity. *Radiation Physics and Chemistry, 80*(5), 614-619.

Bateman, R., & Hagemann, S. (2004). Gold mineralisation throughout about 45 Ma of Archaean orogenesis: protracted flux of gold in the Golden Mile, Yilgarn craton, Western Australia. *Mineralium Deposita, 39*(5), 536-559.

Bath, A. B., Walshe, J. L., Cloutier, J., Verrall, M., Cleverley, J. S., Pownceby, M. I., . . . Nortje, G. S. (2013). Biotite and apatite as tools for tracking pathways of oxidized fluids in the Archean East Repulse gold deposit, Australia. *Economic Geology, 108*(4), 667-690.

Beaudoin, G., & Chiaradia, M. (2016). Fluidmixing in orogenic gold deposits: Evidence from the H-O-Sr isotope composition of the Val-d'Or vein field (Abitibi, Canada). *Chemical Geology, 437*, 7-18. doi:10.1016/j.chemgeo.2016.05.009

Beaudoin, G., Mercier-Langevin, P., Dubé, B., & Taylor, B. E. (2014). Low-temperature alteration at the world-class LaRonde Penna Archean Au-rich volcanogenic massive sulfide deposit, Abitibi subprovince, Quebec, Canada: evidence from whole-rock oxygen isotopes. *Economic Geology, 109*(1), 167-182.

Beaudoin, G., & Pitre, D. (2005). Stable isotope geochemistry of the Archean Val-d'Or (Canada) orogenic gold vein field. *Mineralium Deposita, 40*(1), 59-75. doi:10.1007/s00126-005-0474-z

Beaudoin, G., & Therrien, R. (1999). Sources and drains: Major controls of hydrothermal fluid flow in the Kokanee Range, British Columbia, Canada. *Geology, 27*(10), 883-886.

Beaudoin, G., Therrien, R., & Savard, C. (2006). 3D numerical modelling of fluid flow in the Val-d'Or orogenic gold district: major crustal shear zones drain fluids from overpressured vein fields. *Mineralium Deposita, 41*(1), 82-98. doi:10.1007/s00126-005-0043-5

Bédard, L. P., & Ludden, J. N. (1997). Nd-isotope evolution of Archaean plutonic rocks in southeastern Superior Province. *Canadian Journal of Earth Sciences, 34*(3), 286-298.

Bedeaux, P., Mathieu, L., Pilote, P., Rafini, S., & Daigneault, R. (2018). Origin of the Piche Structural Complex and implications for the early evolution of the Archean crustal-scale Cadillac Larder Lake Fault Zone, Canada. *Canadian Journal of Earth Sciences, 55*(8), 905-922. doi:10.1139/cjes-2017-0270

Bedeaux, P., Pilote, P., Daigneault, R., & Rafini, S. (2017). Synthesis of the structural evolution and associated gold mineralization of the Cadillac Fault, Abitibi, Canada. *Ore Geology Reviews, 82*, 49-69. doi:10.1016/j.oregeorev.2016.11.029

Benn, K., Miles, W., Ghassemi, M. R., & Gillett, J. (1994). Crustal structure and kinematic framework of the northwestern Pontiac Subprovince, Quebec: an integrated structural and geophysical study. *Canadian Journal of Earth Sciences, 31*(2), 271-281.

Bohlke, J. K. (1982). Orogenic (metamorphic-hosted) gold-quartz veins. *US Geological Survey Open-File Report, 795*, 70-76.

Boiron, M.-C., Cathelineau, M., Banks, D. A., Fourcade, S., & Vallance, J. (2003). Mixing of metamorphic and surficial fluids during the uplift of the Hercynian upper crust: consequences for gold deposition. *Chemical Geology, 194*(1-3), 119-141.

Born, P. (1996). *A sedimentary basin analysis of the Abitibi Greenstone belt in the Timmins area, northern Ontario, Canada.* Carleton University,

Börner, J. H., Girault, F., Bhattarai, M., Adhikari, L. B., Deldicque, D., Perrier, F., & Spitzer, K. (2018). Anomalous complex electrical conductivity of a graphitic black schist from the Himalayas of central Nepal. *Geophysical Research Letters, 45*(9), 3984-3993.

Calvert, A., & Ludden, J. (1999). Archean continental assembly in the southeastern Superior Province of Canada. *Tectonics, 18*(3), 412-429.

Card, K. (1990). A review of the Superior Province of the Canadian Shield, a product of Archean accretion. *Precambrian Research, 48*(1-2), 99-156.

Chapon, B., Hallé, L., & Carignan, G. (2013). *Géologie des minéralisations aurifères du segment Augmitto-Astoria, Secteur de Rouyn-Noranda.* Paper presented at the Exploabitibi-2013, Val-d'Or.

Clayton, R. N., & Mayeda, T. K. (1963). The use of bromine pentafluoride in the extraction of oxygen from oxides and silicates for isotopic analysis. *Geochimica Et Cosmochimica Acta, 27*(1), 43-52.

Cole, D. R., Ohmoto, H., & Jacobs, G. K. (1992). Isotopic exchange in mineral-fluid systems: III. Rates and mechanisms of oxygen isotope exchange in the system granite-H2O±NaCl±KCl at hydrothermal conditions. *Geochimica Et Cosmochimica Acta, 56*(1), 445-466.

Corfu, F. (1993). The evolution of the southern Abitibi greenstone belt in light of precise U-Pb geochronology. *Economic Geology, 88*(6), 1323-1340.

Corfu, F., Krogh, T., Kwok, Y., & Jensen, L. (1989). U–Pb zircon geochronology in the southwestern Abitibi greenstone belt, Superior Province. *Canadian Journal of Earth Sciences, 26*(9), 1747-1763.

Cox, K., Bell, J., & Pankhurst, R. (1979). The interpretation of data for plutonic rocks. In K. G. Cox, J. D. Bell, & R. J. Pankhurst (Eds.), *The Interpretation of Igneous Rocks* (pp. 308-331). Dordrecht: Springer Netherlands.

Croghan, C., & Egeghy, P. P. (2003). Methods of dealing with values below the limit of detection using SAS. *Southern SAS User Group, 22*, 24.

Daigneault, R., Mueller, W., & Chown, E. (2002). Oblique Archean subduction: accretion and exhumation of an oceanic arc during dextral transpression, Southern Volcanic Zone, Abitibi Subprovince Canada. *Precambrian Research, 115*(1-4), 261-290.

Daver, L., Jébrak, M., Beaudoin, G., & Trumbull, R. B. (2020). Three-stage formation of greenstone-hosted orogenic gold deposits in the Val-d'Or mining district, Abitibi, Canada: Evidence from pyrite and tourmaline. *Ore Geology Reviews, 120*, 103449.

David, J., Dion, C., Goutier, J., Roy, P., Bandyayera, D., Legault, M., & Rhéaume, P. (2006). Datations U-Pb effectuées dans la Sous-province de l'Abitibi à la suite des travaux de 2004-2005. *Ministère des Ressources naturelles et de la Faune, Québec*(2006-04), 22.

David, J., Pilote, P., Hammouche, H., Leclerc, F., & Takam, F. T. (2018). *Datations U-Pb dans la province du Supérieur effectuées au GEOTOP en 2013-2014*: Géologie Québec.

Davis, D. W. (2002). U–Pb geochronology of Archean metasedimentary rocks in the Pontiac and Abitibi subprovinces, Quebec, constraints on timing, provenance and regional tectonics. *Precambrian Research, 115*(1-4), 97-117.

Dimroth, E., Imreh, L., Rocheleau, M., & Goulet, N. (1982). Evolution of the south-central part of the Archean Abitibi belt, Quebec. Part I: Stratigraphy and paleogeographic model. *Canadian Journal of Earth Sciences, 19*(9), 1729-1758.

Domenico, P. A., & Schwartz, F. W. (1998). *Physical and Chemical Hydrogeology* (Vol. 506): Wiley New York.

Dubé, B., & Gosselin, P. (2007). Greenstone-hosted quartz-carbonate vein deposits. In W. D. Goodfellow (Ed.), *Mineral Deposits of Canada: A Synthesis of Major Deposit-Types, District Metallogeny, the Evolution of Geological Provinces and Exploration Methods* (Vol. 5, pp. 49-73): Geological Association of Canada, Mineral Deposit Division.

Dubé, B., & Mercier-Langevin, P. (2020). Chapter 32: Gold Deposits of the Archean Abitibi Greenstone Belt, Canada. In R. H. Sillitoe, R. J. Goldfarb, F. Robert, & S. F. Simmons (Eds.), *Geology of the World's Major Gold Deposits and Provinces* (Vol. 23, pp. 0): Society of Economic Geologists.

Eiler, J. M. (2001). Oxygen isotope variations of basaltic lavas and upper mantle rocks. *Reviews in Mineralogy and Geochemistry, 43*(1), 319-364.

Eisenlohr, B., Groves, D., & Partington, G. (1989). Crustal-scale shear zones and their significance to Archaean gold mineralization in Western Australia. *Mineralium Deposita, 24*(1), 1-8.

Enrique, P., & Esteve, S. (2019). A chemical approximation to the modal QAPF and normative Q'(F')-ANOR classification of the igneous rocks based on their SiO2-CaO-K2O content. *Geogaceta, 2019, vol. 66, p. 91-94*.

Evans, K., Phillips, G., & Powell, R. (2006). Rock-buffering of auriferous fluids in altered rocks associated with the Golden Mile-style mineralization, Kalgoorlie gold field, Western Australia. *Economic Geology, 101*(4), 805-817.

Folk, R. L., & Land, L. S. (1975). Mg/Ca ratio and salinity: two controls over crystallization of dolomite. *AAPG Bulletin, 59*(1), 60-68.

Fougerouse, D., Micklethwaite, S., Tomkins, A. G., Mei, Y., Kilburn, M., Guagliardo, P., . . . Howard, D. L. (2016). Gold remobilisation and formation of high grade ore shoots driven by dissolution-reprecipitation replacement and Ni substitution into auriferous arsenopyrite. *Geochimica Et Cosmochimica Acta, 178*, 143-159. doi:10.1016/j.gca.2016.01.040

Frieman, B. M. (2018). *U-Pb and Lu-Hf LA-ICP-MS detrital zircon and structural investigations in the Abitibi subprovince, Canada, with implications for Archean geodynamic processes and deformation behavior along gold-bearing, crustal-scale faults.* (Doctor of Philosophy (Geology) Doctoral thesis). Colorado School of Mines. Arthur Lakes Library, Colorado, United-States.

Furnes, H., de Wit, M., Staudigel, H., Rosing, M., & Muehlenbachs, K. (2007). A vestige of Earth's oldest ophiolite. *Science, 315*(5819), 1704-1707.

Gaboury, D. (2019). Parameters for the formation of orogenic gold deposits. *Applied Earth Science, 128*(3), 124-133.

Gao, Y., Hoefs, J., Przybilla, R., & Snow, J. E. (2006). A complete oxygen isotope profile through the lower oceanic crust, ODP Hole 735B. *Chemical Geology, 233*(3-4), 217-234.

Garofalo, P. S. (2000). *Gold precipitation and hydrothermal alteration during fluid flow through the vein network of the mesothermal gold deposit of Sigma,(Abitibi belt, Canada).* ETH Zurich,

Gauthier, N., Rocheleau, M., Kelly, D., & Gagnon, Y. (1990). Controls on the distribution of gold mineralization within the Cadillac tectonic zone, Rouyn-Beauchastel segment, Abitibi Belt, Quebec. In M. Rive, Y. Verpaelst, Y. Gagnon, J. M. Lulin, R. G, & A. Simard (Eds.), *La ceinture polymétallique du Nord-Ouest Québécois* (Vol. 43, pp. 185-198): L'institut canadien des mines et de la métallurgie.

Goldfarb, R. J., Baker, T., Dubé, B., Groves, D. I., Hart, C. J. R., Gosselin, P., . . . Richards, J. P. (2005). Distribution, Character, and Genesis of Gold Deposits in Metamorphic Terran. In *One Hundredth Anniversary Volume* (pp. 0): Society of Economic Geologists.

Goldfarb, R. J., & Groves, D. I. (2015). Orogenic gold: Common or evolving fluid and metal sources through time. *Lithos, 233*, 2-26. doi:10.1016/j.lithos.2015.07.011

Groves, D. I., Goldfarb, R. J., Gebre-Mariam, M., Hagemann, S. G., & Robert, F. (1998). Orogenic gold deposits: a proposed classification in the context of their crustal distribution and relationship to other gold deposit types. *Ore Geology Reviews, 13*(1-5), 7-27.

Groves, D. I., Santosh, M., Deng, J., Wang, Q., Yang, L., & Zhang, L. (2020a). A holistic model for the origin of orogenic gold deposits and its implications for exploration. *Mineralium Deposita, 55*(2), 275-292.

Groves, D. I., Santosh, M., & Zhang, L. (2020b). A scale-integrated exploration model for orogenic gold deposits based on a mineral system approach. *Geoscience Frontiers, 11*(3), 719-738.

Gruau, G., Tourpin, S., Fourcade, S., & Blais, S. (1992). Loss of isotopic (Nd, O) and chemical (REE) memory during metamorphism of komatiites: new evidence from eastern Finland. *Contributions to Mineralogy and Petrology, 112*(1), 66-82.

Heap, M., Farquharson, J., Baud, P., Lavallée, Y., & Reuschlé, T. (2015). Fracture and compaction of andesite in a volcanic edifice. *Bulletin of Volcanology, 77*(6), 1-19.

Heap, M. J., & Kennedy, B. M. (2016). Exploring the scale-dependent permeability of fractured andesite. *Earth and Planetary Science Letters, 447*, 139-150.

Henry, D. J., Novák, M., Hawthorne, F. C., Ertl, A., Dutrow, B. L., Uher, P., & Pezzotta, F. (2011). Nomenclature of the tourmaline-supergroup minerals. *American Mineralogist, 96*(5-6), 895-913.

Herzog, M., LaFlamme, C., Beaudoin, G., Marsh, J., & Guilmette, C. (2022). U–Pb vein xenotime geochronology constraints on timing and longevity of orogenic gold mineralization in the Malartic-Val-d'Or Camp, Abitibi Subprovince, Canada. *Mineralium Deposita*, 1-29.

Hodkiewicz, P. F., Groves, D. I., Davidson, G. J., Weinberg, R. F., & Hagemann, S. G. (2009). Influence of structural setting on sulphur isotopes in Archean orogenic gold deposits, Eastern Goldfields Province, Yilgarn, Western Australia. *Mineralium Deposita, 44*(2), 129-150. doi:10.1007/s00126-008-0211-5

Hood, S. B., Cracknell, M. J., Gazley, M. F., & Reading, A. M. (2019). Element mobility and spatial zonation associated with the Archean Hamlet orogenic Au deposit, Western Australia: Implications for fluid pathways in shear zones. *Chemical Geology, 514*, 10-26.

Hyde, R. S. (1980). Sedimentary facies in the Archean Timiskaming Group and their tectonic implications, Abitibi greenstone belt, northeastern Ontario, Canada. *Precambrian Research, 12*(1-4), 161-195.

Jébrak, M., & Marcoux, É. (2008). *Géologie des ressources minérales*: Ministère des ressources naturelles et de la faune.

Jensen, L. (1976). *A new cation plot for classifying subalkalic volcanic rocks* (Vol. 66): Ontario Division of Mines, Miscellaneous Paper.

Jiang, S.-Y., Palmer, M. R., & Yeats, C. J. (2002). Chemical and boron isotopic compositions of tourmaline from the Archean Big Bell and Mount Gibson gold deposits, Murchison Province, Yilgarn craton, Western Australia. *Chemical Geology, 188*(3-4), 229-247.

Kalamarides, R. I. (1984). Kiglapait geochemistry VI: Oxygen isotopes. *Geochimica Et Cosmochimica Acta, 48*(9), 1827-1836.

Kelly, D. (1988). Recent developments in Yorbeau's Astoria Property Rouyn-Noranda area, Quebec. *Gold Mining, 88*, 468-481.

Kerrich, R., & Fryer, B. (1979). Archaean precious-metal hydrothermal systems, Dome Mine, Abitibi Greenstone Belt. II. REE and oxygen isotope relations. *Canadian Journal of Earth Sciences, 16*(3), 440-458.

Kerrich, R., & Fyfe, W. (1981). The gold—carbonate association: source of CO2, and CO2 fixation reactions in Archaean lode deposits. *Chemical Geology, 33*(1-4), 265-294.

Kerrich, R., Polat, A., Wyman, D., & Hollings, P. (1999). Trace element systematics of Mg-, to Fe-tholeiitic basalt suites of the Superior Province: implications for Archean mantle reservoirs and greenstone belt genesis. *Lithos, 46*(1), 163-187.

Kishida, A., & Kerrich, R. (1987). Hydrothermal alteration zoning and gold concentration at the Kerr-Addison Archean lode gold deposit, Kirkland Lake, Ontario. *Economic Geology, 82*(3), 649-690. doi:10.2113/gsecongeo.82.3.649

Kontak, D. J., & Kerrich, R. (1997). An isotopic (C, O, Sr) study of vein gold deposits in the Meguma Terrane, Nova Scotia; implication for source reservoirs. *Economic Geology, 92*(2), 161-180.

Kotzer, T., Kyser, T., King, R., & Kerrich, R. (1993). An empirical oxygen-and hydrogen-isotope geothermometer for quartz-tourmaline and tourmaline-water. *Geochimica Et Cosmochimica Acta, 57*(14), 3421-3426.

Kuang, X., Jiao, J. J., Zheng, C., Cherry, J. A., & Li, H. (2020). A review of specific storage in aquifers. *Journal of Hydrology, 581*, 124383.

Kyser, T. K., O'Hanley, D. S., & Wicks, F. J. (1999). The origin of fluids associated with serpentinization; evidence from stable-isotope compositions. *The Canadian Mineralogist, 37*(1), 223-237.

LaFlamme, C., Sugiono, D., Thebaud, N., Caruso, S., Fiorentini, M., Selvaraja, V., . . . Martin, L. (2018). Multiple sulfur isotopes monitor fluid evolution of an Archean orogenic gold deposit. *Geochimica Et Cosmochimica Acta, 222*, 436-446. doi:10.1016/j.gca.2017.11.003

Lafrance, B. (2005). *Nouvelles datations isotopiques dans la portion québécoise du Groupe de Blake River et des unités adjacentes*. Québec, Canada: [Charlesbourg]: Ressources naturelles et Faune, Québec.

Lafrance, B. (2015). Geology of the orogenic Cheminis gold deposit along the Larder Lake - Cadillac deformation zone, Ontario. *Canadian Journal of Earth Sciences, 52*(12), 1093-1108. doi:10.1139/cjes-2015-0067

Lahaye, Y., & Arndt, N. (1996). Alteration of a komatiite flow from Alexo, Ontario, Canada. *Journal of Petrology, 37*(6), 1261-1284.

Laporte, J. (2016). *Mineralogical study of the auriferous shear zone along the Augmitto-Astoria segment in the Cadillac break south to Rouyn-Noranda, Abitibi, Quebec.* (Master's thesis). Université du Québec à Montréal, Montreal (Québec, Canada). Retrieved from http://archipel.uqam.ca/id/eprint/8699

Loucks, R. R., & Mavrogenes, J. A. (1999). Gold solubility in supercritical hydrothermal brines measured in synthetic fluid inclusions. *Science, 284*(5423), 2159-2163.

Machel, H.-G., & Mountjoy, E. W. (1986). Chemistry and environments of dolomitization—a reappraisal. *Earth-Science Reviews, 23*(3), 175-222.

Madu, B. E., Nesbitt, B. E., & Muehlenbachs, K. (1990). A mesothermal gold-stibnite-quartz vein occurrence in the Canadian Cordillera. *Economic Geology, 85*(6), 1260-1268.

Martin, H. (1993). The mechanisms of petrogenesis of the Archaean continental crust—comparison with modern processes. *Lithos, 30*(3-4), 373-388.

Matsuhisa, Y., Goldsmith, J. R., & Clayton, R. N. (1979). Oxygen isotopic fractionation in the system quartz-albite-anorthite-water. *Geochimica Et Cosmochimica Acta, 43*(7), 1131-1140. doi:10.1016/0016-7037(79)90099-1

McCuaig, C., & Kerrich, R. (1998). P-T-t-deformation-fluid characteristics of lode gold deposits: evidence from alteration systematics. *Ore Geology Reviews, 12*, 381-453.

McNicoll, V., Goutier, J., Dubé, B., Mercier-Langevin, P., Ross, P.-S., Dion, C., . . . Gibson, H. (2014). U-Pb geochronology of the Blake River Group, Abitibi greenstone belt, Quebec, and implications for base metal exploration. *Economic Geology, 109*(1), 27-59.

Meng, Y.-M., Jébrak, M., Sasseville, C., & Huang, X.-W. (2020). Geochemical and mineralogical diagnosis on gold ores: A case study from the Cadillac–Larder Lake Fault Zone, Abitibi, Canada. *Ore Geology Reviews, 127*, 103840.

Micklethwaite, S., Ford, A., Witt, W., & Sheldon, H. A. (2015). The where and how of faults, fluids and permeability–insights from fault stepovers, scaling properties and gold mineralisation. *Geofluids, 15*(1-2), 240-251.

Middlemost, E. A. (1994). Naming materials in the magma/igneous rock system. *Earth-Science Reviews, 37*(3-4), 215-224.

Mielke, P., Weinert, S., Bignall, G., & Sass, I. (2016). Thermo-physical rock properties of greywacke basement rock and intrusive lavas from the Taupo Volcanic Zone, New Zealand. *Journal of Volcanology and Geothermal Research, 324*, 179-189.

Mikucki, E., & Heinrich, C. (1993). *Vein-and mine-scale wall-rock alteration and gold mineralisation in the Archaean Mount Charlotte deposit, Kalgoorlie, Western Australia.* Paper presented at the Vein-and mine-scale wall-rock alteration and gold mineralisation in the Archaean Mount Charlotte deposit, Kalgoorlie, Western Australia.

Mikucki, E., & Ridley, J. (1993). The hydrothermal fluid of Archaean lode-gold deposits at different metamorphic grades: compositional constraints from ore and wallrock alteration assemblages. *Mineralium Deposita, 28*(6), 469-481.

Ministère des Ressources Naturelles Géologie Québec, M. (2021). Geological Map of Quebec – 2021 Edition. *Système d'information géominière of Québec (SIGEOM).* Retrieved from https://sigeom.mines.gouv.qc.ca/signet/classes/I1108_afchCarteIntr

Monecke, T., Mercier-Langevin, P., Dubé, B., & Frieman, B. (2017). *Archean base and precious metal deposits, southern Abitibi greenstone belt, Canada*: Society of Economic Geologists, Incorporated.

Montsion, R., Thurston, P., & Ayer, J. (Cartographer). (2018). 1:2 000 000 Scale Geological Compilation of the Superior Craton

Mortensen, J. (1993). U–Pb geochronology of the eastern Abitibi Subprovince. Part 2: Noranda–Kirkland Lake area. *Canadian Journal of Earth Sciences, 30*(1), 29-41.

Mueller, W., & Donaldson, J. (1992). Development of sedimentary basins in the Archean Abitibi belt, Canada: an overview. *Canadian Journal of Earth Sciences, 29*(10), 2249-2265.

Mueller, W., Donaldson, J., Dufresne, D., & Rocheleau, M. (1991). The Duparquet Formation: sedimentation in a late Archean successor basin, Abitibi greenstone belt, Quebec, Canada. *Canadian Journal of Earth Sciences, 28*(9), 1394-1406.

Neumayr, P., Hagemann, S., & Couture, J.-F. (2000). Structural setting, textures, and timing of hydrothermal vein systems in the Val d'Or camp, Abitibi, Canada: implications for the evolution of transcrustal, second-and third-order fault zones and gold mineralization. *Canadian Journal of Earth Sciences, 37*(1), 95-114.

Neumayr, P., & Hagemann, S. G. (2002). Hydrothermal fluid evolution within the Cadillac tectonic zone, Abitibi greenstone belt, Canada: Relationship to auriferous fluids in adjacent second- and third-order shear zones. *Economic Geology and the Bulletin of the Society of Economic Geologists, 97*(6), 1203-1225. doi:10.2113/97.6.1203

Neumayr, P., Hagemann, S. G., Banks, D. A., Yardley, B. W. D., Couture, J. F., Landis, G. P., & Rye, R. (2007). Fluid chemistry and evolution of hydrothermal fluids in an Archaean transcrustal fault zone network: the case of

the Cadillac Tectonic Zone, Abitibi greenstone belt, Canada. *Canadian Journal of Earth Sciences, 44*(6), 745-773. doi:10.1139/e06-130

Neumayr, P., Walshe, J., Hagemann, S., Petersen, K., Roache, A., Frikken, P., . . . Halley, S. (2008). Oxidized and reduced mineral assemblages in greenstone belt rocks of the St. Ives gold camp, Western Australia: vectors to high-grade ore bodies in Archaean gold deposits? *Mineralium Deposita, 43*(3), 363-371.

Nicoli, G., Moyen, J.-F., & Stevens, G. (2016). Diversity of burial rates in convergent settings decreased as Earth aged. *Scientific Reports, 6*(1), 1-10.

Oberthuer, T., Mumm, A. S., Vetter, U., Simon, K., & Amanor, J. A. (1996). Gold mineralization in the Ashanti Belt of Ghana; genetic constraints of the stable isotope geochemistry. *Economic Geology, 91*(2), 289-301.

Ohmoto, H. (1986). Stable isotope geochemistry of ore deposit. . In J. W. Valley, H. P. J. Taylor, & J. R. O'Neil (Eds.), *Stable Isotopes in High Temperature Geological Processes*

(Vol. 16, pp. 491-559): Reviews in Mineralogy and Geochemistry.

Ohmoto, H., & Rye, R. O. (1979). Isotopes of sulfur and carbon. In H. L. Barnes (Ed.), *Geochemistry of hydrothermal ore deposits* (pp. 509-567): John Wiley & Sons.

Olivo, G. R., Chang, F., & Kyser, T. K. (2006). Formation of the auriferous and barren North Dipper Veins in the Sigma Mine, Val d'Or, Canada: constraints from structural, mineralogical, fluid Inclusion, and isotopic data. *Economic Geology, 101*(3), 607-631.

Percival, J. A. (2007). Geology and metallogeny of the Superior Province, Canada. In W. D. Goodfellow (Ed.), *Mineral deposits of Canada: A synthesis of major deposit-types, district metallogeny, the evolution of geological provinces, and exploration methods* (Vol. 5, pp. 903-928): Geological Association of Canada, Mineral Deposits Division.

Petrella, L., Thébaud, N., Evans, K., LaFlamme, C., & Occhipinti, S. (2021). The role of competitive fluid-rock interaction processes in the formation of high-grade gold deposits. *Geochimica Et Cosmochimica Acta, 313*, 38-54.

Pettijohn, F. J., Potter, P. E., & Siever, R. (1973). *Sand and sandstone*: Springer Science & Business Media.

Phillips, G., & Powell, R. (2010). Formation of gold deposits: a metamorphic devolatilization model. *Journal of Metamorphic Geology, 28*(6), 689-718.

Pitcairn, I., Leventis, N., Beaudoin, G., & Dubé, B. (2017). *A metasedimentary source for orogenic gold in the Abitibi belt?*

Pitcairn, I. K., Leventis, N., Beaudoin, G., Faure, S., Guilmette, C., & Dubé, B. (2021). A metasedimentary source of gold in Archean orogenic gold deposits. *Geology, 49*(7), 862-866.

Pitcairn, I. K., Teagle, D. A., Craw, D., Olivo, G. R., Kerrich, R., & Brewer, T. S. (2006). Sources of metals and fluids in orogenic gold deposits: insights from the Otago and Alpine Schists, New Zealand. *Economic Geology, 101*(8), 1525-1546.

Pokrovski, G. S., Kokh, M. A., Guillaume, D., Borisova, A. Y., Gisquet, P., Hazemann, J. L., . . . Dubessy, J. (2015). Sulfur radical species form gold deposits on Earth. *Proceedings of the National Academy of Sciences of the United States of America, 112*(44), 13484-13489. doi:10.1073/pnas.1506378112

Polat, A., Frei, R., Longstaffe, F. J., Thorkelson, D. J., & Friedman, E. (2018). Petrology and geochemistry of the Tasse mantle xenoliths of the Canadian Cordillera: a record of Archean to Quaternary mantle growth, metasomatism, removal, and melting. *Tectonophysics, 737*, 1-26.

Pope, E. C., Bird, D. K., & Rosing, M. T. (2012). Isotope composition and volume of Earth's early oceans. *Proceedings of the National Academy of Sciences, 109*(12), 4371-4376.

Poulsen, K. H. (2000). Geological classification of Canadian gold deposits. *Bulletin of the Geological Survey of Canada, 540*, 1-106.

Poulsen, K. H., Monecke, T., Mercier-Langevin, P., & Dubé, B. (2017). The Larder Lake-Cadillac Break and Its Gold Districts. In *Archean Base and Precious Metal Deposits, Southern Abitibi Greenstone Belt, Canada* (Vol. 19, pp. 0): Society of Economic Geologists.

Powell, W., Carmichael, D., & Hodgson, C. (1995). Conditions and timing of metamorphism in the southern Abitibi greenstone belt, Quebec. *Canadian Journal of Earth Sciences, 32*(6), 787-805.

Powell, W. G. (1991). *The distribution, structural history and relationship to regional metamorphism of high-strain zones forming the Larder Lake-Cadillac deformation zone, Matachewan area, Abitibi belt.* (Thesis (M.Sc., Geological Sciences)). Queen's University, Kingston, Ontario.

Powell, W. G., & Hodgson, C. J. (1992). Deformation of the Gowganda Formation, Matachewan area, Ontario, by post-Early Proterozoic reactivation of the Archean Larder Lake–Cadillac Break, with implications for gold exploration. *Canadian Journal of Earth Sciences, 29*(7), 1580-1589. doi:10.1139/e92-124

Quesnel, B., Scheffer, C., & Beaudoin, G. (in press). The light stable isotope (H, B, C, N, O, Si, S) composition of orogenic gold deposits. In *Isotopes in mineral exploration*: SpringerNature.

Rafini, S. (2014). Fiches descriptives de gîtes – Faille de Cadillac. Projet CONSOREM 2011-01 et 2012-01. 187.

Raskevicius, T., Beaudoin, G., Kyser, K., Perrouty, S., & Gaillard, N. (2019). Whole-rock δ2H and δ18O footprint of the Canadian Malartic gold deposit, Pontiac Subprovince, Québec, Canada. *Mineralium Deposita*, 1-18.

Rehm, A. G., Jørgensen, T. R., Thurston, P. C., Gibson, H. L., & Lafrance, B. (2021). Synsedimentary rifting and basaltic-komatiitic volcanism in the Pontiac subprovince, Superior craton (Canada): Implications for Neoarchean geodynamics. *Precambrian Research, 362*, 106204.

Ridley, J., Mikucki, E., & Groves, D. (1996). Archean lode-gold deposits: fluid flow and chemical evolution in vertically extensive hydrothermal systems. *Ore Geology Reviews, 10*(3-6), 279-293.

Ridley, J. R., & Diamond, L. (2000). Fluid chemistry of orogenic lode gold deposits and implications for genetic models. In S. G. Hagemann & P. Brown (Eds.), *Gold in 2000* (Vol. 13, pp. 141-162): Society of Economic Geologists, Inc.

Robert, F. (1989). Internal structure of the Cadillac tectonic zone southeast of Val d'Or, Abitibi greenstone belt, Quebec. *Canadian Journal of Earth Sciences, 26*(12), 2661-2675. doi:10.1139/e89-226

Robert, F., Boullier, A. M., & Firdaous, K. (1995). Gold-quartz veins in metamorphic terranes and their bearing on the role of fluids in faulting. *Journal of Geophysical Research: Solid Earth, 100*(B7), 12861-12879.

Robert, F., Brommecker, R., Bubar, D., Rive, M., Verpaelst, P., Gagnon, Y., . . . Simard, A. (1990). *The Orenada Zone 4 deposit: Deformed vein-type gold mineralization within the Cadillac tectonic zone, SE of Val d'Or* (Vol. 43): Canadian Institute of Mining and Metallurgy.

Robert, F., & Kelly, W. C. (1987). Ore-forming fluids in Archean gold-bearing quartz veins at the Sigma Mine, Abitibi greenstone belt, Quebec, Canada. *Economic Geology, 82*(6), 1464-1482. doi:10.2113/gsecongeo.82.6.1464

Rosenbaum, J., & Sheppard, S. (1986). An isotopic study of siderites, dolomites and ankerites at high temperatures. *Geochimica Et Cosmochimica Acta, 50*(6), 1147-1150.

Ross, P. S., Goutier, J., Mercier-Langevin, P., & Dube, B. (2011). Basaltic to andesitic volcaniclastic rocks in the Blake River Group, Abitibi Greenstone Belt: 1. Mode of emplacement in three areas. *Canadian Journal of Earth Sciences, 48*(4), 728-756. doi:10.1139/e10-090

Salmon, B., & McDonough, B. (2011). *Technical report on the Rouyn property,-Rouyn-Noranda, Québec, Canada*. Retrieved from https://www.yorbeauresources.com/document/en/2089-TechnicalReport.pdf

Sarkar, T., Dubinina, E. O., Harris, C., Maier, W. D., & Mouri, H. (2018). Petrogenesis of ultramafic rocks of komatiitic composition from the Central Zone of the Limpopo Belt, South Africa: Evidence from O and H isotopes. *Journal of African Earth Sciences, 147*, 68-77.

Savard, C., Beaudoin, G., & Therrien, R. (2007). Numerical modelling of 3D fluid flow and oxygen isotope exchange in fractured media: spatial distribution of isotope patterns. *Geofluids, 7*(4), 387-400.

Sharma, S. D., Patil, D., & Gopalan, K. (2002). Temperature dependence of oxygen isotope fractionation of CO2 from magnesite-phosphoric acid reaction. *Geochimica Et Cosmochimica Acta, 66*(4), 589-593.

Sharp, Z. (2017). *Principles of stable isotope geochemistry* (2nd edition ed.): The University of New Mexico.

Sharp, Z., & Kirschner, D. (1994). Quartz-calcite oxygen isotope thermometry: A calibration based on natural isotopic variations. *Geochimica Et Cosmochimica Acta, 58*(20), 4491-4501.

Shenberger, D., & Barnes, H. (1989). Solubility of gold in aqueous sulfide solutions from 150 to 350 C. *Geochimica Et Cosmochimica Acta, 53*(2), 269-278.

Sheppard, S. M. (1986). Characterization and isotopic variations in natural waters. *Stable isotopes in high temperature geological processes*, 165-184.

Sibson, R. H., Robert, F., & Poulsen, K. H. (1988). High-angle reverse faults, fluid-pressure cycling, and mesothermal gold-quartz deposits. *Geological Society of America, 16*(6), 551-555. doi:10.1130/0091-7613(1988)016<0551:Harffp>2.3.Co;2

Singhal, B. B. S., & Gupta, R. P. (2010). *Applied hydrogeology of fractured rocks*: Springer Science & Business Media.

Smith, H., O'Neil, J., & Erlank, A. (1984). Oxygen isotope compositions of minerals and rocks and chemical alteration patterns in pillow lavas from the Barberton greenstone belt, South Africa. In *Archaean Geochemistry* (pp. 115-137): Springer.

Srisutthiyakorn, N., & Mavko, G. (2016). Hydraulic tortuosity: From artificial packs to natural rocks. In *SEG Technical Program Expanded Abstracts 2016* (pp. 3133-3137): Society of Exploration Geophysicists.

Sugiono, D., LaFlamme, C., Thébaud, N., Martin, L., Savard, D., & Fiorentini, M. (2022). Fault-induced gold saturation of a single auriferous fluid is a key process for orogenic gold deposit formation. *Economic Geology*.

Taylor, H. P., & Sheppard, S. M. (1986). Igneous rocks; I, Processes of isotopic fractionation and isotope systematics. *Reviews in Mineralogy and Geochemistry, 16*(1), 227-271.

Taylor, H. P. J. (1978). Oxygen and hydrogen isotope studies of plutonic granitic rocks. *Earth and Planetary Science Letters, 38*(1), 177-210. doi:10.1016/0012-821x(78)90131-0

Therrien, R., & Sudicky, E. (1996). Three-dimensional analysis of variably-saturated flow and solute transport in discretely-fractured porous media. *Journal of Contaminant Hydrology, 23*(1-2), 1-44.

Thurston, P., Ayer, J., Goutier, J., & Hamilton, M. (2008). Depositional gaps in Abitibi greenstone belt stratigraphy: A key to exploration for syngenetic mineralization. *Economic Geology, 103*(6), 1097-1134.

Thurston, P. C. (2015). Igneous Rock Associations 19. Greenstone Belts and Granite-Greenstone Terranes: Constraints on the Nature of the Archean World. *Geoscience Canada, 42*, 437-484. doi:10.12789/geocanj.2015.42.081

Tomkins, A. G. (2013). On the source of orogenic gold. *Geology, 41*(12), 1255-1256. doi:10.1130/focus122013.1

Uemoto, T., Ridley, J., Mikucki, E., Groves, D. I., & Kusakabe, M. (2002). Fluid chemical evolution as a factor in controlling the distribution of gold at the Archean Golden Crown lode gold deposit, Murchison province, Western Australia. *Economic Geology, 97*(6), 1227-1248.

Vho, A., Lanari, P., & Rubatto, D. (2019). An internally-consistent database for oxygen isotope fractionation between minerals. *Journal of Petrology, 60*(11), 2101-2129.

Ward, J., Mavrogenes, J., Murray, A., & Holden, P. (2017). Trace element and sulfur isotopic evidence for redox changes during formation of the Wallaby Gold Deposit, Western Australia. *Ore Geology Reviews, 82*, 31-48.

Weatherley, D. K., & Henley, R. W. (2013). Flash vaporization during earthquakes evidenced by gold deposits. *Nature Geoscience, 6*(4), 294-298.

Whitmore, D., Berry, L., & Hawley, J. (1946). Chrome micas. *American Mineralogist: Journal of Earth and Planetary Materials, 31*(1-2), 1-21.

Wilson, M. E. (1962). *Rouyn-Beauchastel Map-areas, Quebec*: Geological Survey of Canada.

Wyman, D., & Kerrich, R. (2009). Plume and arc magmatism in the Abitibi subprovince: implications for the origin of Archean continental lithospheric mantle. *Precambrian Research, 168*(1-2), 4-22.

Wyman, D., Kerrich, R., & Polat, A. (2002). Assembly of Archean cratonic mantle lithosphere and crust: plume–arc interaction in the Abitibi–Wawa subduction–accretion complex. *Precambrian Research, 115*(1-4), 37-62.

Wyman, D. A., Cassidy, K. F., & Hollings, P. (2016). Orogenic gold and the mineral systems approach: Resolving fact, fiction and fantasy. *Ore Geology Reviews, 78*, 322-335. doi:10.1016/j.oregeorev.2016.04.006

Xu, M., & Eckstein, Y. (1995). Use of weighted least-squares method in evaluation of the relationship between dispersivity and field scale. *Groundwater, 33*(6), 905-908.

Xue, Y. X., Campbell, I., & Ireland, T. R. (2013). No mass-independent sulfur isotope fractionation in auriferous fluids supports a magmatic origin for Archean gold deposits. *Geology, 41*(7), 791-794. doi:10.1130/g34186.1

Zhang, X., Nesbitt, B. E., & Muehlenbachs, K. (1989). Gold mineralization in the Okanagan Valley, southern British Columbia; fluid inclusion and stable isotope studies. *Economic Geology, 84*(2), 410-424.

Appendix A – Geostatistical model

Geostatistical analyses of the spatial variation of $\delta^{18}O_{H2O}$ and alteration indices were done using ArcGIS software. The method chosen is the inverse weighted (IDW) interpolation, which uses a linearly weighted combination of a set of sample points to estimate the unknown cell values through interpolation, and from which the weight is a function of inverse distance. The method assumes a decrease in influence with distance of the variable being mapped from its sampled location. The software uses the method and equations presented in Watson and Philip (1985).

- Watson, D., & Philip, G. (1985). A refinement of inverse distance weighted interpolation. Geo-processing, 2(4), 315-327.

Appendix B – Lithogeochemical data

Table B.1 Whole-rock lithogeochemistry and isotopic data of sampled host rocks.

	LOD	19-GR-124S-04 Talc-chlorite-carbonate schist	19-GR-405S-15 Carbonate schist	19-GR-442S-09 Carbonate schist	19-GR-415S-09 Carbonate-fuchsite schist	19-GR-425S-03 Carbonate-fuchsite schist	19-GR-467CI-04 Carbonate schist	19-GR-564CI-07 Carbonate schist	19-GR-603CI-04 Carbonate schist	19-GR-620CI-04 Carbonate schist	19-GR-535CI-03 Carbonate-fuchsite schist	19-GR-610CI-06 Carbonate-fuchsite schist	19-GR-461GA-05 Carbonate-fuchsite schist	19-GR-500GA-07 Carbonate-fuchsite schist
H_2O^+ (%)	<0.01	6.12	3.7	1.09	1.19	1.64		2.66	3.07	3.56	0.68	3.04	2.04	0.19
SiO_2 (%)	<0.01	34.6	32.6	56.5	32.4	33.9		33.4	33.8	39.6	29.9	32.9	31	39.4
Al2O3 (%)	<0.01	4.8	5.09	4.31	4.9	4.81		5.16	5.97	5.07	4.31	4.99	4.12	11.75
Fe_2O_3 (%)	<0.01	9.72	8.74	3.72	8.81	8.2		8.6	9.18	8.96	8.61	9.11	10.05	4.55
CaO (%)	<0.01	7.36	9.82	9.65	2.35	3.4		5.28	11.05	1.27	16.65	6.08	1.16	10.2
MgO (%)	<0.01	25.7	17.75	8.38	22.1	21.1		20.4	14.3	22.6	9.99	20.5	24.4	7.47
Na_2O (%)	<0.01	b.d.l	b.d.l	0.27	0.95	0.24		0.51	0.68	b.d.l	0.15	0.07	0.01	6.64
K_2O (%)	<0.01	0.03	0.02	b.d.l	0.73	0.64		b.d.l	0.04	0.01	1.23	b.d.l	0.63	0.16
Cr_2O_3 (%)	<0.002	0.315	0.289	0.166	0.288	0.24		0.268	0.287	0.304	0.275	0.278	0.339	0.509
TiO_2 (%)	<0.01	0.24	0.26	0.18	0.24	0.24		0.2	0.28	0.24	0.27	0.28	0.27	0.52
MnO (%)	<0.01	0.2	0.17	0.1	0.12	0.13		0.12	0.13	0.08	0.26	0.14	0.09	0.14
P_2O_5 (%)	<0.01	0.01	0.02	b.d.l	0.01	0.01		0.01	0.03	0.01	0.23	0.04	0.02	b.d.l
SrO (%)	<0.01	0.01	0.01	0.02	b.d.l	0.02		0.01	0.02	b.d.l	0.02	0.02	b.d.l	0.02
BaO (%)	<0.01	b.d.l	b.d.l	b.d.l	0.02	0.01		b.d.l	b.d.l	b.d.l	0.02	b.d.l	0.01	0.01
LOI (%)	n/a	16.45	23.8	15.9	26.9	26.6		25.1	22.8	22.3	20.8	25.5	27.6	16.75
Total (%)	n/a	99.44	98.57	99.2	99.82	99.54		99.06	98.57	100.44	92.72	99.91	99.7	98.12
C (%)	<0.05	2.94	5.67	3.76	6.66	6.35		6.28	5.53	4.69	6.88	6.39	6.31	4.71
CO_2 (%)	<0.2	10.8	20.8	13.8	24.4	23.3		23	20.3	17.2	25.2	23.4	23.1	17.3
C (%)	<0.01	3.19	5.86	3.81	7.35	7.09		6.4	5.76	5.39	6.9	6.36	7.35	4.72
S (%)	<0.01	0.03	0.09	0.24	0.1	0.09		0.08	0.15	0.07	2.73	0.14	0.11	0.13
$\delta^{13}C_{carbonate}$ (‰ VPDB)	n/a	-3.1	-3.5	-3.5	-4.0	-3.3	-4.5	-3.7	-3.8	-3.0	-4.7	-3.2	-4.2	-5.0
$\delta^{18}O_{carbonate}$ (‰ VSMOW)	n/a	12.1	14.0	13.9	13.7	13.9	13.0	13.7	12.9	15.4	12.4	13.0	13.9	12.6
$\delta^{18}O$ (‰ VSMOW)	n/a	7.9	9.8	11.7	9.6	9.7	10.3	9.7	9.3	11.1	9.4	9.7	9.9	9.6

Table B.1 Whole-rock lithogeochemistry and isotopic data of sampled host rocks. (Continued)

		19-GR-574GA-05	19-GR-645AS-07	19-GR-656AS-06	19-GR-638AS-06	19-GR-04EB-01	19-GR-12A-08	19-GR-17A-05	19-GR-475SC-03	19-GR-650AS-02	19-GR-631AUG-01	19-GR-628GA-02
	LOD	Carbonate-fuchsite schist	Carbonate schist	Carbonate schist	Carbonate-fuchsite schist	Carbonate schist	Carbonate schist	Carbonate schist	Talc-chlorite-carbonate schist	Albitite dyke	Greywacke	Greywacke
H_2O^+ (%)	<0.01	3.39	3.61	2.98	2.44	1.52	4.04	4.12	6.97	5.45	1.88	
SiO_2 (%)	<0.01	34.4	35.6	37	32.9	52.9	32.7	37	48.5	48.9	69.5	
Al2O3 (%)	<0.01	5.94	4.93	4.36	4.18	9.94	6.24	5.49	4.3	17.2	12.3	
Fe_2O_3 (%)	<0.01	11.05	9.05	7.93	8.75	5.84	10.05	8.71	10.5	9.29	2.79	
CaO (%)	<0.01	4.34	13.2	13.45	3.62	7.71	12.85	12.35	2.09	0.96	3.45	
MgO (%)	<0.01	19.6	13	12.95	23.5	6.11	13.45	13.55	25.8	11.35	2.36	
Na_2O (%)	<0.01	0.37	0.02	b.d.l	0.07	3.01	0.13	b.d.l	b.d.l	5.24	2.46	
K_2O (%)	<0.01	0.08	0.06	0.03	0.05	0.79	0.07	b.d.l	0.03	0.11	2.26	
Cr_2O_3 (%)	<0.002	0.372	0.285	0.277	0.266	0.118	0.319	0.274	0.334	0.003	0.012	
TiO_2 (%)	<0.01	0.36	0.25	0.27	0.22	0.39	0.39	0.37	0.35	1.06	0.28	
MnO (%)	<0.01	0.19	0.24	0.21	0.13	0.13	0.27	0.25	0.07	0.03	0.06	
P_2O_5 (%)	<0.01	0.02	0.02	b.d.l	0.01	0.12	0.04	0.07	0.02	0.33	0.08	
SrO (%)	<0.01	b.d.l	b.d.l	0.01	b.d.l	0.02	0.01	0.05	b.d.l	0.03	0.05	
BaO (%)	<0.01	b.d.l	b.d.l	b.d.l	b.d.l	0.03	b.d.l	b.d.l	b.d.l	0.01	0.08	
LOI (%)	n/a	23.1	23.2	21.6	26.8	13.25	22.4	21.6	6.77	5.82	4.8	
Total (%)	n/a	99.82	99.86	98.09	100.5	100.36	98.92	99.71	98.76	100.33	100.48	
C (%)	<0.05	5.12	5.62	5.21	6.43	3.17	5.44	5.04	0.4	0.12	0.86	
CO_2 (%)	<0.2	18.8	20.6	19.1	23.6	11.6	19.9	18.5	1.5	0.4	3.2	
C (%)	<0.01	5.74	5.63	5.33	6.88	3.35	5.47	5.07	0.41	0.14	0.87	
S (%)	<0.01	0.09	0.17	0.06	0.06	0.27	0.08	0.08	0.03	1.67	0.09	
$\delta^{13}C_{carbonate}$ (‰ VPDB)	n/a	-4.9	-4.9	-4.4	-4.3	-4.5	-6.0	-4.2	-2.9	-4.3	-6.7	-2.2
$\delta^{18}O_{carbonate}$ (‰ VSMOW)	n/a	13.3	11.1	10.2	14.4	13.1	12.8	10.6	14.6	11.4	13.2	13.8
$\delta^{18}O$ (‰ VSMOW)	n/a	9.5	7.5	7.8	9.9	10.0	9.7	8.1	11.2	6.5	11.7	12.7

Table B.1 Whole-rock lithogeochemistry and isotopic data of sampled host rocks. (Continued)

		19-GR-299AS-09	19-GR-472BO-04	19-GR-473BO-04	19-GR-480BW-01	19-GR-476SC-06	19-GR-483BW-05	19-GR-652BO-05	19-GR-10010AS-03	19-GR-10013AS-04
	LOD	Greywacke	Greywacke	Greywacke	Greywacke	Greywacke	Greywacke	Greywacke	Tremolite schist	Tremolite schist
H_2O^+ (%)	<0.01	3.98	2.6	3.59	1.04	3.89	4.31	1.67	9.59	7.23
SiO_2 (%)	<0.01	52.9	66.8	57.8	71.8	52.7	51	62.8	40.8	45.1
Al2O3 (%)	<0.01	15.6	14.8	16.25	12.2	19.3	11.65	13.85	9.51	5.94
Fe_2O_3 (%)	<0.01	14.2	5.03	6.25	3.13	5.01	9.81	5.05	12.8	11.15
CaO (%)	<0.01	0.98	1.18	3.85	1.79	8.19	6.4	2.82	5.97	4.83
MgO (%)	<0.01	2.58	3.1	3.76	1.32	2.66	8.22	2.4	24.9	24.9
Na_2O (%)	<0.01	3.23	4.98	3.01	3.5	2.64	2.15	4.13	0.15	0.34
K_2O (%)	<0.01	2.25	0.89	2.53	2.17	0.53	1.44	1.85	0.35	1.03
Cr_2O_3 (%)	<0.002	0.067	0.028	0.035	0.017	0.028	0.073	0.033	0.18	0.39
TiO_2 (%)	<0.01	0.67	0.52	0.64	0.39	0.48	0.71	0.52	0.05	0.3
MnO (%)	<0.01	0.03	0.05	0.08	0.05	0.18	0.15	0.08	0.12	0.15
P_2O_5 (%)	<0.01	0.14	0.18	0.2	0.09	0.03	0.21	0.1	0.02	0.01
SrO (%)	<0.01	b.d.l	0.04	0.03	0.04	0.01	0.05	0.03	b.d.l	b.d.l
BaO (%)	<0.01	0.06	0.04	0.06	0.06	0.01	0.02	0.04	0.01	0.01
LOI (%)	n/a	8.13	2.7	5.68	3.4	7.73	7.79	5.15	7.03	6.27
Total (%)	n/a	100.84	100.34	100.18	99.96	99.5	99.67	98.85	101.89	100.42
C (%)	<0.05	0.24	0.15	0.77	0.68	1.27	1.28	1.13	0.07	0.2
CO_2 (%)	<0.2	0.9	0.6	2.8	2.5	4.7	4.7	4.2	0.3	0.7
C (%)	<0.01	0.33	0.16	0.77	0.68	1.24	1.24	1.14	0.06	0.17
S (%)	<0.01	5.52	0.04	0.08	0.38	0.04	0.1	0.25	0.02	0.02
$\delta^{13}C_{carbonate}$ (‰ VPDB)	n/a	-5.0	-4.4	-4.7	-5.3	-4.4	-2.4	-6.8	-5.6	-2.1
$\delta^{18}O_{carbonate}$ (‰ VSMOW)	n/a	15.5	13.3	12.1	13.3	13.6	12.2	15.1	13.0	12.6
$\delta^{18}O$ (‰ VSMOW)	n/a	10.6	10.5	10.1	12.0	11.6	9.7	13.5	7.7	7.3

*Not enough available material for whole-rock lithogeochemistry

Appendix C – Carbonate EPMA data

Table C.1 Vein carbonate EPMA analyses in weight%.

Block	Host rock	Sample	Analysis #	Mineral		$MgCO_3$	$CaCO_3$	$MnCO_3$	$FeCO_3$	$SrCO_3$	Mg/(Fe+Mg)
					LOD	<0.008	<0.008	<0.014	<0.034	<0.016	n/a
Augmitto	Carbonate schist	19-GR-405S-14	1	Fe-dolomite		41.09	53.6	0.15	5.16	0.04	0.87
	Carbonate schist		2	Fe-magnesite		75.01	0.3	0.48	24.17	0.00	0.72
	Albitite dyke	19-GR-442S-02	1	Fe-dolomite		38.96	52.8	0.54	7.55	0.10	0.81
	Albitite dyke		2	Fe-dolomite		39.13	52.7	0.23	7.84	0.12	0.80
	Talc-chlorite-carbonate schist	19-GR-415S-04	1	Fe-dolomite		40.23	52.8	0.20	6.66	0.09	0.83
	Talc-chlorite-carbonate schist		2	Fe-dolomite		39.88	52.9	0.15	6.97	0.08	0.82
	Talc-chlorite-carbonate schist		3	Fe-dolomite		40.36	53.3	0.23	6.06	0.05	0.85
Cinderella	Carbonate schist	19-GR-535CI-05	1	Fe-dolomite		40.68	52.9	0.31	5.99	0.14	0.85
	Carbonate schist		2	Fe-dolomite		39.05	53.3	0.40	7.07	0.13	0.82
	Carbonate schist		3	Fe-dolomite		40.74	53.2	0.27	5.71	0.12	0.85
	Carbonate schist	19-GR-564CI-06	1	Fe-dolomite		40.44	53.3	0.25	5.95	0.03	0.85
	Carbonate schist		2	Fe-dolomite		40.60	53.4	0.16	5.75	0.09	0.85
	Carbonate schist	19-GR-467CI-09	1	Fe-dolomite		40.12	53.4	0.22	6.21	0.09	0.84
	Carbonate schist		2	Fe-dolomite		37.94	52.9	0.25	8.76	0.13	0.78
	Carbonate schist		3	Fe-dolomite		38.70	52.8	0.20	8.16	0.11	0.80
	Carbonate schist	19-GR-620CI-05	1	Fe-dolomite		41.02	53.3	0.09	5.58	0.05	0.86
	Carbonate schist		2	Fe-dolomite		41.01	53.3	0.09	5.56	0.08	0.86
	Carbonate schist		3	Fe-dolomite		40.78	53.2	0.11	5.81	0.08	0.85
	Carbonate schist	19-GR-620CI-06	1	Fe-dolomite		41.66	53.8	0.15	4.27	0.14	0.89
	Carbonate schist		2	Fe-magnesite		74.87	0.5	0.02	24.63	0.02	0.71
	Carbonate schist		3	Fe-magnesite		73.95	0.5	0.51	25.06	0.00	0.71
	Carbonate schist		4	Fe-magnesite		63.29	0.4	1.65	34.70	0.00	0.60
	Carbonate schist		5	Fe-magnesite		72.77	0.4	0.21	26.62	0.01	0.69
	Carbonate schist		6	Fe-magnesite		69.98	0.3	0.62	29.08	0.00	0.66
	Carbonate schist		7	Fe-dolomite		41.25	53.3	0.20	5.01	0.24	0.87
Lac Gamble	Carbonate-fuchsite schist	19-GR-461GA-04	1	Fe-dolomite		40.90	53.3	0.24	5.49	0.05	0.86
	Carbonate-fuchsite schist		2	Fe-dolomite		41.11	53.1	0.14	5.56	0.07	0.86
Astoria	Argillite	19-GR-638AS-05	1	Calcite		0.17	99.1	0.43	0.31	0.00	0.31

Table C Vein carbonate EPMA analyses in weight%. (Continued)

Block	Host rock	Sample	Analysis #	Mineral		$MgCO_3$	$CaCO_3$	$MnCO_3$	$FeCO_3$	$SrCO_3$	Mg/(Fe+Mg)
					LOD	<0.008	<0.008	<0.014	<0.034	<0.016	n/a
Astoria	Argillite	19-GR-638AS-05	2	Calcite		0.28	99.1	0.26	0.36	0.00	0.39
	Argillite		3	Calcite		0.20	99.1	0.29	0.40	0.00	0.29
	Carbonate schist	19-GR-656AS-03	1	Fe-dolomite		38.66	53.0	0.46	7.85	0.03	0.80
	Carbonate schist		2	Fe-dolomite		39.51	52.8	0.31	7.35	0.02	0.82
East-Bay	Talc-chlorite-carbonate schist	19-GR-650AS-04	1	Fe-dolomite		38.64	52.8	0.47	7.50	0.62	0.81
	Talc-chlorite-carbonate schist		2	Fe-dolomite		38.85	53.6	0.85	6.24	0.41	0.84
	Talc-chlorite-carbonate schist		3	Fe-dolomite		37.97	52.4	0.55	8.26	0.86	0.79
	Talc-chlorite-carbonate schist		4	Fe-dolomite		37.83	53.2	0.64	7.90	0.47	0.80
	Talc-chlorite-carbonate schist		5	Fe-dolomite		38.40	53.3	0.59	7.30	0.45	0.81
	Talc-chlorite-carbonate schist		6	Fe-dolomite		38.36	52.9	0.52	7.62	0.62	0.81
	Talc-chlorite-carbonate schist	19-GR-650AS-04	7	Fe-dolomite		38.39	52.5	0.55	7.77	0.78	0.80
	Carbonate schist	19-GR-04-EB-04	1	Fe-dolomite		34.59	52.5	0.70	12.12	0.14	0.70
	Carbonate schist		2	Fe-dolomite		35.39	52.1	1.12	11.31	0.05	0.72
	Carbonate schist		3	Fe-dolomite		35.05	52.4	1.13	11.43	0.04	0.72
Bouzan	Carbonate schist	19-GR-12A-04	1	Fe-dolomite		38.29	52.3	0.52	8.88	0.05	0.78
	Carbonate schist	19-GR-476SC-01	1	Calcite		0.05	99.0	0.97	0.00	0.00	
	Carbonate schist		2	Calcite		0.08	98.9	0.98	0.03	0.00	0.68
	Carbonate schist		3	Calcite		0.30	98.6	0.97	0.13	0.02	0.66
	Carbonate schist		4	Calcite		0.15	98.7	1.01	0.15	0.04	0.45
	Carbonate schist		5	Calcite		0.07	99.0	0.78	0.10	0.04	0.37
	Carbonate schist		6	Calcite		0.16	99.0	0.72	0.00	0.14	
	Carbonate schist		7	Calcite		0.11	98.7	1.10	0.09	0.01	0.52
	Carbonate schist		8	Calcite		0.13	98.7	1.02	0.11	0.02	0.50
	Calcite-chlorite schist	19-GR-475SC-02	1	Calcite		0.93	96.2	1.31	1.54	0.04	0.33
	Calcite-chlorite schist		2	Calcite		1.18	96.1	1.16	1.44	0.08	0.40
	Calcite-chlorite schist		3	Calcite		0.66	96.1	1.31	1.87	0.04	0.23
	Calcite-chlorite schist		4	Calcite		0.92	95.7	1.50	1.88	0.03	0.29
	Mafic intrusion	19-GR-652BO-01	1	Calcite		1.69	94.7	1.03	0.84	1.76	0.62
	Mafic intrusion		2	Calcite		1.53	95.1	0.96	0.63	1.76	0.67
	Mafic intrusion		3	Calcite		1.76	94.9	1.05	0.86	1.43	0.63
	Argillite	19-GR-652BO-02	1	Ankerite		25.14	50.4	0.71	23.51	0.24	0.47
	Argillite		2	Ankerite		25.44	50.0	0.65	23.75	0.19	0.47

Table C Vein carbonate EPMA analyses in weight%. (Continued)

Block	Host rock	Sample	Analysis #	Mineral		$MgCO_3$	$CaCO_3$	$MnCO_3$	$FeCO_3$	$SrCO_3$	Mg/(Fe+Mg)
					LOD	<0.008	<0.008	<0.014	<0.034	<0.016	n/a
Bouzan	Argillite	19-GR-652BO-02	3	Ankerite		23.91	50.1	0.70	25.06	0.20	0.44
	Greywacke	19-GR-483BW-03	1	Calcite		1.50	95.3	1.27	1.65	0.27	0.43
	Andesite	19-GR-17A-01	1	Calcite		0.77	97.2	0.70	1.12	0.19	0.36
	Greywacke	19-GR-472BO-03	1	Calcite		0.53	95.8	1.70	1.37	0.59	0.24
	Greywacke		2	Calcite		0.43	96.6	1.36	1.27	0.32	0.22
	Greywacke		3	Calcite		0.06	98.8	1.16	0.00	0.00	
	Greywacke		4	Calcite		0.36	98.0	0.96	0.54	0.15	0.35
	Greywacke		5	Calcite		0.41	98.0	0.94	0.40	0.26	0.46
	Greywacke		6	Calcite		0.41	97.3	1.23	0.64	0.40	0.35
	Greywacke		7	Calcite		0.20	98.5	0.92	0.24	0.14	0.41

Appendix D – Tourmaline EPMA data

Table D.1 Vein tourmaline EPMA analyses in weight%. The conversion in apfu for a formula based on 29 oxygen atoms was done according to Henry et al. (2011).

Sample		19-GR-124S-01			19-GR-405S-14			19-GR-442S-02				
Host rock[1]		Talc-chlorite-carbonate schist			Carbonate schist			Albitite dyke				
Analysis #		1	2	3	1	2	3	1	2	3	4	5
Tourmaline species		Dravite	Dravite	Dravite	Dravite	Dravite	Dravite	Dravite	Dravite	Dravite	Dravite	Dravite
	LOD											
SiO_2 (%)	<0.007	36.89	36.53	36.71	36.66	36.79	36.30	36.38	36.11	36.93	36.95	36.66
TiO_2 (%)	<0.025	0.62	0.59	0.97	0.52	0.42	0.91	0.06	0.06	0.64	0.74	0.73
B_2O_3 (%)[3]	n/a	14.48	14.54	14.79	14.60	14.49	14.97	15.84	15.63	14.35	14.27	14.04
Al_2O_3 (%)	<0.008	32.02	31.39	31.86	32.65	33.08	32.00	32.70	33.43	32.51	32.29	33.08
Cr_2O_3 (%)	<0.011	0.65	2.15	0.02	0.22	0.78	0.94	0.00	0.02	0.10	0.00	0.00
MgO (%)	<0.007	9.53	9.23	9.64	9.20	8.94	8.96	8.69	9.38	9.55	9.56	9.32
CaO (%)	<0.006	0.15	0.15	0.22	0.25	0.13	0.20	0.28	0.04	0.24	0.25	0.16
MnO (%)	<0.011	0.02	0.00	0.00	0.01	0.01	0.00	0.03	0.00	0.00	0.00	0.00
FeO (%)	<0.03	3.00	2.87	3.02	3.39	2.81	3.11	3.99	3.16	3.05	3.32	3.19
Na_2O (%)	<0.009	2.63	2.54	2.76	2.50	2.55	2.61	2.03	2.17	2.63	2.62	2.82
K_2O (%)	<0.006	0.01	0.01	0.02	0.00	0.01	0.00	0.00	0.01	0.00	0.00	0.01
Formula based on 29 O												
B		3.00	3.00	3.00	3.00	3.00	3.00	3.00	3.00	3.00	3.00	3.00
Si		5.96	5.94	5.95	5.93	5.93	5.91	5.97	5.89	5.95	5.96	5.89
Ti		0.08	0.07	0.12	0.06	0.05	0.11	0.01	0.01	0.08	0.09	0.09
Al		6.10	6.01	6.09	6.23	6.29	6.14	6.33	6.43	6.18	6.14	6.27
Cr		0.08	0.28	0.00	0.03	0.10	0.12	0.00	0.00	0.01	0.00	0.00
Fe^{2+}		0.41	0.39	0.41	0.46	0.38	0.42	0.55	0.43	0.41	0.45	0.43
Mn		0.00	0.00	0.00	0.00	0.00	0.00	0.00	0.00	0.00	0.00	0.00
Mg		2.30	2.24	2.33	2.22	2.15	2.18	2.13	2.28	2.30	2.30	2.23
Ca		0.03	0.03	0.04	0.04	0.02	0.04	0.05	0.01	0.04	0.04	0.03
Na		0.82	0.80	0.87	0.78	0.80	0.83	0.65	0.68	0.82	0.82	0.88
K		0.00	0.00	0.00	0.00	0.00	0.00	0.00	0.00	0.00	0.00	0.00
X site												
Na		0.82	0.80	0.87	0.78	0.80	0.83	0.65	0.68	0.82	0.82	0.88
K		0.00	0.00	0.00	0.00	0.00	0.00	0.00	0.00	0.00	0.00	0.00
Ca		0.03	0.03	0.04	0.04	0.02	0.04	0.05	0.01	0.04	0.04	0.03
X-Vac		0.15	0.17	0.09	0.17	0.18	0.14	0.30	0.31	0.14	0.14	0.09
Y site												
Fe^{2+}		0.41	0.39	0.41	0.46	0.38	0.42	0.55	0.43	0.41	0.45	0.43
Mg		2.30	2.24	2.33	2.22	2.15	2.18	2.13	2.28	2.30	2.30	2.23
Mn^{2+}		0.00	0.00	0.00	0.00	0.00	0.00	0.00	0.00	0.00	0.00	0.00
Al^{3+}		0.07	0.00	0.04	0.16	0.22	0.06	0.30	0.32	0.13	0.09	0.16
Cr^{3+}		0.08	0.22	0.00	0.03	0.10	0.12	0.00	0.00	0.01	0.00	0.00
Ti		0.08	0.07	0.12	0.06	0.05	0.11	0.01	0.01	0.08	0.09	0.09
Mg/(Mg+Fe) Y site		0.85	0.85	0.85	0.83	0.85	0.84	0.80	0.84	0.85	0.84	0.84
Na/(Na+Ca) X site		0.97	0.97	0.96	0.95	0.97	0.96	0.93	0.99	0.95	0.95	0.97
$^{X-}\square/(^{X-}+Na^{1+}+K^{1+})$		0.15	0.18	0.09	0.18	0.18	0.14	0.32	0.31	0.14	0.14	0.09

Table D Vein tourmaline EPMA analyses in weight% and apfu. (Continued)

Sample		19-GR-415S-04			19-GR-564CI-06			19-GR-603CI-06			
Host rock[1]		Talc-chlorite-carbonate schist			Carbonate schist			Carbonate schist			
Analysis #		1	2	3	1	2	3	1	2	3	4
Tourmaline species		Dravite	Dravite	Dravite	Dravite	Dravite	Dravite	Dravite	Dravite	Dravite	Dravite
	LOD										
SiO_2 (%)	<0.007	37.01	36.86	36.76	36.88	36.70	36.94	37.46	37.09	36.77	36.83
TiO_2 (%)	<0.025	0.07	0.51	0.15	0.20	0.11	0.57	0.51	0.22	0.14	0.33
B_2O_3 (%)[3]	n/a	14.64	14.48	14.81	14.46	14.87	14.02	13.56	14.40	14.79	14.67
Al_2O_3 (%)	<0.008	33.66	32.85	33.86	32.94	33.50	32.75	33.72	34.46	33.50	33.60
Cr_2O_3 (%)	<0.011	0.05	0.01	0.10	0.03	0.01	0.03	0.07	0.06	0.00	0.18
MgO (%)	<0.007	9.55	8.97	9.08	9.62	9.28	9.58	8.92	8.61	9.30	8.96
CaO (%)	<0.006	0.04	0.16	0.05	0.11	0.10	0.14	0.15	0.12	0.06	0.20
MnO (%)	<0.011	0.00	0.01	0.00	0.00	0.00	0.00	0.01	0.01	0.00	0.00
FeO (%)	<0.03	2.83	3.65	3.06	2.98	2.64	3.20	2.88	2.58	3.30	2.89
Na_2O (%)	<0.009	2.15	2.49	2.15	2.76	2.78	2.77	2.71	2.45	2.14	2.35
K_2O (%)	<0.006	0.00	0.02	0.00	0.02	0.01	0.01	0.01	0.00	0.01	0.00
Formula based on 29 O											
B		3.00	3.00	3.00	3.00	3.00	3.00	3.00	3.00	3.00	3.00
Si		5.95	5.96	5.93	5.95	5.93	5.94	5.96	5.94	5.94	5.93
Ti		0.01	0.06	0.02	0.02	0.01	0.07	0.06	0.03	0.02	0.04
Al		6.38	6.26	6.43	6.26	6.38	6.20	6.33	6.50	6.37	6.38
Cr		0.01	0.00	0.01	0.00	0.00	0.00	0.01	0.01	0.00	0.02
Fe^{2+}		0.38	0.49	0.41	0.40	0.36	0.43	0.38	0.35	0.44	0.39
Mn		0.00	0.00	0.00	0.00	0.00	0.00	0.00	0.00	0.00	0.00
Mg		2.29	2.16	2.18	2.31	2.24	2.29	2.12	2.05	2.24	2.15
Ca		0.01	0.03	0.01	0.02	0.02	0.02	0.03	0.02	0.01	0.03
Na		0.67	0.78	0.67	0.86	0.87	0.86	0.83	0.76	0.67	0.74
K		0.00	0.00	0.00	0.00	0.00	0.00	0.00	0.00	0.00	0.00
X site											
Na		0.67	0.78	0.67	0.86	0.87	0.86	0.83	0.76	0.67	0.74
K		0.00	0.00	0.00	0.00	0.00	0.00	0.00	0.00	0.00	0.00
Ca		0.01	0.03	0.01	0.02	0.02	0.02	0.03	0.02	0.01	0.03
X-Vac		0.32	0.19	0.32	0.11	0.11	0.11	0.14	0.22	0.32	0.23
Y site											
Fe^{2+}		0.38	0.49	0.41	0.40	0.36	0.43	0.38	0.35	0.44	0.39
Mg		2.29	2.16	2.18	2.31	2.24	2.29	2.12	2.05	2.24	2.15
Mn^{2+}		0.00	0.00	0.00	0.00	0.00	0.00	0.00	0.00	0.00	0.00
Al^{3+}		0.33	0.21	0.36	0.20	0.31	0.14	0.29	0.44	0.31	0.32
Cr^{3+}		0.01	0.00	0.01	0.00	0.00	0.00	0.01	0.01	0.00	0.02
Ti		0.01	0.06	0.02	0.02	0.01	0.07	0.06	0.03	0.02	0.04
Mg/(Mg+Fe) Y site		0.86	0.81	0.84	0.85	0.86	0.84	0.85	0.86	0.83	0.85
Na/(Na+Ca) X site		0.99	0.97	0.99	0.98	0.98	0.97	0.97	0.97	0.98	0.96
$^{x}\square/(^{x}\square+Na^{1+}+K^{1+})$		0.33	0.19	0.32	0.12	0.11	0.11	0.14	0.23	0.32	0.24

Table D Vein tourmaline EPMA analyses in weight% and apfu. (Continued)

Sample		19-GR-467CI-09			19-GR-620CI-06						
Host rock[1]		Carbonate schist			Carbonate schist						
Analysis #		1	2	3	1	2	3	4	5	6	7	8
Tourmaline species		Dravite	Dravite	Dravite	Dravite	Dravite	Dravite	Dravite	Dravite	Dravite	Dravite	Dravite
	LOD											
SiO_2 (%)	<0.007	36.95	39.07	36.81	36.70	36.13	36.29	36.79	36.87	36.32	36.27	36.48
TiO_2 (%)	<0.025	0.27	0.62	0.48	0.31	0.55	0.39	0.27	0.50	0.21	0.25	0.14
B_2O_3 (%)[3]	n/a	14.16	14.62	15.18	15.11	15.41	14.53	15.31	15.10	14.74	15.24	14.63
Al_2O_3 (%)	<0.008	33.14	30.43	32.05	31.66	29.84	30.24	32.33	31.75	30.22	30.84	31.08
Cr_2O_3 (%)	<0.011	0.01	0.24	0.75	2.06	3.40	4.98	1.14	1.23	4.50	3.69	3.33
MgO (%)	<0.007	9.03	9.10	9.37	8.89	8.83	8.44	8.92	9.34	8.77	8.50	8.87
CaO (%)	<0.006	0.11	0.13	0.13	0.13	0.16	0.20	0.14	0.12	0.05	0.27	0.13
MnO (%)	<0.011	0.00	0.00	0.00	0.00	0.00	0.00	0.00	0.01	0.00	0.00	0.00
FeO (%)	<0.03	3.64	3.21	2.90	2.60	3.01	2.47	2.61	2.59	2.59	2.51	2.92
Na_2O (%)	<0.009	2.67	2.57	2.31	2.51	2.64	2.45	2.46	2.49	2.59	2.42	2.41
K_2O (%)	<0.006	0.03	0.01	0.02	0.03	0.03	0.02	0.03	0.01	0.01	0.01	0.01
Formula based on 29 O												
B		3.00	3.00	3.00	3.00	3.00	3.00	3.00	3.00	3.00	3.00	3.00
Si		5.95	6.30	5.99	5.98	5.97	5.94	5.99	5.99	5.95	5.96	5.95
Ti		0.03	0.08	0.06	0.04	0.07	0.05	0.03	0.06	0.03	0.03	0.02
Al		6.29	5.78	6.14	6.08	5.81	5.83	6.20	6.08	5.84	5.97	5.97
Cr		0.00	0.03	0.10	0.27	0.44	0.64	0.15	0.16	0.58	0.48	0.43
Fe^{2+}		0.49	0.43	0.39	0.35	0.42	0.34	0.36	0.35	0.36	0.34	0.40
Mn		0.00	0.00	0.00	0.00	0.00	0.00	0.00	0.00	0.00	0.00	0.00
Mg		2.17	2.19	2.27	2.16	2.18	2.06	2.16	2.26	2.14	2.08	2.16
Ca		0.02	0.02	0.02	0.02	0.03	0.03	0.02	0.02	0.01	0.05	0.02
Na		0.83	0.80	0.73	0.79	0.85	0.78	0.78	0.78	0.82	0.77	0.76
K		0.01	0.00	0.00	0.01	0.01	0.00	0.01	0.00	0.00	0.00	0.00
X site												
Na		0.83	0.80	0.73	0.79	0.85	0.78	0.78	0.78	0.82	0.77	0.76
K		0.01	0.00	0.00	0.01	0.01	0.00	0.01	0.00	0.00	0.00	0.00
Ca		0.02	0.02	0.02	0.02	0.03	0.03	0.02	0.02	0.01	0.05	0.02
X-Vac		0.14	0.18	0.24	0.18	0.12	0.18	0.19	0.19	0.17	0.18	0.21
Y site												
Fe^{2+}		0.49	0.43	0.39	0.35	0.42	0.34	0.36	0.35	0.36	0.34	0.40
Mg		2.17	2.00	2.27	2.16	2.18	2.06	2.16	2.26	2.14	2.08	2.16
Mn^{2+}		0.00	0.00	0.00	0.00	0.00	0.00	0.00	0.00	0.00	0.00	0.00
Al^{3+}		0.24	0.00	0.13	0.06	0.00	0.00	0.19	0.08	0.00	0.00	0.00
Cr^{3+}		0.00	0.00	0.10	0.27	0.22	0.41	0.15	0.16	0.37	0.40	0.35
Ti		0.03	0.08	0.06	0.04	0.07	0.05	0.03	0.06	0.03	0.03	0.02
Mg/(Mg+Fe) Y site		0.82	0.82	0.85	0.86	0.84	0.86	0.86	0.87	0.86	0.86	0.84
Na/(Na+Ca) X site		0.98	0.97	0.97	0.97	0.97	0.96	0.97	0.97	0.99	0.94	0.97
$^{X}\square/(^{X}\square+Na^{1+}+K^{1+})$		0.14	0.18	0.25	0.18	0.12	0.19	0.20	0.20	0.17	0.19	0.22

Table D Vein tourmaline EPMA analyses in weight% and apfu. (Continued)

Sample		19-GR-574GA-06		19-GR-638AS-02			19-GR-656AS-03			19-GR-645AS-02		
Host rock[1]		Carbonate-fuchsite schist		Carbonate-fuchsite schist			Carbonate schist			Carbonate schist		
Analysis #		1	2	1	2	3	1	2	3	1	2	3
Tourmaline species		Dravite	Dravite	Dravite	Dravite	Dravite	Dravite	Dravite	Dravite	Dravite	Dravite	Dravite
	LOD											
SiO_2 (%)	<0.007	37.29	36.80	37.38	36.43	36.42	36.57	36.80	36.18	37.11	37.14	38.29
TiO_2 (%)	<0.025	0.46	0.67	0.33	0.28	0.41	0.93	0.84	0.70	0.85	0.27	0.05
B_2O_3 (%)[3]	n/a	13.90	14.52	13.92	15.48	14.69	13.97	13.80	15.32	13.69	14.56	13.88
Al_2O_3 (%)	<0.008	32.70	32.70	33.03	32.79	33.02	32.21	31.34	31.52	32.25	32.97	33.08
Cr_2O_3 (%)	<0.011	0.00	0.00	0.48	0.33	0.16	0.59	1.22	0.23	0.09	0.01	0.04
MgO (%)	<0.007	10.03	9.66	8.91	9.00	9.18	9.37	9.82	9.16	10.01	9.67	10.17
CaO (%)	<0.006	0.17	0.21	0.10	0.09	0.09	0.23	0.38	0.24	0.36	0.12	0.04
MnO (%)	<0.011	0.00	0.02	0.00	0.00	0.01	0.01	0.00	0.00	0.00	0.00	0.02
FeO (%)	<0.03	2.72	2.69	3.50	3.16	3.54	3.37	3.23	4.07	2.98	2.58	2.20
Na_2O (%)	<0.009	2.73	2.73	2.36	2.43	2.48	2.73	2.58	2.58	2.66	2.68	2.23
K_2O (%)	<0.006	0.02	0.00	0.01	0.01	0.00	0.03	0.00	0.01	0.00	0.00	0.01
Formula based on 29 O												
B		3.00	3.00	3.00	3.00	3.00	3.00	3.00	3.00	3.00	3.00	3.00
Si		5.97	5.93	5.99	5.94	5.90	5.90	5.93	5.94	5.94	5.98	6.08
Ti		0.06	0.08	0.04	0.03	0.05	0.11	0.10	0.09	0.10	0.03	0.01
Al		6.17	6.21	6.24	6.31	6.31	6.12	5.95	6.10	6.09	6.25	6.19
Cr		0.00	0.00	0.06	0.04	0.02	0.07	0.16	0.03	0.01	0.00	0.01
Fe^{2+}		0.36	0.36	0.47	0.43	0.48	0.45	0.44	0.56	0.40	0.35	0.29
Mn		0.00	0.00	0.00	0.00	0.00	0.00	0.00	0.00	0.00	0.00	0.00
Mg		2.39	2.32	2.13	2.19	2.22	2.25	2.36	2.24	2.39	2.32	2.40
Ca		0.03	0.04	0.02	0.02	0.02	0.04	0.07	0.04	0.06	0.02	0.01
Na		0.85	0.85	0.73	0.77	0.78	0.85	0.80	0.82	0.83	0.84	0.69
K		0.00	0.00	0.00	0.00	0.00	0.01	0.00	0.00	0.00	0.00	0.00
X site												
Na		0.85	0.85	0.73	0.77	0.78	0.85	0.80	0.82	0.83	0.84	0.69
K		0.00	0.00	0.00	0.00	0.00	0.01	0.00	0.00	0.00	0.00	0.00
Ca		0.03	0.04	0.02	0.02	0.02	0.04	0.07	0.04	0.06	0.02	0.01
X-Vac		0.12	0.11	0.25	0.21	0.20	0.10	0.13	0.14	0.11	0.14	0.31
Y site												
Fe^{2+}		0.36	0.36	0.47	0.43	0.48	0.45	0.44	0.56	0.40	0.35	0.29
Mg		2.39	2.32	2.13	2.19	2.22	2.25	2.36	2.24	2.39	2.32	2.40
Mn^{2+}		0.00	0.00	0.00	0.00	0.00	0.00	0.00	0.00	0.00	0.00	0.00
Al^{3+}		0.13	0.15	0.23	0.25	0.21	0.02	0.00	0.04	0.03	0.23	0.19
Cr^{3+}		0.00	0.00	0.06	0.04	0.02	0.07	0.04	0.03	0.01	0.00	0.01
Ti		0.06	0.08	0.04	0.03	0.05	0.11	0.10	0.09	0.10	0.03	0.01
Mg/(Mg+Fe) Y site		0.87	0.87	0.82	0.84	0.82	0.83	0.84	0.80	0.86	0.87	0.89
Na/(Na+Ca) X site		0.97	0.96	0.98	0.98	0.98	0.96	0.92	0.95	0.93	0.98	0.99
$^{X}\square/(^{X}\square+Na^{1+}+K^{1+})$		0.13	0.11	0.25	0.22	0.21	0.10	0.14	0.14	0.12	0.14	0.31

Table D Vein tourmaline EPMA analyses in weight% and apfu. (Continued)

Sample		19-GR-645AS-02	19-GR-645AS-06				19-GR-04-EB-04			
Host rock[1]		Carbonate schist	Carbonate schist				Carbonate schist			
Analysis #		4	1	2	3	4	1	2	3	4
Tourmaline species		Dravite	Dravite	Dravite	Dravite	Dravite	Dravite	Dravite	Dravite	Dravite
	LOD									
SiO_2 (%)	<0.007	37.14	36.70	36.38	36.02	36.82	36.54	36.31	35.82	36.27
TiO_2 (%)	<0.025	0.78	0.62	0.62	1.08	0.17	0.38	1.02	1.28	0.35
B_2O_3 (%)[3]	n/a	14.27	14.74	14.55	15.31	15.04	13.79	14.51	14.68	14.20
Al_2O_3 (%)	<0.008	32.48	32.11	30.81	31.11	32.71	32.17	31.45	30.22	33.29
Cr_2O_3 (%)	<0.011	0.00	1.02	2.49	0.58	0.00	0.00	0.01	0.00	0.03
MgO (%)	<0.007	9.81	9.36	9.51	9.50	9.93	8.45	8.38	7.92	8.24
CaO (%)	<0.006	0.35	0.20	0.29	0.36	0.06	0.25	0.44	0.45	0.22
MnO (%)	<0.011	0.00	0.01	0.01	0.00	0.00	0.00	0.01	0.00	0.00
FeO (%)	<0.03	2.63	2.70	2.80	3.48	2.89	5.75	5.48	7.15	4.86
Na_2O (%)	<0.009	2.52	2.54	2.53	2.54	2.38	2.67	2.38	2.48	2.52
K_2O (%)	<0.006	0.01	0.01	0.02	0.02	0.00	0.01	0.00	0.01	0.01
Formula based on 29 O										
B		3.00	3.00	3.00	3.00	3.00	3.00	3.00	3.00	3.00
Si		5.97	5.95	5.93	5.91	5.96	5.94	5.94	5.94	5.89
Ti		0.09	0.08	0.08	0.13	0.02	0.05	0.13	0.16	0.04
Al		6.15	6.13	5.91	6.02	6.24	6.16	6.07	5.91	6.37
Cr		0.00	0.13	0.32	0.08	0.00	0.00	0.00	0.00	0.00
Fe^{2+}		0.35	0.37	0.38	0.48	0.39	0.78	0.75	0.99	0.66
Mn		0.00	0.00	0.00	0.00	0.00	0.00	0.00	0.00	0.00
Mg		2.35	2.26	2.31	2.32	2.40	2.05	2.05	1.96	1.99
Ca		0.06	0.03	0.05	0.06	0.01	0.04	0.08	0.08	0.04
Na		0.78	0.80	0.80	0.81	0.75	0.84	0.76	0.80	0.79
K		0.00	0.00	0.00	0.00	0.00	0.00	0.00	0.00	0.00
X site										
Na		0.78	0.80	0.80	0.81	0.75	0.84	0.76	0.80	0.79
K		0.00	0.00	0.00	0.00	0.00	0.00	0.00	0.00	0.00
Ca		0.06	0.03	0.05	0.06	0.01	0.04	0.08	0.08	0.04
X-Vac		0.15	0.17	0.15	0.12	0.24	0.11	0.16	0.12	0.17
Y site										
Fe^{2+}		0.35	0.37	0.38	0.48	0.39	0.78	0.75	0.99	0.66
Mg		2.35	2.26	2.31	2.32	2.40	2.05	2.05	1.81	1.99
Mn^{2+}		0.00	0.00	0.00	0.00	0.00	0.00	0.00	0.00	0.00
Al^{3+}		0.11	0.08	0.00	0.00	0.20	0.10	0.01	0.00	0.25
Cr^{3+}		0.00	0.13	0.16	0.00	0.00	0.00	0.00	0.00	0.00
Ti		0.09	0.08	0.08	0.13	0.02	0.05	0.13	0.16	0.04
Mg/(Mg+Fe) Y site		0.87	0.86	0.86	0.83	0.86	0.72	0.73	0.65	0.75
Na/(Na+Ca) X site		0.93	0.96	0.94	0.93	0.99	0.95	0.91	0.91	0.95
$^{X}\square/(^{X}\square+Na^{1+}+K^{1+})$		0.16	0.17	0.15	0.13	0.24	0.12	0.18	0.13	0.17

Table D Vein tourmaline EPMA analyses in weight% and apfu. (Continued)

Sample		19-GR-12A-04	19-GR-476SC-01								
Host rock[1]		Carbonate schist	Carbonate schist								
Analysis #		1	1	2	3	4	5	6	7	8	9
Tourmaline species		Dravite	Dravite	Dravite	Mg-foitite[2]	Dravite	Dravite	Dravite	Mg-foitite[2]	Dravite	Dravite
	LOD										
SiO_2 (%)	<0.007	36.82	36.37	36.30	36.76	36.24	36.55	37.23	36.76	35.71	35.39
TiO_2 (%)	<0.025	0.02	0.31	0.49	0.13	0.27	0.49	0.54	0.00	0.32	0.21
B_2O_3 (%)[3]	n/a	15.06	14.49	14.16	14.48	13.71	14.18	13.50	14.96	14.59	15.03
Al_2O_3 (%)	<0.008	31.52	34.38	34.52	34.57	34.28	33.49	33.57	33.86	34.19	33.66
Cr_2O_3 (%)	<0.011	0.01	0.00	0.00	0.01	0.00	0.00	0.03	0.00	0.05	0.03
MgO (%)	<0.007	10.25	5.97	6.02	6.01	6.32	6.36	6.42	6.38	5.84	5.97
CaO (%)	<0.006	0.08	0.35	0.52	0.24	0.51	0.60	0.57	0.25	0.77	1.87
MnO (%)	<0.011	0.00	0.03	0.01	0.04	0.02	0.00	0.03	0.01	0.03	0.03
FeO (%)	<0.03	3.80	6.52	6.21	6.32	6.78	6.50	6.32	6.33	6.81	6.24
Na_2O (%)	<0.009	2.44	1.57	1.77	1.46	1.88	1.83	1.80	1.45	1.69	1.57
K_2O (%)	<0.006	0.01	0.00	0.01	0.00	0.00	0.00	0.00	0.00	0.01	0.02
Formula based on 29 O											
B		3.00	3.00	3.00	3.00	3.00	3.00	3.00	3.00	3.00	3.00
Si		6.00	5.93	5.90	5.97	5.88	5.96	6.01	6.01	5.86	5.85
Ti		0.00	0.04	0.06	0.02	0.03	0.06	0.07	0.00	0.04	0.03
Al		6.06	6.61	6.61	6.62	6.56	6.43	6.38	6.52	6.61	6.55
Cr		0.00	0.00	0.00	0.00	0.00	0.00	0.00	0.00	0.01	0.00
Fe^{2+}		0.52	0.89	0.84	0.86	0.92	0.89	0.85	0.87	0.93	0.86
Mn		0.00	0.00	0.00	0.00	0.00	0.00	0.00	0.00	0.00	0.00
Mg		2.49	1.45	1.46	1.46	1.53	1.55	1.54	1.55	1.43	1.47
Ca		0.01	0.06	0.09	0.04	0.09	0.10	0.10	0.04	0.14	0.33
Na		0.77	0.50	0.56	0.46	0.59	0.58	0.56	0.46	0.54	0.50
K		0.00	0.00	0.00	0.00	0.00	0.00	0.00	0.00	0.00	0.00
X site											
Na		0.77	0.50	0.56	0.46	0.59	0.58	0.56	0.46	0.54	0.50
K		0.00	0.00	0.00	0.00	0.00	0.00	0.00	0.00	0.00	0.00
Ca		0.01	0.06	0.09	0.04	0.09	0.10	0.10	0.04	0.14	0.33
X-Vac		0.21	0.44	0.35	0.50	0.32	0.32	0.34	0.50	0.33	0.16
Y site											
Fe^{2+}		0.52	0.89	0.84	0.86	0.92	0.89	0.85	0.87	0.93	0.86
Mg		2.49	1.45	1.46	1.46	1.53	1.55	1.54	1.55	1.43	1.47
Mn^{2+}		0.00	0.00	0.00	0.00	0.00	0.00	0.00	0.00	0.00	0.00
Al^{3+}		0.06	0.54	0.51	0.59	0.44	0.38	0.38	0.52	0.47	0.40
Cr^{3+}		0.00	0.00	0.00	0.00	0.00	0.00	0.00	0.00	0.01	0.00
Ti		0.00	0.04	0.06	0.02	0.03	0.06	0.07	0.00	0.04	0.03
Mg/(Mg+Fe) Y site		0.83	0.62	0.63	0.63	0.62	0.64	0.64	0.64	0.60	0.63
Na/(Na+Ca) X site		0.98	0.89	0.86	0.92	0.87	0.85	0.85	0.91	0.80	0.60
$^{X}\square/(^{X}\square+Na^{1+}+K^{1+})$		0.22	0.47	0.39	0.52	0.35	0.36	0.38	0.52	0.38	0.24

Table D Vein tourmaline EPMA analyses in weight% and apfu. (Continued)

Sample		19-GR-476SC-01		19-GR-17A-01		
Host rock[1]		Carbonate schist		Andesite		
Analysis #		10	11	1	2	3
Tourmaline species		Dravite	Dravite	Schorl	Dravite	Dravite
	LOD					
SiO_2 (%)	<0.007	36.10	35.27	35.86	35.82	35.50
TiO_2 (%)	<0.025	0.37	0.39	0.57	0.17	0.05
B_2O_3 (%)[3]	n/a	13.87	14.84	13.93	14.30	14.79
Al_2O_3 (%)	<0.008	34.04	32.90	30.25	30.76	30.94
Cr_2O_3 (%)	<0.011	0.01	0.00	0.01	0.02	0.02
MgO (%)	<0.007	6.08	6.09	5.67	5.87	5.96
CaO (%)	<0.006	0.62	2.32	0.35	0.37	0.36
MnO (%)	<0.011	0.03	0.03	0.01	0.02	0.03
FeO (%)	<0.03	7.01	6.55	10.73	10.18	9.76
Na_2O (%)	<0.009	1.87	1.60	2.60	2.47	2.58
K_2O (%)	<0.006	0.00	0.01	0.03	0.03	0.03
Formula based on 29 O						
B		3.00	3.00	3.00	3.00	3.00
Si		5.88	5.84	6.00	6.00	5.97
Ti		0.05	0.05	0.07	0.02	0.01
Al		6.54	6.42	5.97	6.07	6.13
Cr		0.00	0.00	0.00	0.00	0.00
Fe^{2+}		0.95	0.91	1.50	1.43	1.37
Mn		0.00	0.00	0.00	0.00	0.00
Mg		1.48	1.50	1.41	1.46	1.49
Ca		0.11	0.41	0.06	0.07	0.07
Na		0.59	0.52	0.84	0.80	0.84
K		0.00	0.00	0.01	0.01	0.01
X site						
Na		0.59	0.52	0.84	0.80	0.84
K		0.00	0.00	0.01	0.01	0.01
Ca		0.11	0.41	0.06	0.07	0.07
X-Vac		0.30	0.07	0.09	0.13	0.09
Y site						
Fe^{2+}		0.95	0.91	1.50	1.43	1.37
Mg		1.48	1.50	1.38	1.46	1.49
Mn^{2+}		0.00	0.00	0.00	0.00	0.00
Al^{3+}		0.42	0.26	0.00	0.06	0.10
Cr^{3+}		0.00	0.00	0.00	0.00	0.00
Ti		0.05	0.05	0.07	0.02	0.01
Mg/(Mg+Fe) Y site		0.61	0.62	0.48	0.51	0.52
Na/(Na+Ca) X site		0.85	0.56	0.93	0.92	0.93
$^{x}\square/(^{x}\square+Na^{1+}+K^{1+})$		0.34	0.12	0.09	0.14	0.10

[1]Wall rock of the sampled vein
[2]Magnesio-foitite
[3]$B_2O_3+H_2O+Li_2O+F$ calculated by difference

Appendix E – Boundary conditions of the 3D model

Appendix E1 – The four tested scenarios

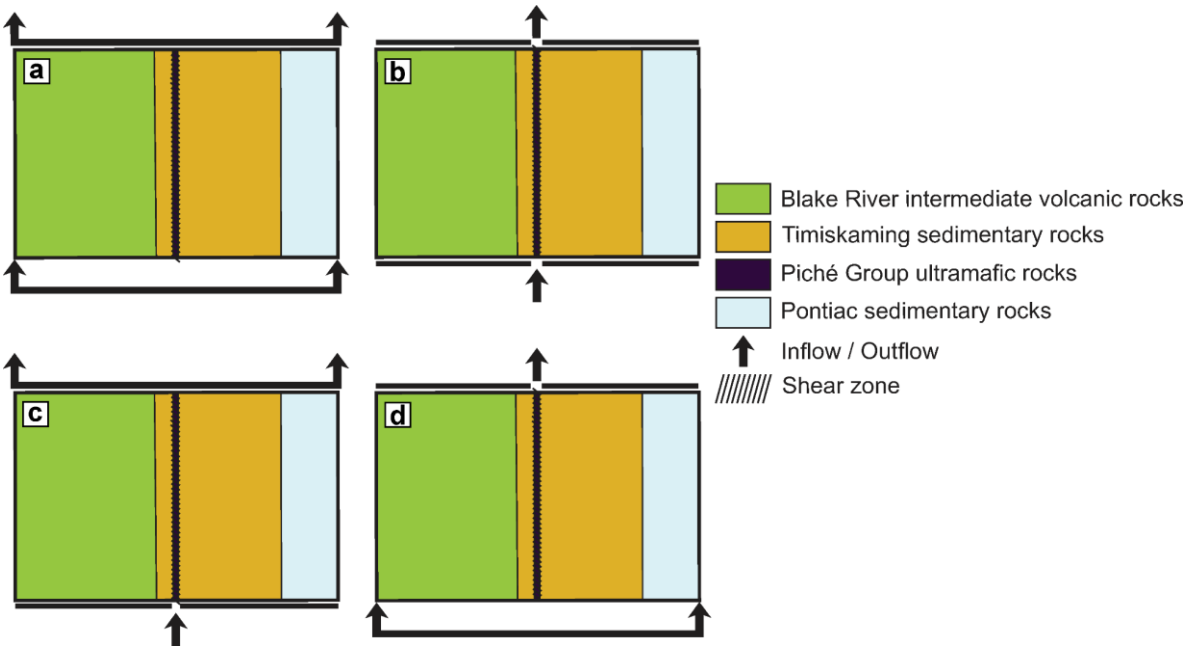

Figure E1 Cross-section of the model (Fig. 18) at X = 0 m, looking east, showing the four different tested geologically realistic boundary conditions, adapted from Beaudoin et al. (2006). Impermeable lateral boundaries have been assigned for every scenario. **a** Both the upper and lower boundaries are considered permeable. Fluid inflow is at the bottom (*bar with arrows*), and outflow is at the top of the model (*bar with arrows*). **b** Both the upper and lower boundaries are impermeable, except along the Piché Group, where inflow and outflow are permitted (*arrows*). **c** The bottom boundary is considered impermeable, except along the Piché Group where fluid inflow (*arrow*) is allowed, and a fluid outflow *(bar with arrows*) at the upper permeable boundary. **d** Fluid inflow is allowed from the bottom and permeable boundary of the model (*bar with arrows*). The upper boundary is considered impermeable, and the outflow is controlled at the top (*arrow*) by the Piché Group.

Appendix E2 – Scenario A

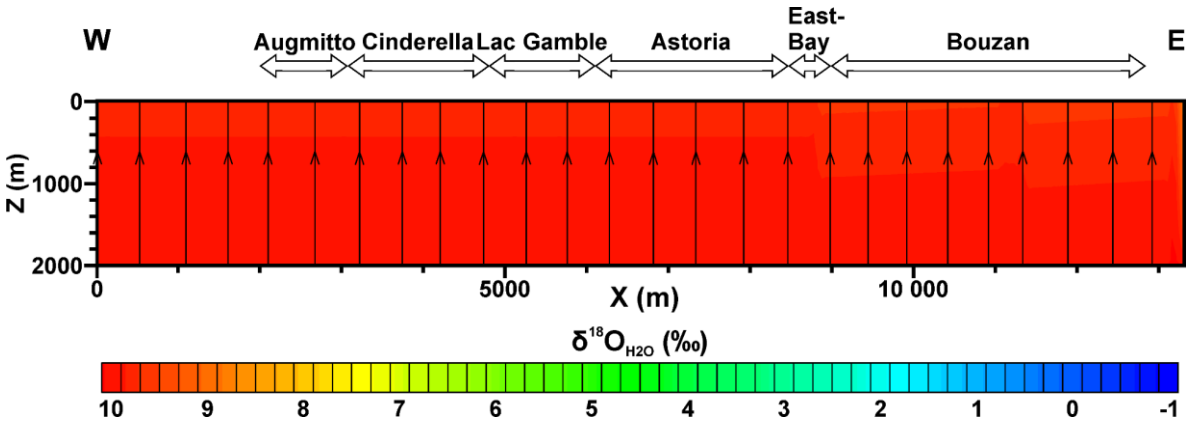

Figure E2 Simulated $\delta^{18}O_{H2O}$ values for boundary conditions of scenario A (Appendix E1) after 1000 years within the Piché Group. The streamlines are displayed to show the direction of the infiltrating fluid.

Appendix E3 – Scenario B

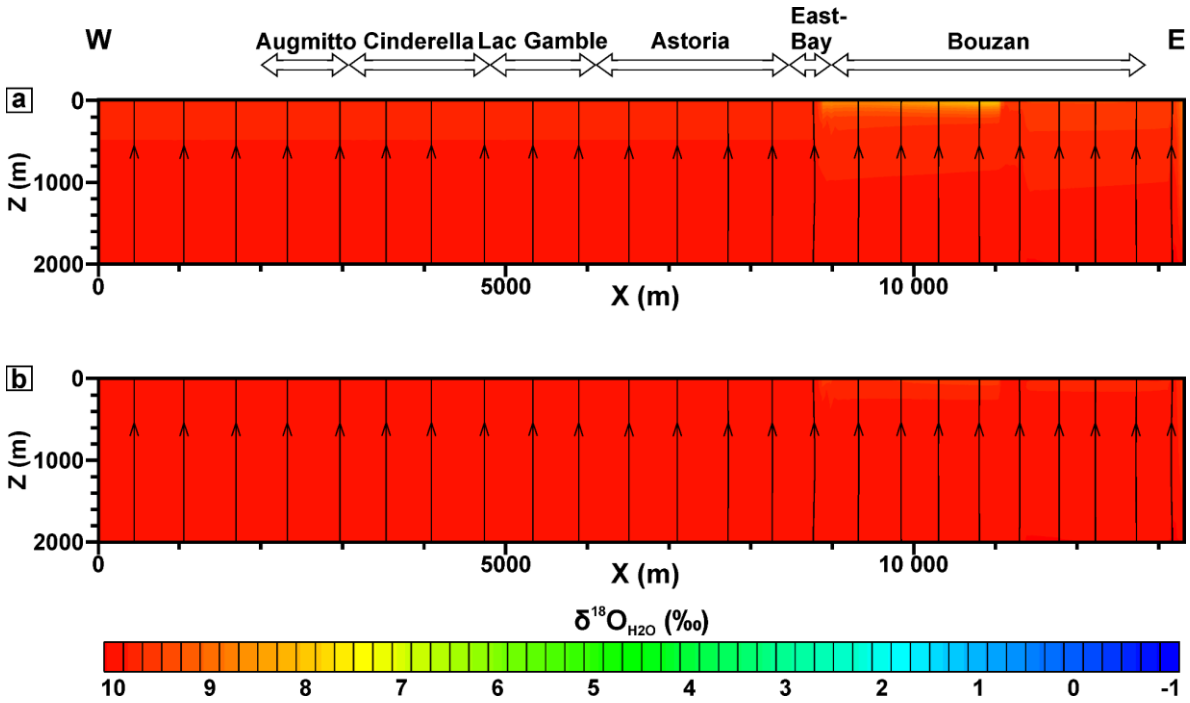

Figure E3 Simulated $\delta^{18}O_{H2O}$ values for boundary conditions of scenario B (Appendix E1) after (**a**) 1000 and (**b**) 100 000 years within the Piché Group. The streamlines are displayed to show the direction of the infiltrating fluid.

Appendix E4 – Scenario C

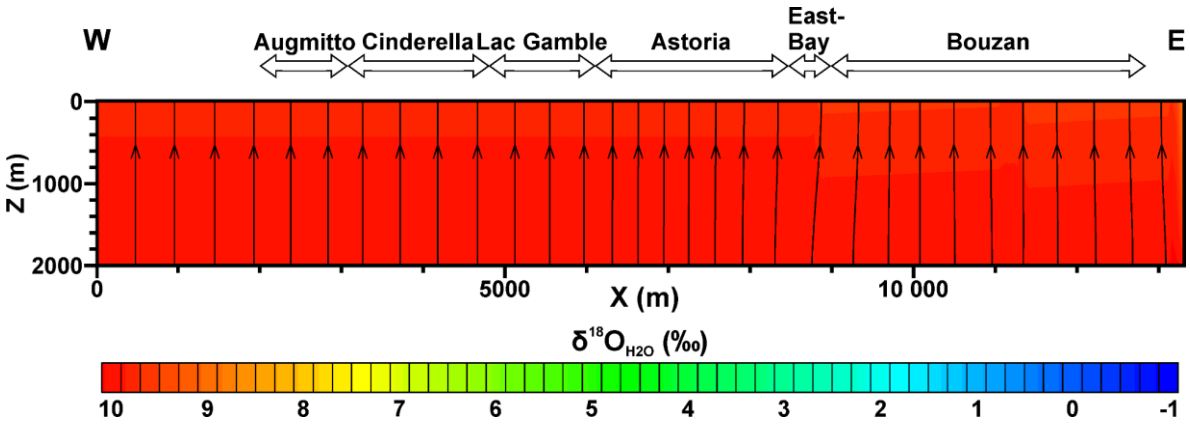

Figure E4 Simulated $\delta^{18}O_{H2O}$ values for boundary conditions of scenario C (Appendix E1) after 1000 years within the Piché Group. The streamlines are displayed to show the direction of the infiltrating fluid.

Appendix F – $\delta^{18}O$ of Quartz vs Carbonate

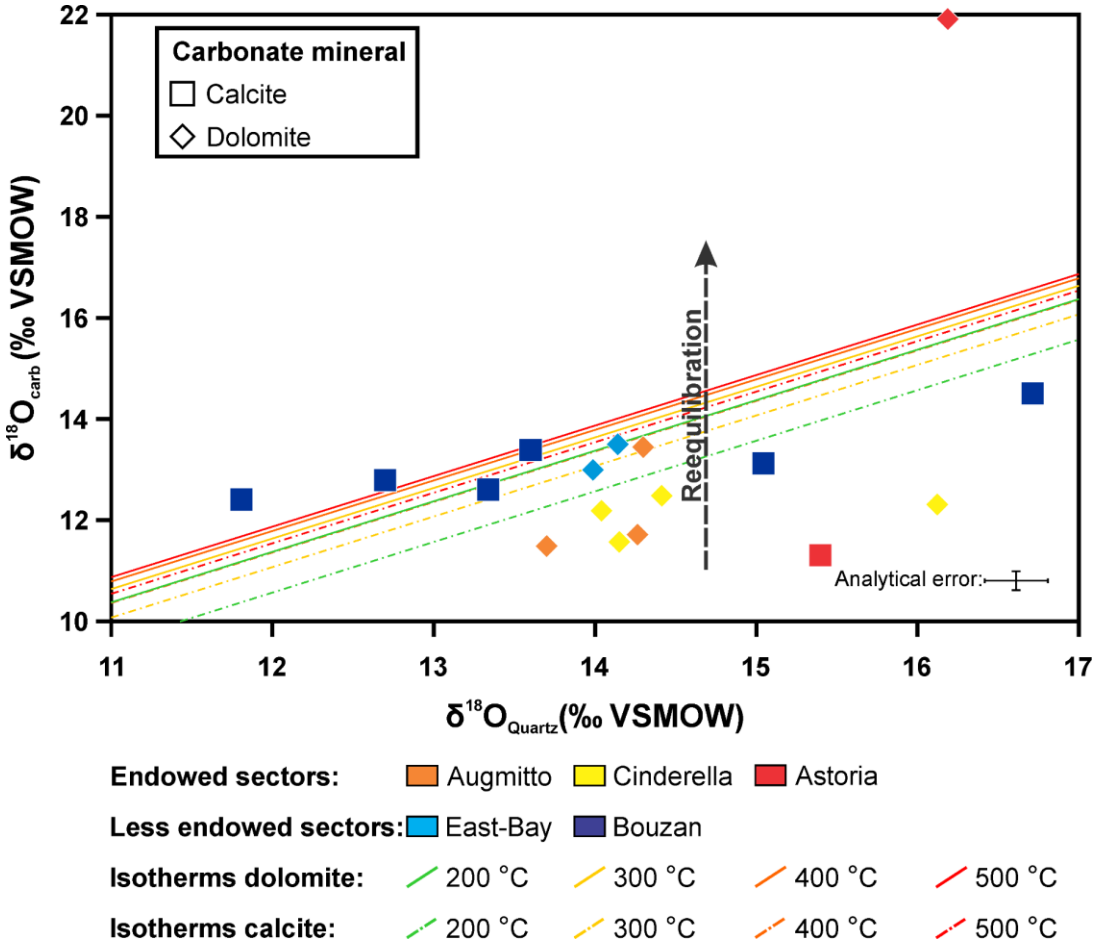

Figure F1 Plot of $\delta^{18}O$ values of coexisting quartz and tourmaline along the Augmitto-Bouzan segment. The isotherms were calculated from the oxygen isotope fractionation equations of Vho et al. (2019). The *arrow* shows the reequilibration path of carbonate minerals.

Appendix G – Fluid/rock ratio parameters

Table G.1 Necessary information for fluid/rock ratio calculations and results for closed and open-system, in molar %.

Block	Sample	Host rock	UTM Nad83 Zone 17N		Depth	$\delta^{18}O^{f}_{rock}$ VSMOW	$\delta^{18}O^{i}_{rock}$ VSMOW	$\delta^{18}O^{i}_{H2O}$ VSMOW	Temperature	$\Delta_{rock-H2O}$ VSMOW	F/R open system
			Easting	Northing	m	(‰)	(‰)	(‰)	°C	(‰)	(Molar)
Augmitto	19-GR-631AUG-01	Greywacke	641091	5339817	450.6	11.7	8.6	10.0	250/ 300/ 350	8.3/6.4/5.0	0.4/0.5/0.7
	19-GR-124S-04	Talc-chlorite schist	641482	5339556	54.1	7.9	5.5	6.2	273	3.6	0.8
	19-GR-405S-15	Carbonate schist	641815	5339693	361.8	9.8	5.5	6.7	282	7.2	0.7
	19-GR-442S-09	Carbonate schist	641962	5339531	25.1	11.7	5.5	7.3	300	6.6	1.4
	19-GR-425S-03	Carbonate±fuchsite schist	642011	5339554	20.2	9.7	5.5	7.5	310	6.0	0.8
	19-GR-415S-09	Carbonate±fuchsite schist	642082	5339970	653.1	9.6	5.5	10.4	409	3.6	0.7
Cinderella	19-GR-535CI-03	Carbonate±fuchsite schist	642455	5339885	499.9	9.4	5.5	9.3	370	4.4	0.6
	19-GR-610CI-06	Carbonate±fuchsite schist	642457	5339732	223.3	9.7	5.5	8.5	330	5.4	0.7
	19-564CI-07	Carbonate schist	642737	5339838	525.5	9.7	5.5	10.8	420	3.5	0.7
	19-603CI-04	Carbonate schist	642821	5339660	98.2	9.3	5.5	5.2	228	9.3	0.5
	19-467CI-04	Carbonate schist	642930	5339846	389.1	10.3	5.5	9.1	359	4.8	0.8
	19-GR-620CI-04	Carbonate schist	643745	5339681	46.5	11.1	5.5	7.9	320	5.8	1.2
Lac Gamble	19-GR-500GA-07	Carbonate±fuchsite schist	644328	5339940	682.3	9.6	5.5	7.8	310	5.8	0.7
	19-GR-628GA-02	Greywacke	644374	5339851	484.2	12.7	8.6	10.0	250/ 300/ 350	8.1/6.3/4.9	0.6/ 0.8/ 1.1
	19-GR-574GA-05	Carbonate±fuchsite schist	644602	5340005	632.8	9.5	5.5	7.7	306	5.9	0.7
	19-GR-461GA-05	Carbonate±fuchsite schist	644672	5339740	268.4	9.9	5.5	7.8	310	5.8	1.2
Astoria	19-GR-638AS-06	Carbonate±fuchsite schist	645984	5339913	470.2	9.9	5.5	9.4	344	4.9	0.7
	19-GR-299AS-09	Greywacke	646128	5339808	289.7	10.6	8.6	10.0	250/ 300/ 350	8.1/6.3/4.9	0.2/ 0.3/ 0.4
	19-GR-656AS-06	Carbonate schist	646606	5340175	852.1	8.0	5.5	8.5	363	4.0	0.4
	19-GR-645AS-07	Carbonate schist	646871	5339779	136.1	7.5	5.5	6.5	285	6.0	0.3
East-Bay	19-GR-650AS-02	Albitite dyke	647600	5339868	295.7	6.5	5.8	10	250/ 300/ 350	6.6/ 4.9/ 3.7	0.1/ 0.1/ 0.1
	19-GR-04EB-01	Carbonate schist	647931	5339789	108.2	10.0	5.5	4.4	235	8.7	0.9
Bouzan	19-GR-12A-08	Carbonate schist	648128	5339808	118.2	9.7	5.5	6.0	266	7.4	0.7
	19-GR-476SC-06	Greywacke	648373	5340157	516.0	11.6	8.6	10.0	250/ 300/ 350	8.0/6.1/4.7	0.4/ 0.5/ 0.7
	19-GR-475SC-03	Talc-chlorite schist	648559	5339995	306.9	11.2	5.5	5.7	260	6.5	1.9
	19-GR-652BO-05	Greywacke	648801	5340049	254.7	13.5	8.6	10.0	250/ 300/ 350	8.2/6.3/4.9	0.7/ 1.0/ 1.5
	19-GR-483BW-05	Greywacke	649714	5340347	173.8	9.7	8.6	10.0	250/ 300/ 350	8.0/ 6.1/ 4.7	0.1/ 0.2/ 0.2
	19-GR-480BW-01	Greywacke	649987	5340263	111.5	12.0	8.6	10.0	250/ 300/ 350	8.0/ 6.1/ 4.7	0.4/ 0.6/ 0.8
	19-GR-17A-05	Carbonate schist	650304	5340335	25.5	8.1	5.5	9.3	280	6.9	0.3
	19-GR-473BO-04	Greywacke	650866	5340497	95.4	10.1	8.6	10.0	250/ 300/ 350	8.0/ 6.1/ 4.7	0.2/ 0.2/ 0.3
	19-GR-472BO-04	Greywacke	651529	5340552	71.1	10.5	8.6	10.0	250/ 300/ 350	8.3/ 6.4/ 5.0	0.2/ 0.3/ 0.4